

GRAVITY GRADIENT SURVEY WITH A MOBILE ATOM  
INTERFEROMETER

A DISSERTATION  
SUBMITTED TO THE DEPARTMENT OF APPLIED PHYSICS  
AND THE COMMITTEE ON GRADUATE STUDIES  
OF STANFORD UNIVERSITY  
IN PARTIAL FULFILLMENT OF THE REQUIREMENTS  
FOR THE DEGREE OF  
DOCTOR OF PHILOSOPHY

Xinan Wu  
March 2009

© Copyright by Xinan Wu 2009  
All Rights Reserved

I certify that I have read this dissertation and that, in my opinion, it is fully adequate in scope and quality as a dissertation for the degree of Doctor of Philosophy.

---

(Mark A. Kasevich) Principal Adviser

I certify that I have read this dissertation and that, in my opinion, it is fully adequate in scope and quality as a dissertation for the degree of Doctor of Philosophy.

---

(Yoshihisa Yamamoto)

I certify that I have read this dissertation and that, in my opinion, it is fully adequate in scope and quality as a dissertation for the degree of Doctor of Philosophy.

---

(David A. B. Miller)

Approved for the Stanford University Committee on Graduate Studies.



For my family,  
both near and far.

# Abstract

The field of atom interferometry has grown rapidly over the last two decades, opening up a new direction in precision metrology. Atom interferometers have proven to be valuable tools for measuring gravitational and inertial effects. In particular, gravimeters, gradiometers, and gyroscopes based on atom interferometry have all demonstrated high accuracies competitive with state-of-the-art commercial technology. We describe here the development and operation of a compact mobile gravity gradiometer using  $\pi/2 - \pi - \pi/2$  sequence with two-photon stimulated Raman transitions in a dual atomic fountain setup for precision gravity gradient survey and other gravity tests. Various noise sources have been identified and overcome, and a differential acceleration sensitivity of  $4.2 \times 10^{-9} g/\sqrt{\text{Hz}}$  has been achieved over a 70 cm baseline in the laboratory. The apparatus was then moved into a box-truck and a gravity gradient survey was conducted near a 4 story-deep building, at an accuracy of  $7 \times 10^{-9}/\text{s}^2$  in gravity gradient with about three minutes integration at each survey point. The survey results agreed with a theoretical model considering detailed floor plan and building structure. In addition, technique to measure absolute gravity gradient is discussed. Finally, a complete dynamic model of the  $\pi/2 - \pi - \pi/2$  sequence was established, and potential algorithms to de-correlate apparatus platform noise during survey based on this model were identified.

# Acknowledgements

I am deeply indebted to my advisor Professor Mark Kasevich, who supported, inspired, and encouraged me throughout my whole graduate study. I learned so much from both his knowledge of science and his approach to problem-solving.

Thanks to Brent Young and Todd Gustavson for not only leading the development of our custom instrument, but also kindly guided me at the early stage of my graduate study. Mohan Gurunathan and Jie Deng helped develop my electronics skills, which became essential later on. I am grateful to Jeff Fixler, Matt Cashen, and Todd Kawakami for all the useful advice and encouragement they provided me. I acknowledge Larry Novak and Paul Bayer for their very skillful assembling and cleaning work. I also appreciate Grant Biedermann and Ken Takase for countless hours they spent on teaching me basic experimental skills.

I am undoubtedly grateful to Grant Biedermann, Louis Deslauriers, and Sean Roy for all the time and efforts they put into investigating and reducing apparatus noise, and for all the insightful and fruitful discussions. In particular, Louis unreservedly helped me on various parts of this thesis work - for example, appendix B is nearly entirely derived from his notes. Also, big thanks to Chetan Mahadeswaraswamy for his work on the truck, without which none of the mobile tests would have been possible. Thanks to Ken Bower and Tom Langenstein for their work during the critical stage of this project when we integrated systems in the truck. I am also thankful to John Stockton for his advice on data analysis and control theory. I also thank other group members in Kasevich's group, as well as people in Chu's group for providing helpful advice and instruments whenever needed.

# Contents

<b>Abstract</b>	<b>vi</b>
<b>Acknowledgements</b>	<b>vii</b>
<b>1 Introduction</b>	<b>1</b>
1.1 Gravity Gradiometer . . . . .	1
1.1.1 Gravity Gradient Measurement . . . . .	1
1.1.2 Applications of Gravity Gradiometer . . . . .	4
1.2 Brief History of Atom Interferometry . . . . .	6
1.3 Overview . . . . .	6
<b>2 Atomic Fountain Overview</b>	<b>8</b>
2.1 Two-Level System . . . . .	8
2.2 Atomic Structure of Cesium . . . . .	10
2.3 Cold Atom Preparation . . . . .	11
2.4 State Selection and Optical Pumping . . . . .	13
2.5 Detection . . . . .	14
<b>3 Atom Interferometry</b>	<b>19</b>
3.1 Stimulated Raman Transition . . . . .	19
3.2 Interferometer Phase Shift . . . . .	22
3.2.1 Path Integral Approach . . . . .	23
3.2.2 Wave Packet Approach . . . . .	28
3.2.2.1 Wave Packet and Atom Cloud . . . . .	29

3.2.2.2	Wave Packet Interacting with Raman Pulse . . . . .	31
3.2.2.3	Example 1: $\delta T$ -Scan . . . . .	32
3.2.2.4	Example 2: Pitch Noise . . . . .	33
3.2.3	Acceleration Measurement . . . . .	34
3.3	Raman Beam Path Asymmetry . . . . .	36
3.4	Multi-Photon Sequence . . . . .	38
<b>4</b>	<b>Experimental Apparatus</b>	<b>41</b>
4.1	Portable Laser System . . . . .	42
4.2	Control and Electronics System . . . . .	43
4.3	Sensor Hardware . . . . .	45
4.4	Mobile Laboratory in a Truck . . . . .	46
<b>5</b>	<b>Data Analysis</b>	<b>48</b>
5.1	Ellipse Fitting . . . . .	48
5.1.1	Ellipse Fitting Noise and Systematic Error . . . . .	50
5.1.2	Single Ellipse Fitting Residue . . . . .	51
5.2	Phase and Contrast Noise Correction . . . . .	55
5.3	Direct Phase Extraction . . . . .	59
5.4	Sine Fitting . . . . .	61
5.5	Dedrifting and Allan Deviation . . . . .	61
5.6	Derivative and Differential Measurement . . . . .	64
<b>6</b>	<b>Error Model</b>	<b>67</b>
6.1	Analysis in the Earth Frame . . . . .	67
6.1.1	Symbols Used in the Model . . . . .	69
6.1.2	Contrast Model . . . . .	71
6.1.3	Platform Noise and Contrast Noise . . . . .	72
6.1.4	Term Evaluation . . . . .	73
6.1.5	A Note on Numerical Calculation . . . . .	74
6.2	Analysis in the Inertial Frame . . . . .	75
6.3	Imperfection of Raman Windows . . . . .	78

6.3.1	Wedge . . . . .	78
6.3.2	Window Attenuation . . . . .	81
6.4	Wedge Noise Model . . . . .	82
6.4.1	Two-Dimensional Wedge . . . . .	82
6.4.2	Three-Dimensional Wedge . . . . .	85
6.5	Gradiometer Error Terms . . . . .	88
6.5.1	Ideal Condition . . . . .	89
6.5.2	Stable Condition . . . . .	90
6.5.3	Jitter Terms . . . . .	91
<b>7</b>	<b>Various Noise and Effects Study</b>	<b>93</b>
7.1	Interferometer Simulator . . . . .	93
7.1.1	Intensity Noise . . . . .	95
7.1.2	Raman Beam Size . . . . .	99
7.2	Spontaneous Emission . . . . .	99
7.3	Atom Cloud Temperature . . . . .	102
7.4	Detection Bleedthrough Model . . . . .	105
7.5	$0 \rightarrow 2$ Transition . . . . .	108
<b>8</b>	<b>Gravity Gradient Measurements</b>	<b>111</b>
8.1	Gradiometer Performance . . . . .	111
8.2	Gravity Anomaly Survey . . . . .	112
8.3	Baseline Determination . . . . .	117
8.4	Absolute Gravity Gradient Measurement . . . . .	118
8.5	Motion Sensitivity . . . . .	119
8.5.1	Yaw Rotation Response . . . . .	120
8.5.2	Disturbance Sensitivity . . . . .	122
<b>9</b>	<b>Conclusion</b>	<b>125</b>
9.1	Future Improvements . . . . .	125
<b>A</b>	<b>Characteristic Data</b>	<b>127</b>

<b>B Transition Calculation</b>	<b>129</b>
B.1 AC Stark Calculation . . . . .	129
B.2 Spontaneous Emission . . . . .	132
<b>Bibliography</b>	<b>135</b>

# List of Tables

3.1	Evolution of Phase during Interferometer . . . . .	26
6.1	Gradiometer Phase in Ideal Condition . . . . .	89
6.2	Symbols for Stable Gradiometer . . . . .	90
6.3	Gradiometer Phase in Stable Condition . . . . .	91
6.4	Symbols for Jitter Gradiometer . . . . .	91
6.5	Gradiometer Phase in Jitter Condition . . . . .	92
7.1	Interferometer Simulator Parameters . . . . .	94
7.2	Interferometer Simulator Pulse Performance . . . . .	94
7.3	Interferometer Simulator Noise . . . . .	95
8.1	Disturbance Test Fitting Results . . . . .	124
A.1	Useful Constants and Relevant Cesium Parameters . . . . .	127

# List of Figures

1.1	Gravity Gradient of the Earth . . . . .	2
1.2	Gravity Gradient Measurement . . . . .	3
2.1	Energy Diagram of Two-level System . . . . .	9
2.2	Cesium Energy Level Structure . . . . .	11
2.3	Zeeman-State Optical Pumping . . . . .	15
2.4	Schematic of the Detection System . . . . .	16
2.5	CCD Image of Fringe . . . . .	17
2.6	Detection SNR . . . . .	18
3.1	Three-Level System . . . . .	20
3.2	Interferometer Phase . . . . .	23
3.3	Gravity Gradient Measurement . . . . .	35
3.4	Raman Beam Path Asymmetry for Single Sensor . . . . .	36
3.5	Ultra-short $T$ Illustrating Raman Beam Path Asymmetry . . . . .	38
3.6	Raman Beam Path Asymmetry for Dual Sensor . . . . .	38
3.7	$4\hbar k$ Sequence . . . . .	39
3.8	$4\hbar k$ Sequence Fountain . . . . .	40
4.1	System Block Diagram . . . . .	41
4.2	System Integration . . . . .	42
4.3	Raman Generation . . . . .	43
4.4	Laser Distribution . . . . .	44
4.5	Zerodur Cell . . . . .	46

4.6	Raman Beam Delivery . . . . .	46
4.7	Sensor Hardware . . . . .	47
5.1	Ellipse Fitting Noise Conversion . . . . .	51
5.2	Ellipse Fitting Noise Integration . . . . .	52
5.3	Ellipse Fitting Systematic Error . . . . .	53
5.4	Ellipse Fitting Residue Conversion . . . . .	55
5.5	Phase and Contrast Noise Correction . . . . .	57
5.6	Phase Correction in Microwave Clock . . . . .	58
5.7	Direct Phase Extraction . . . . .	60
5.8	Allan Deviation of Dedrifted Signal . . . . .	64
5.9	Differential Measurement Correction . . . . .	66
6.1	Earth Frame Coordinate System . . . . .	68
6.2	Platform Noise and Contrast Noise . . . . .	73
6.3	Extra Phase Shift Due to Earth Rotation . . . . .	77
6.4	Short- $T$ Phase v.s. $T$ . . . . .	79
6.5	Roll Sensitivity . . . . .	80
6.6	Single 2D Wedge . . . . .	83
6.7	Dual 2D Wedge . . . . .	84
6.8	Single 3D Wedge . . . . .	85
7.1	Intensity Noise Propagation . . . . .	98
7.2	Raman Beam Size and Pulse Efficiency . . . . .	100
7.3	Spontaneous Emission Calculation . . . . .	101
7.4	Spatial Temperature Distribution . . . . .	103
7.5	Detected Atom Temperature . . . . .	104
7.6	Detection Bleedthrough . . . . .	106
7.7	Bleedthrough Correction . . . . .	107
7.8	$0 \rightarrow 2$ Transition Paths . . . . .	108
7.9	$0 \rightarrow 2$ Transition Strength . . . . .	109
7.10	Observed $0 \rightarrow 2$ Transition . . . . .	110

8.1	Mass Chopping Data . . . . .	112
8.2	Mass Chopping Allan Deviation . . . . .	113
8.3	Truck During Survey . . . . .	114
8.4	Survey Allan Deviation . . . . .	114
8.5	Predicted Gravity Gradient Map . . . . .	115
8.6	Gravity Gradient Survey Result . . . . .	116
8.7	Baseline Measurement . . . . .	118
8.8	Yaw Chop Test . . . . .	120
8.9	Yaw Rotation Effect . . . . .	121
8.10	Disturbance Test Ellipse . . . . .	123
8.11	Disturbance Test Result . . . . .	124
A.1	Cesium Energy Levels . . . . .	128
B.1	Raman Energy Diagram . . . . .	131



# Chapter 1

## Introduction

### 1.1 Gravity Gradiometer

#### 1.1.1 Gravity Gradient Measurement

Gravity gradiometer measures the change rate of gravity field over space. The gravity gradient tensor is the derivative of gravitational acceleration  $\mathbf{g}$  and is represented by a three-by-three matrix:

$$T = \nabla \cdot \mathbf{g} = \begin{pmatrix} \partial_x g_x & \partial_y g_x & \partial_z g_x \\ \partial_x g_y & \partial_y g_y & \partial_z g_y \\ \partial_x g_z & \partial_y g_z & \partial_z g_z \end{pmatrix} = \begin{pmatrix} T_{xx} & T_{xy} & T_{xz} \\ T_{yx} & T_{yy} & T_{yz} \\ T_{zx} & T_{zy} & T_{zz} \end{pmatrix}, \quad (1.1)$$

where  $\mathbf{g}$  is the derivative of the gravitational potential:

$$\mathbf{g}(\mathbf{r}) = -\nabla\Phi(\mathbf{r}). \quad (1.2)$$

Due to the conservative nature of the field,  $T_{ij} = T_{ji}$ , and  $\nabla^2\Phi = 0$  which gives

$$T_{xx} + T_{yy} + T_{zz} = 0. \quad (1.3)$$

Therefore, only five components of the gravity gradient tensor in equation 1.1 are independent (although sometimes all  $T_{xx}$ ,  $T_{yy}$ , and  $T_{zz}$  are shown for convenience).

Gravity gradient is often quoted in the unit of Eötvös, named after Baron Roland von Eötvös, a Hungarian physicist who invented the first gradiometer in 1886 [1, 2]. The unit is usually written as E, and  $1 \text{ E} = 10^{-9}/\text{s}^2$ , or about  $10^{-10}g/\text{m}$  where  $g$  is the acceleration of gravity at the surface of the Earth.

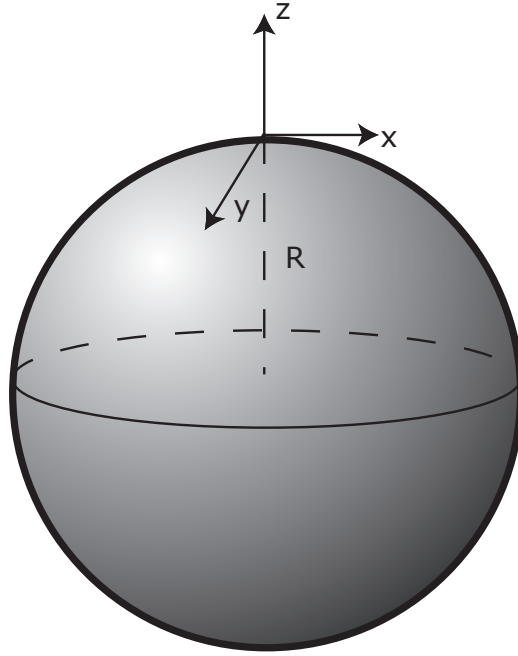


Figure 1.1: Coordinate system for defining gravity gradient of the Earth.  $R$  is the radius of the Earth.

As an example, human body generates a gravity gradient of about 5 E at a meter away; while the gravity gradient generated by the mass of the Earth, represented in the coordinate system as shown in figure 1.1, is given by

$$\begin{cases} T_{xx} = T_{yy} & = g/R \approx 1500 \text{ E} \\ T_{zz} & = -2g/R \approx -3000 \text{ E} \\ T_{xy} = T_{xz} = T_{yz} & = 0, \end{cases} \quad (1.4)$$

Note that gravity gradient is a scalar tensor, so, for example, even if  $z$ -axis is defined in the reverse direction (pointing towards the center of the Earth),  $T_{zz}$  is still negative.



Figure 1.2: Gravity gradient measurement by differential accelerometers.

A gravity gradient measurement is typically achieved by making two acceleration measurements at two locations. For example, (see figure 1.2)

$$T_{yy}(y_0) = \left. \frac{\partial g_y(y)}{\partial y} \right|_{y=y_0} \approx \frac{g_y(y_0 + L/2) - g_y(y_0 - L/2)}{L}. \quad (1.5)$$

Here  $g_y(y)$  denotes the component of gravity along the measurement axis and  $y_0$  is the midpoint of where these two measurements are made.  $L$  is called the measurement baseline. Some gradiometers, particularly our apparatus, are designed to measure inline gravity gradient, as shown in equation 1.5. In other words, we measure the change of gravity acceleration component along the line connecting two sensors. Cross components such as  $T_{xy}$  cannot be measured directly by inline measurement. It can be shown that the general expression for an arbitrary inline measurement along an axis in spherical coordinates defined by the polar angle  $\phi$  and azimuthal angle  $\theta$  is given by

$$\begin{aligned} T_{\phi,\theta}^{\text{inline}} = & + (\cos^2 \theta \sin^2 \phi - \cos^2 \phi) T_{xx} \\ & + (\sin^2 \theta \sin^2 \phi - \cos^2 \phi) T_{yy} \\ & + \sin 2\theta \sin^2 \phi T_{xy} \\ & + \cos \theta \sin 2\phi T_{xz} \\ & + \sin \theta \sin 2\phi T_{yz}. \end{aligned} \quad (1.6)$$

With five inline gravity gradient measurements along five independent axes, one can

derive all five independent components of the gravity gradient tensor.

### 1.1.2 Applications of Gravity Gradiometer

Due to equivalence principle, any platform acceleration (vibration) would be picked up by accelerometer and be mistakenly interpreted as gravity signal. However, gradiometer utilizes two simultaneous acceleration measurements ideally referenced to the same platform, and the platform vibration noise is therefore largely canceled when two measurements are subtracted to extract the gravity gradient value. The gravity gradient measurement can tolerate relatively high platform noise and is advantageous in dynamic environment such as survey, yet it does provide valuable information of the local gravity environment. Similarly, in precision scientific measurements, gravity gradiometry lessens the constraints on the level of knowledge of local gravitational field which could be modified by tides, ocean loading, and local structures [3]. In this section we describe a few applications of gravity gradiometer, followed by a summary of current gradiometer technologies.

Gradiometer is very useful in detecting subsurface mass anomalies. Research has shown that full tensor gradiometry (FTG) can be used to accurately locate anomaly location and other properties [4, 5]. The first gradiometer invented by Eötvös in 1886 was improved, and combined with seismic methods, it became the standard technique in mineral exploration, particularly oil [6] and diamond mine [7] discovery. Similar methods can be used to detect water reservoir levels, underground tunnel, and submarine structures [8]. The gravity gradient survey can be conducted even with airborne instrument or satellite with reasonably controlled platform noise, making it very convenient in remote area where land-based survey is difficult.

Navigation system also requires high precision gravity gradiometers, particularly in the inertial navigation system (INS) [9]. The Global Positioning System (GPS) provides an excellent navigation tool on the Earth, however there are a number of environments where GPS is unavailable (such as urban and submarine area) [10], where INS could provide a “fly-wheel” in those dead zones. The INS is extensively used in aerospace and deep space navigation, and is based on the same principle

as gravity measurements. Distinguishing the true acceleration of the motion from the surrounding gravity signature is essential in precision inertial navigation systems. Recently it has been shown that gravity anomalies could result in significant error in inertial navigation, and an on-board gravity gradiometer could correct that error [11]. In addition, exact knowledge of the Earth gravitational field dynamically measured on-board GPS satellite could provide orbital perturbation corrections and improve GPS accuracy.

Besides practical applications, gravity gradiometer also draws great attention from the scientific community. One of the least known fundamental constants is the gravitational constant  $G$ , and gravity gradiometer, such as torsion balance instrument, is one of the best ways to measure  $G$  [12]. Since the invention of the first gravity gradiometer, the accuracy of the  $G$  measurement has been gradually improved [13, 14]. A more precise value of  $G$  is beneficial for a number of related areas, such as geophysics and string theory [15, 16, 17, 18, 19, 20]. Besides measuring  $G$ , Eötvös also pioneered in comparing gravitational and inertial mass [2, 21], long before Einstein proposed General Relativity. Recent progress in gravity theory, including Yukawa potential terms, fifth force, and other “new physics”, proposed experiments that require very high precision gravity gradiometers [22, 23].

Currently, the most successful commercial gradiometer is the UGM developed by Bell and later acquired by Lockheed Martin. This Bell gradiometer is based on mechanical accelerometers on a rotating disk, and has full-tensor gradiometry capability. It demonstrated sensitivities on the order of  $10 \text{ E}/\sqrt{\text{Hz}}$ , and is designed for airborne applications [24, 25, 8, 26]. The most sensitive gradiometer reported by far is a superconducting gradiometer developed at Maryland University [27]. The acceleration of the two test masses is detected using two superconducting quantum interference devices (SQUIDs) and the short-term sensitivity of this device is  $0.02 \text{ E}/\sqrt{\text{Hz}}$  [28]. Another competing technology is based on falling corner cube and has demonstrated sensitivity of  $400 \text{ E}/\sqrt{\text{Hz}}$  but very high precision at  $10^{-9}g$  level [29].

## 1.2 Brief History of Atom Interferometry

It was first proposed by de Broglie in 1924 that massive particle has wave-like properties with a wavelength determined by the particle's momentum [30]. First experimental demonstration of the interference in atoms was performed by Ramsey in 1950 [31], and inertial effects in matter waves were first observed in 1975 in neutron interferometer [32, 33]. It is not until recent two decades that atom interferometry demonstrated extremely high sensitivities and excellent long-term stability. Today many different matter wave interferometry experiments are taking the advantage of the wave nature of atoms for precision measurements and fundamental research.

The key enabling technology for atom interferometry is the techniques of manipulating atoms using lasers. In the 1970s, several groups proposed slowing atoms with optical forces [34, 35]. A breakthrough took place in 1985 when Chu and his colleagues trapped neutral atoms with optical molasses and magneto-optical trap (MOT) [36, 37]. Atomic physics then quickly became a hot area, and atom interferometry was demonstrated in 1991 using two-photon stimulated Raman transitions [38, 39, 40, 41].

Since then, atom interferometer has been used for precision measurements of inertial and gravitational effects, such as acceleration [42], gravity gradient [43, 44], rotation rate [45, 46, 47, 48], fine structure constant [49, 50, 51], and gravitational constant  $G$  [52, 53, 54]. Recently, potential experiments based on atom interferometry were proposed in many scientific research areas such as spacetime fluctuations [55, 56] and tests of general relativity, including tests of the equivalence principle [57, 58], measurements of the curvature of space-time [59], and detection of gravitational waves [60, 61, 62].

## 1.3 Overview

The format of this dissertation is as follows. Chapter 2 presents an overview of an atomic fountain, the atomic structure, and operation principles. Chapter 3 reviews some of the basics of atom-photon interactions, Raman transition, and calculation

of interferometer differential phase. The experimental apparatus is described in detail in chapter 4, including the control, electronics, laser, and sensor systems, as well as the boxtruck which enables the gravity gradient survey. Chapter 5 reviews important technique in data analysis, including ellipse fitting, noise decorrelation, and dedrifting. Some minor data processing algorithms are also documented. Chapter 6 discusses a complete model of the  $\pi/2 - \pi - \pi/2$  atom interferometer sequence. Chapter 7 continues to discuss major problems and noise sources we encountered and how we overcome them. Some interesting effects we observed are also presented in this chapter. The results of this work is presented in chapter 8, including gradiometer performance characterization in the laboratory, gravity anomaly survey, and preliminary motion sensitivity studies. Finally, chapter 9 concludes with a brief discussion of possible future improvements that can potentially lead to an order of magnitude more sensitive gravity gradient measurements.

# Chapter 2

## Atomic Fountain Overview

This chapter outlines the basic operation principles of an atomic fountain, including the atomic structure and characteristics we utilize to cool and trap them with laser and magnetic fields. Atomic fountain setup, atomic state preparation and detection sequence will also be discussed, leaving out only the atom interferometry measurement sequence to be discussed in detail in the next chapter.

### 2.1 Two-Level System

When an atom is driven close to resonance of a transition, it can often be approximated as a simple two-level system. In this section, we discuss the dynamics of two-level system without taking into account other effects such as spontaneous emission. This two-level system dynamics serve as the basis of atomic physics, and is used extensively in the operation of our apparatus. It is therefore essential to introduce these concepts and equations before discussing the atomic fountain.

The Hamiltonian for a two-level atom subject to an electric field  $\mathbf{E}$  is

$$\hat{H} = \hbar\omega_e|e\rangle\langle e| + \hbar\omega_g|g\rangle\langle g| - \mathbf{d} \cdot \mathbf{E}, \quad (2.1)$$

here  $\hbar\omega_g$  and  $\hbar\omega_e$  represent the internal energy levels of the ground and excited states, and  $\mathbf{d}$  represents the dipole moment of the atom. For a fixed driving frequency, the

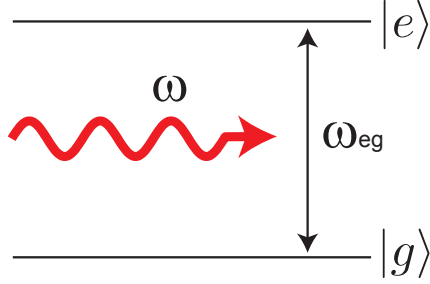


Figure 2.1: Energy diagram of a two-level system.

external (classical) electric field is given by

$$\mathbf{E} = \mathbf{E}_0 \cos(\omega t + \phi). \quad (2.2)$$

The Rabi frequency is defined as

$$\Omega_{eg} = \frac{\langle e | \mathbf{d} \cdot \mathbf{E} | g \rangle}{\hbar} \quad (2.3)$$

which represents the frequency of Rabi oscillation between the two states separated by resonance frequency  $\omega = \omega_e - \omega_g = \omega_{eg}$  (see figure 2.1). The time-dependent Schrodinger equation can be solved for this Hamiltonian by rotating wave approximation [50]. The evolution of the two state amplitudes is given by

$$c_e(t_0 + \tau) = e^{-i\delta\tau/2} \left\{ c_e(t_0) [\cos(\Omega_r\tau/2) - i \cos\theta \sin(\Omega_r\tau/2)] + c_g(t_0) e^{-i(\delta t_0 + \phi)} [-i \sin\theta \sin(\Omega_r\tau/2)] \right\} \quad (2.4)$$

$$c_g(t_0 + \tau) = e^{i\delta\tau/2} \left\{ c_e(t_0) e^{i(\delta t_0 + \phi)} [-i \sin\theta \sin(\Omega_r\tau/2)] + c_g(t_0) [\cos(\Omega_r\tau/2) + i \cos\theta \sin(\Omega_r\tau/2)] \right\} \quad (2.5)$$

where

$$\Omega_r = \sqrt{|\Omega_{eg}|^2 + \delta^2} \quad (2.6)$$

$$\delta = \omega - \omega_{eg} \quad (2.7)$$

$$\sin \theta = \Omega_{eg}/\Omega_r \quad (2.8)$$

$$\cos \theta = -\delta/\Omega_r. \quad (2.9)$$

Note that the state amplitudes oscillate at a Rabi frequency  $\Omega_r$ , with transfer efficiency dependent on  $\delta$ . In particular, if atom is initially prepared in ground state and excited by on-resonance light  $\delta = 0$ , the probability of finding this atom in the excited state after time  $\tau$  is

$$P_e(\tau) = |c_e(\tau)|^2 = \frac{1 - \cos(\Omega_{eg}\tau)}{2}. \quad (2.10)$$

When  $\tau = \pi/\Omega_{eg}$ , the atom is transferred to excited state with a 100% probability, commonly referred as a  $\pi$ -pulse. If  $\tau$  is half of that, the pulse puts atom into an equal superposition of the two states, and is referred as a  $\pi/2$ -pulse. In practice, often a cloud of atoms is observed, and the on-resonance condition can seldom be satisfied by all the atoms, and the Rabi frequency is often different for different parts of the cloud due to spatial intensity profile of the laser beam. In this case, we usually call the pulse that transfers the maximum number of atoms to the other state as a  $\pi$ -pulse. This will be discussed in more detail in section 7.1.

Finally, it is also important to note that the final state amplitudes contains a dependence on local optical phase  $\phi$ . This phase is not important in single-pulse Rabi oscillation case, but is very important in full interferometer sequence which consists of many pulses separated in time.

## 2.2 Atomic Structure of Cesium

It is said that the periodic table for atomic physicists consists primarily of only the left-most column (alkali-metal atoms). The heaviest stable element in that column, Cesium (Cs), is used exclusively in our apparatus. A simplified energy level diagram of Cs is shown in figure 2.2. The electron's total angular momentum  $\mathbf{J} = \mathbf{L} + \mathbf{S}$  where  $\mathbf{L}$  is electron's orbital angular momentum and  $\mathbf{S}$  is the electron's spin. For ground state and first excited state,  $L = 0, 1$  respectively. The ground state has  $J = 1/2$ ,

and the first excited state has two fine splitting levels  $J = 1/2, 3/2$ , and the  $J = 1/2$  level is not used in our apparatus.

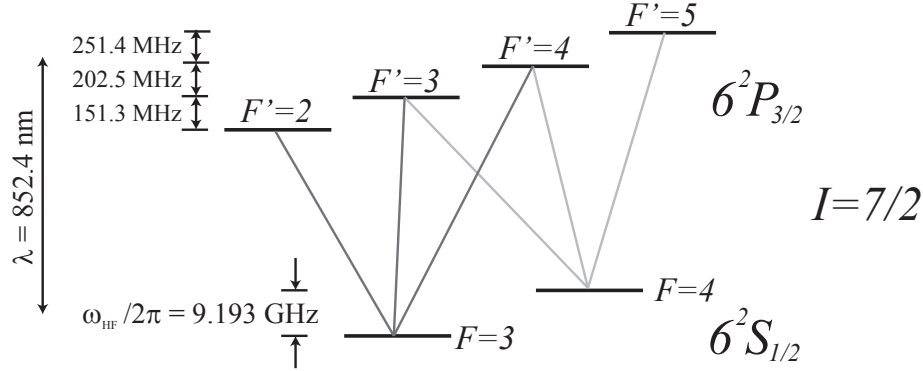


Figure 2.2: Cesium atom energy level structure.

The Cs atom has a nucleus spin  $I = 7/2$ .  $I$  interacts with  $J$  weakly, giving the total atom angular momentum  $F = J + I$ . As a result, the ground state has two hyperfine splitting levels, the  $6^2S_{1/2}$   $F = 3$  and  $F = 4$  levels, separated by 9.192631770 GHz exactly (the definition of second), and the first excited state  $6^2P_{3/2}$  has four hyperfine splitting levels usually denoted by  $F' = 2, 3, 4, 5$  respectively. The optical transition from state  $6^2S_{1/2}$  to state  $6^2P_{3/2}$  can be driven by laser of wavelength  $\lambda \approx 852.3$  nm.

Each hyperfine level is further split into  $(2F+1)$  Zeeman  $m_F$  sub-levels in the presence of external magnetic field. The  $|F = 3, m_F = 0\rangle$  and  $|F = 4, m_F = 0\rangle$  sub-levels are usually used in atom interferometry experiment such as atomic clocks because their energy levels are second-order sensitive to external magnetic field [63].

## 2.3 Cold Atom Preparation

Standard atomic fountain technique has been used in our atom interferometry experiment. This section outlines all the essential parts of cold atom sample preparation in the atomic fountain, including cooling, trapping, and launching. Detailed explanation can be found in [64].

Laser cooling has become the “out-of-the-box” solution to cooling alkali-metal atoms. The cycling cooling transition of Cs is  $|F = 4, m_F = 4\rangle \rightarrow |F' = 5, m'_F = 5\rangle$ . Six laser beams with frequency slightly red-detuned ( $\approx 10$  MHz) from this cooling transition are used to slow down Cs atoms. Other transitions are a few hundreds MHz away, so once an atom goes into this cooling transition, it is continuously cooled down as they undergoes dozens of cycling cooling transitions every microsecond. This process is referred as Doppler cooling. During this cooling process, a small portion of the atoms can be excited into other energy levels, falling outside the cooling transition. It is therefore necessary to include a weak repump light tuned at transition frequency of  $|F = 3\rangle \rightarrow |F' = 4\rangle$  during cooling process. While cooling laser slows down atoms, it is unable to confine atoms spatially. A carefully designed magnetic field is typically placed in addition to the cooling lasers to form a magnetic optic trap (MOT) to trap cooled atoms at the center of intersection of all cooling laser beams.

About  $10^9$  Cs atoms are trapped in a  $\approx 2$  mm  $1/e$ -radius cloud during MOT, and they are launched upwards right after MOT by ramping the frequency of two vertical cooling laser beams in about 2 ms. The downward beam at wavelength  $\lambda = 852.3$  nm is ramped towards red by  $f = 1.17$  MHz, while the upward beam is ramped towards blue by the same amount. As a result, if an atom is at rest in the lab frame, it has more probability to absorb a directional photon from the upward beam than from the downward beam, thus making the atom move faster upwards. The atom continues to accelerate upwards until it reaches the desired launching speed of  $v = \lambda f = 1$  m/s upwards, at which speed the atom sees all six cooling laser beams at the same frequency (due to Doppler shift). The process is similar to laser cooling, and one can think that in the moving frame of 1 m/s upwards, atoms are cooled and trapped just like in the lab frame before launching, thus a cloud of cool atoms moving at 1 m/s upwards is prepared.

The Doppler cooling process slows atoms down to  $\sim 100$   $\mu\text{K}$  or 0.1 m/s average thermal velocity, and the sub-Doppler cooling is required to further cool atoms down to a few  $\mu\text{K}$  so that the expansion of atom cloud is small enough during measurement sequence for efficient detection. After launching atoms, laser beam intensities are ramped down, and their detunings are ramped from the original  $\approx 10$  MHz to  $\approx 60$

MHz. Few  $\mu\text{K}$  temperature is achieved after sub-Doppler cooling process, and average thermal velocity is on the order of 1 cm/s. More detailed investigation on the atom cloud temperature can be found later in section 7.3.

## 2.4 State Selection and Optical Pumping

After the cooling and launching sequence mentioned in the previous section, the prepared cloud of  $\sim 10^9$  cold atoms are distributed across all  $m_F$  levels in the  $|F = 4\rangle$  ground state. As mentioned in section 2.2, two  $|m_F = 0\rangle$  ground levels are used in this atom interferometry work. This section outlines the technique to select out atoms in the  $|m_F = 0\rangle$  level and to improve the population in this level.

To select atoms in the  $|m_F = 0\rangle$  level, a microwave  $\pi$ -pulse tuned at resonance frequency of transition  $|F = 3, m_F = 0\rangle \rightarrow |F = 4, m_F = 0\rangle$  is used to transfer atoms in level  $|F = 4, m_F = 0\rangle$  to level  $|F = 3, m_F = 0\rangle$ . A magnetic field of  $\approx 28$  mG is applied to break the degeneracy of different  $m_F$  energy levels, so that with a sufficiently long  $\pi$ -pulse length (with low microwave power) atoms in levels other than  $|F = 4, m_F = 0\rangle$  are not addressed by this state-selection microwave pulse, and are then heated up and kicked away by a downward 50  $\mu\text{s}$  laser pulse tuned on resonance frequency of optical transition  $|F = 4\rangle \rightarrow |F' = 5\rangle$ . A cloud of  $\sim 10^8$  cold atoms in  $|F = 3, m_F = 0\rangle$  level is prepared by this sequence.

This state-selection sequence removes about 90% of the trap atoms because the population is about evenly distributed across all 9  $m_F$  levels in  $|F = 4\rangle$  after cooling and trapping. The general trick of increasing population in  $|m_F = 0\rangle$  level is to carefully design a optical and/or microwave pulse sequence to redistribute atoms across all the  $m_F$  levels while keeping  $|m_F = 0\rangle$  a “dark” level not responding to this designed sequence. The commonly used optical pumping is one implementation of this sequence [65]. Briefly,  $\pi$ -polarized laser beam tuned on transition  $|F = 4\rangle \rightarrow |F' = 4\rangle$  is used to redistribute  $|F = 4\rangle$  atoms across  $m_F$  levels, and because transition  $|F = 4, m_F = 0\rangle \xrightarrow{\pi} |F' = 4, m_F = 0\rangle$  is forbidden, atoms falling into  $|F = 4, m_F = 0\rangle$  level are not able to get out. At the same time, some atoms spontaneously decay into  $|F = 3\rangle$  state, and a repump light tuned on transition

$|F = 3\rangle \rightarrow |F' = 4\rangle$  is also necessary during this process to pump those atoms back to  $|F = 4\rangle$  state. This optical pumping scheme is reported to get 95% of total atoms into  $|F = 4, m_F = 0\rangle$  state, and has been tried in our apparatus to achieve about 50% efficiency in selecting  $|m_F = 0\rangle$  atoms. However, this scheme requires the generation of an additional optical frequency  $|F = 4\rangle \rightarrow |F' = 4\rangle$ , and very pure  $\pi$ -polarization is also required to ensure the level  $|F = 4, m_F = 0\rangle$  is dark. So in our experiment, we use a slightly different scheme to increase population in the  $|F = 4, m_F = 0\rangle$  level.

We generate a “microwave frequency comb” using frequency modulation with a modulation index of  $m = 2.40$  and a modulation frequency of 20 kHz, creating a frequency comb with 20 kHz spacing between sidebands and nullified carrier frequency. This 20 kHz matches the spacing in  $\Delta m_F = 0$  microwave transition frequencies under the  $\approx 28$  mG magnetic field applied. A 200  $\mu\text{s}$  microwave pulse of such frequency comb transfers atoms from  $|F = 4, m_F = \pm 1, \pm 2, \pm 3\rangle$  to the corresponding  $m_F$  levels in  $|F = 3\rangle$  state (see figure 2.3), followed by a 10  $\mu\text{s}$   $|F = 3\rangle \rightarrow |F' = 4\rangle$  repump optical pulse. The repump pulse pumps most atoms back to  $|F = 4\rangle$  state and the spontaneous decay redistributes atoms across all  $m_F$  levels. Throughout this process, the  $|F = 4, m_F = 0, \pm 4\rangle$  levels remain dark. This pulse sequence is repeated a few times, resulting about 1/3 of the atoms in the  $|F = 4, m_F = 0\rangle$  level. This Zeeman-state optical pumping (ZOP) enhancement is limited by accumulation of atoms in the  $|F = 4, m_F = \pm 4\rangle$ , and can potentially be improved by introducing a 70 kHz comb in addition to the existing frequency comb. This ZOP sequence does not require the generation of an additional optical frequency, but does require a stable external magnetic field. If the apparatus is moved, external magnetic field change has to be compensated by a magnetic field servo with a 3-axis field control, and that was successfully implemented (see section 4.3).

## 2.5 Detection

After state selection process, a cloud of  $\sim 10^8$  Cs atoms in the  $|F = 3, m_F = 0\rangle$  state enters an atomic interferometer sequence which typically lasts  $\approx 170$  ms and consists of a few stimulated Raman transition pulses. After the interferometer sequence, which

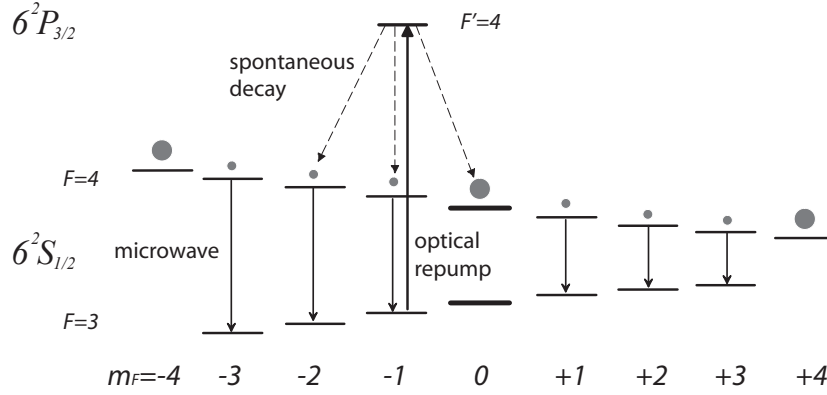


Figure 2.3: Diagram of the energy levels for the Zeeman-state optical pumping in order to increase the population in the  $|m_F = 0\rangle$  level.

will be discussed in the next chapter, the inertial or gravity measurement information is encoded in the population ratio of two ground states  $|F = 3\rangle$  and  $|F = 4\rangle$ . There are various ways of extracting this population ratio information [66]. The detection sequence we use in our apparatus has been summarized in [67]. Briefly, atom cloud is moving at  $\approx 1$  m/s downwards before detection, and a upward propagating laser beam resonant with transition  $|F = 4\rangle \rightarrow |F' = 5\rangle$  is turned on for  $\approx 70 \mu\text{s}$ , which pushes  $|F = 4\rangle$  atoms upwards with a velocity of  $\approx 1$  m/s. Atom in superposition of two states is projected into one state during this process, and this pulse is commonly referred as “separation pulse” or “projection pulse”. After separation pulse, a repump beam tuned on transition  $|F = 3\rangle \rightarrow |F' = 4\rangle$  is pulsed on for a few milliseconds to pump the still-downwards-moving  $|F = 3\rangle$  atoms to  $|F = 4\rangle$  state. After about 5 ms, two atom clouds are separated by about 12 mm, and the upper and lower clouds represent the population of  $|F = 4\rangle$  and  $|F = 3\rangle$  states after interferometer sequence, although they are both in  $|F = 4\rangle$  state now. A detection beam resonant with transition  $|F = 4\rangle \rightarrow |F' = 5\rangle$  is then pulsed on for  $300 \mu\text{s}$  and the resulting fluorescence from each spatially separated atom cloud is imaged onto separate detector, each collects 1.3% of the fluorescence or  $\sim 20$  photons per atom (see figure 2.4). Each quadrant photocurrent output is independently integrated over this detection time. Johnson and photodetector dark current noise are negligible. This detection

sequence is advantageous in that it simultaneously detects two states, thus making it insensitive to detection laser frequency and intensity noise.

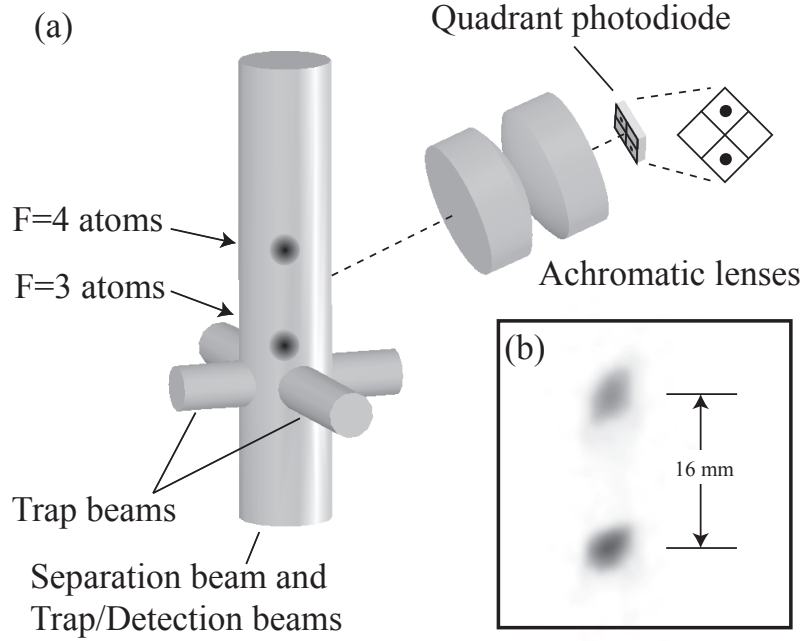


Figure 2.4: Schematic of the detection system.

The separation pulse heats up  $|F = 4\rangle$  atoms, making the cloud size bigger upon detection thus less efficiently detected. We account this effect by introducing a detection efficiency parameter typically called “scaling”  $s$  in calculating the population ratio:

$$r_{3/4} = \frac{sV_3}{V_4}, \quad (2.11)$$

where  $V_3$  and  $V_4$  are the integrated photodetector voltages of  $|F = 3\rangle$  and  $|F = 4\rangle$  state cloud, respectively, and  $s$  is typically  $\approx 0.85$  in our apparatus. The more commonly used way to present measurement result, though, is the “normalized atom number”, or the fraction of population in  $|F = 3\rangle$  state out of the total number of atoms:

$$N_3 = \frac{sV_3}{sV_3 + V_4}. \quad (2.12)$$

This scaling  $s$  is experimentally measured by varying the population ratio using a simple two-pulse microwave Ramsey fringe without changing the loading sequence such that  $(sV_3 + V_4)$  is a constant so  $s$  can be determined by linear fitting. Figure 2.5 shows the spatial distribution of the atoms during the detection stage as a function of such Ramsey sequence interferometer phase.

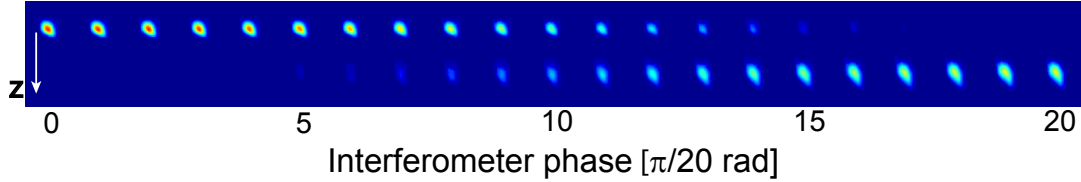


Figure 2.5: A CCD image of the detected atoms showing the change in the relative populations between the  $|F = 3\rangle$  and  $|F = 4\rangle$  states as an interferometer fringe is scanned.

To characterize the detection system performance and signal-to-noise ratio (SNR) limit, atoms are launched, prepared and detected immediately after a short microwave interferometer sequence. We define SNR following the convention in [68]. With very similar detection sequence applied, the SNR is measured with different number of atoms ( $N$ ) loaded, and plotted in figure 2.6. An  $N^{1/2}$  scaling in this figure indicates a shot-noise limited detection system, and SNR of 7800:1 per shot was observed [67], and our apparatus performance is currently not limited by this detection system noise due to other technical noise sources.

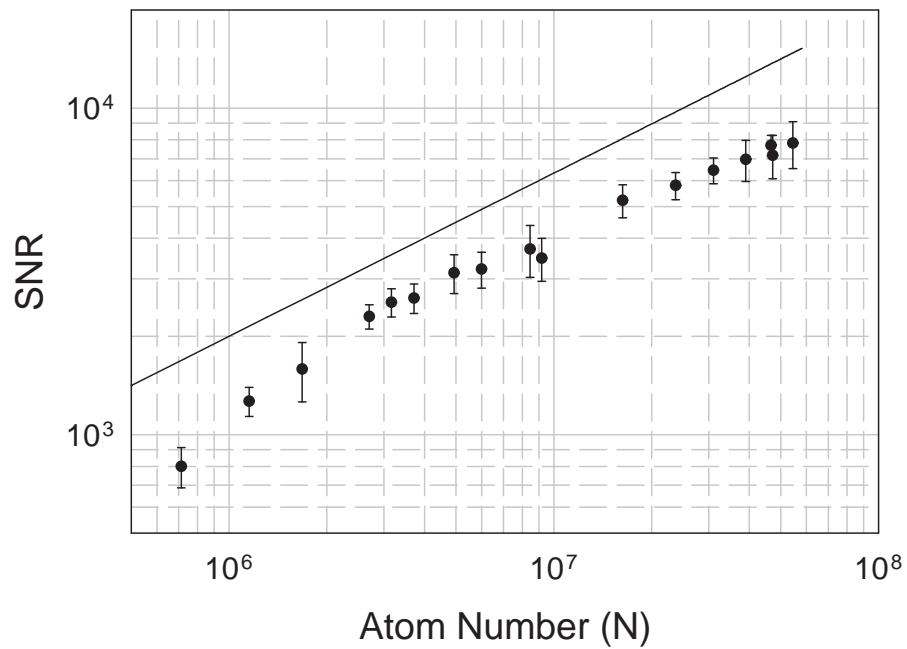


Figure 2.6: SNR is measured as a function of atom number  $N$  by varying the trap loading time. The measured  $N^{1/2}$  dependence suggests that the detection system is limited by atom shot noise scaling. The solid line is an estimate of the quantum projection noise limited SNR ( $2N^{1/2}$ ).

# Chapter 3

## Atom Interferometry

The overall picture of the operation of atomic fountain is introduced in the last chapter. This chapter describes in detail the atomic processes involved in the actual atom interferometry measurement sequence. We start with the theory of stimulated Raman transition and interferometer pulse sequence, followed by the interferometer phase calculation. Finally, gravity gradient measurements based on atom interferometer and advanced atom interferometer sequences are discussed.

### 3.1 Stimulated Raman Transition

Two-photon stimulated Raman transitions [38] are used to coherently manipulate the atomic wavepackets in our experiment. This stimulated Raman pulse couples two hyperfine ground levels with two optical frequencies, with a frequency difference roughly equal to the hyperfine splitting, resulting in a large momentum recoil advantageous to precision inertial measurements. Spontaneous emission is largely suppressed by detuning the single optical frequency far away from the optical transition frequency. A detailed discussion can be found in [50].

A energy level diagram of a three-level system is shown in figure 3.1. The two hyperfine ground state  $|g\rangle$  and  $|e\rangle$  are coupled through an intermediate level  $|i\rangle$  via two optical transitions with angular frequencies  $\omega_1$  and  $\omega_2$ . The combined electric

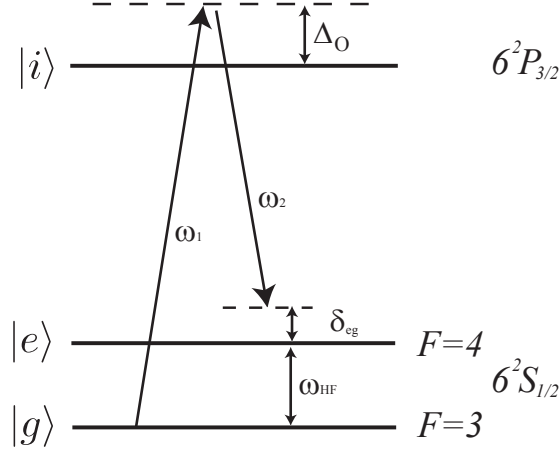


Figure 3.1: Simplified energy diagram of a three-level system.

field in this case is

$$\mathbf{E} = \mathbf{E}_1 \cos(\mathbf{k}_1 \cdot \mathbf{x} - \omega_1 t + \phi_1) + \mathbf{E}_2 \cos(\mathbf{k}_2 \cdot \mathbf{x} - \omega_2 t + \phi_2). \quad (3.1)$$

The Hamiltonian for this three-level system is

$$\hat{H} = \frac{p^2}{2m} + \hbar\omega_g |g\rangle\langle g| + \hbar\omega_e |e\rangle\langle e| + \hbar\omega_i |i\rangle\langle i| - \mathbf{d} \cdot \mathbf{E}. \quad (3.2)$$

In the limit of large single photon detuning  $\Delta_O$ , the intermediate level may be adiabatically eliminated. The eigenstates in the presence of optical fields are simply  $|g, \mathbf{p}\rangle$  and  $|e, \mathbf{p} + \hbar\mathbf{k}_{\text{eff}}\rangle$  indicating internal energy level and external momentum state are coupled. The Hamiltonian in this representation is

$$\hat{H} = \hbar \begin{pmatrix} \Omega_e^{\text{AC}} & \frac{\Omega_{\text{eff}}}{2} e^{-i(\delta_{12}t + \phi_{\text{eff}})} \\ \frac{\Omega_{\text{eff}}}{2} e^{i(\delta_{12}t + \phi_{\text{eff}})} & \Omega_g^{\text{AC}} \end{pmatrix} \quad (3.3)$$

where

$$\Omega_e^{\text{AC}} = \frac{|\Omega_e|^2}{4\Delta} \quad (3.4)$$

$$\Omega_g^{\text{AC}} = \frac{|\Omega_g|^2}{4\Delta} \quad (3.5)$$

$$\delta_{12} = (\omega_1 - \omega_2) - \left( \omega_{eg} + \frac{\mathbf{p} \cdot \mathbf{k}_{\text{eff}}}{m} + \frac{\hbar |\mathbf{k}_{\text{eff}}|^2}{2m} \right) \quad (3.6)$$

$$\Omega_g = -\frac{\langle i | \mathbf{d} \cdot \mathbf{E}_1 | g \rangle}{\hbar} \quad (3.7)$$

$$\Omega_e = -\frac{\langle i | \mathbf{d} \cdot \mathbf{E}_2 | e \rangle}{\hbar} \quad (3.8)$$

$$\Omega_{\text{eff}} = \frac{\Omega_e^* \Omega_g}{2\Delta} e^{i\phi_{\text{eff}}} \quad (3.9)$$

$$\phi_{\text{eff}} = \phi_1 - \phi_2 \quad (3.10)$$

$$\mathbf{k}_{\text{eff}} = \mathbf{k}_1 - \mathbf{k}_2 \quad (3.11)$$

The solution to the Hamiltonian is

$$\begin{aligned} c_{|e, \mathbf{p} + \hbar \mathbf{k}_{\text{eff}}\rangle}(t_0 + \tau) &= e^{-i(\Omega_e^{\text{AC}} + \Omega_g^{\text{AC}})\tau/2} e^{-i\delta_{12}\tau/2} \\ &\quad \left\{ c_{|e, \mathbf{p} + \hbar \mathbf{k}_{\text{eff}}\rangle}(t_0) [\cos(\Omega'_r \tau/2) - i \cos \Theta \sin(\Omega'_r \tau/2)] \right. \\ &\quad \left. + c_{|g, \mathbf{p}\rangle}(t_0) e^{-i(\delta_{12}t_0 + \phi_{\text{eff}})} [-i \sin \Theta \sin(\Omega'_r \tau/2)] \right\} \\ c_{|g, \mathbf{p}\rangle}(t_0 + \tau) &= e^{-i(\Omega_e^{\text{AC}} + \Omega_g^{\text{AC}})\tau/2} e^{i\delta_{12}\tau/2} \\ &\quad \left\{ c_{|e, \mathbf{p} + \hbar \mathbf{k}_{\text{eff}}\rangle}(t_0) e^{i(\delta_{12}t_0 + \phi_{\text{eff}})} [-i \sin \Theta \sin(\Omega'_r \tau/2)] \right. \\ &\quad \left. + c_{|g, \mathbf{p}\rangle}(t_0) [\cos(\Omega'_r \tau/2) + i \cos \Theta \sin(\Omega'_r \tau/2)] \right\} \end{aligned} \quad (3.12)$$

where

$$\Omega'_r = \sqrt{|\Omega_{\text{eff}}|^2 + (\delta_{12} - \delta^{\text{AC}})^2} \quad (3.13)$$

$$\delta^{\text{AC}} = \delta_e^{\text{AC}} - \delta_g^{\text{AC}} \quad (3.14)$$

$$\sin \Theta = \Omega_{\text{eff}} / \Omega'_r \quad (3.15)$$

$$\cos \Theta = (\delta^{\text{AC}} - \delta_{12}) / \Omega'_r. \quad (3.16)$$

The differential ac Stark shift  $\delta^{\text{AC}}$  is usually tuned to zero by adjusting the relative intensities of the two optical frequencies. In the case of on-resonance condition ( $\delta_{12} = 0$ ), the atom undergoes a Rabi flop between two ground states as if it were a two-level

state, with an effective Rabi frequency  $\Omega_{\text{eff}}$ . It is important to note that when an atom transfers from one internal energy state to the other, its external momentum state changes as well, due to the fact that during a two-photon stimulated Raman transition, the atom absorbs a photon from one optical field and then stimulate emits a photon into the other optical field. The momentum change due to this Raman transition is  $\hbar\mathbf{k}_1 - \hbar\mathbf{k}_2 = \hbar\mathbf{k}_{\text{eff}}$ . With two counterpropagating frequencies ( $\mathbf{k}_1 \approx -\mathbf{k}_2$ ), the atom receives the maximum possible momentum recoil of  $\approx 2\hbar\mathbf{k}_1$  (For Cs atom, this recoil corresponds to a velocity change of about  $v_r = 7$  mm/s.).

Generally speaking, the sensitivity of atom interferometer is proportional to  $k_{\text{eff}}$ . The advantage of two-photon Raman transition is that it effectively couples two stable ground states together but with a large  $k_{\text{eff}}$ . As a comparison, one could in principle use microwave to directly couple two hyperfine splitting ground states together and make atom interferometry measurement. However, for a microwave transition at 9.2 GHz for Cs,  $k_{\text{microwave}} = 1.9 \times 10^2 \text{ m}^{-1}$ , while the two-photon transition has a  $k_{\text{eff}} = 1.47 \times 10^7 \text{ m}^{-1}$ , about five orders of magnitude larger than the microwave transition, resulting in a much better sensitivity in inertial measurements.

A precision measurement based on this two-photon transition requires very stable  $k_{\text{eff}}$ , typically at sub-Hz level. For an optical frequency, this requirement of frequency stabilization, although possible [69], is very difficult. Fortunately, stabilization of  $k_{\text{eff}}$  does not require two individual optical frequencies ( $\omega_1$  and  $\omega_2$ ) to be very stable, but only the difference between them ( $\omega_1 - \omega_2$ ). In practice, frequency  $\omega_2$  is generated from  $\omega_1$  by frequency shifting  $\omega_1$  with a microwave frequency  $\approx \omega_{eg}$  which is ultra stable and locked to frequency standard such as Rubidium clock. There does exist a certain requirement of this single frequency ( $\omega_1$ ) stability, typically only at kHz level, which is much easier to implement.

## 3.2 Interferometer Phase Shift

In atom interferometer, the direct observable from the measurement sequence is the population ratio of two atomic states, which reflects the differential phase obtained through two interfering paths. The desired information, such as acceleration, gravity,

rotation rate, can be inferred from this differential phase. It is therefore essential to determine the linkage between the differential phase shift and the physical quantities.

There are many different approaches to derive the interferometer phase output terms. In this section, we will focus on the  $\pi/2 - \pi - \pi/2$  sequence (see figure 3.2) but our analysis is generic and can be applied to any interferometer sequence with slight modifications.

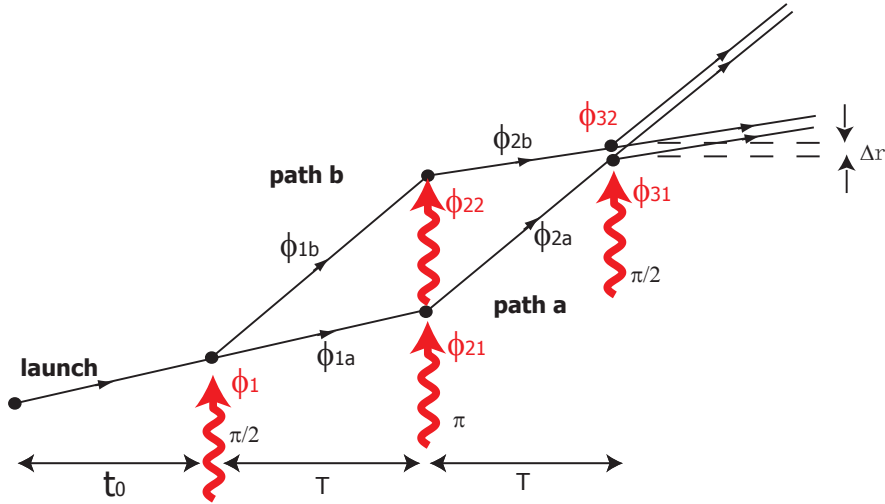


Figure 3.2: Interferometer phase and recoil diagram of  $\pi/2 - \pi - \pi/2$  sequence.

### 3.2.1 Path Integral Approach

Path-Integral approach is the most commonly used method to derive atom interferometer phase output. Detailed explanation can be found in [70] and [50]. Generally speaking, the differential phase between two interfering paths can be broken down into three parts: the laser phase at each pulses, the atom path phase due to the free evolution of the wavepackets, and the separation phase associated with the partial overlap of the two wavepackets:

$$\Delta\phi_{\text{total}} = \Delta\phi_{\text{laser}} + \Delta\phi_{\text{path}} + \Delta\phi_{\text{sep}}. \quad (3.17)$$

The laser interaction phase  $\Delta\phi_{\text{laser}}$  is associated with the atom's interactions with the light. As pointed out in section 3.1, the interaction time, or Raman pulse length, is orders of magnitude shorter than the interferometer sequence length. In the analysis of atom interferometer, the short-pulse limit is often assumed so that the pulse length is negligibly small. In this limit, the time evolution of the two atomic state amplitudes during on-resonance Raman pulse is given by

$$c_g(t + \tau) = \cos(\Omega_{\text{eff}}\tau/2)c_g(t) - i \sin(\Omega_{\text{eff}}\tau/2)e^{i\phi}c_e(t) \quad (3.18)$$

$$c_e(t + \tau) = -i \sin(\Omega_{\text{eff}}\tau/2)e^{-i\phi}c_g(t) + \cos(\Omega_{\text{eff}}\tau/2)c_e(t) \quad (3.19)$$

where  $\phi$  is the local phase of the external electric field. For a  $\pi$ -pulse,  $\tau = \tau_\pi = \pi/\Omega_{\text{eff}}$  and

$$c_g(t + \tau_\pi) = -ie^{i\phi}c_e(t) \quad (3.20)$$

$$c_e(t + \tau_\pi) = -ie^{-i\phi}c_g(t) \quad (3.21)$$

For a  $\pi/2$ -pulse,  $\tau = \tau_\pi/2$  and

$$c_g(t + \tau_\pi/2) = \frac{1}{\sqrt{2}}[c_g(t) - ie^{i\phi}c_e(t)] \quad (3.22)$$

$$c_e(t + \tau_\pi/2) = \frac{1}{\sqrt{2}}[-ie^{-i\phi}c_g(t) + c_e(t)] \quad (3.23)$$

The  $\pi/2$ -pulse splits each state into an equal super-position of two states. When an atom transfers from the ground state to the excited state, it picks up a laser phase  $e^{-i\phi}$ ; likewise, the atom picks up a laser phase of  $e^{i\phi}$  when it is driven from the excited state to the ground state. Atom does not pick up laser phase when it does not undergo a transition from one state to the other. The phase pickup rule is the same in  $\pi$ -pulse case which transfers atom from one state to the other completely. There are five laser phases involved in the full  $\pi/2 - \pi - \pi/2$  interferometer sequence, and will be discussed in detail later in this section.

The path phase  $\Delta\phi_{\text{path}}$  is associated with the phase shift picked up by the atom during its free propagation from  $\mathbf{r}_1 = \mathbf{r}(t_1)$  to  $\mathbf{r}_2 = \mathbf{r}(t_2)$  between Raman pulses, and

can be calculated along its classical trajectory using its Lagrangian:

$$\phi_{\text{path}} = \frac{1}{\hbar} \int_{t_1}^{t_2} L[\mathbf{r}(t), \dot{\mathbf{r}}(t)] dt, \quad (3.24)$$

where the Lagrangian is defined as  $L[\mathbf{r}(t), \dot{\mathbf{r}}(t)] = \frac{1}{2}m\dot{\mathbf{r}}^2 - V(\mathbf{r})$ .

The separation phase arises from the fact that the two wavepackets going through two arms of the interferometer do not overlap perfectly. The wavepacket is often assumed to be plane wave and the de Broglie waves from two wavepackets interfere with a differential phase of

$$\phi_{\text{sep}} = \frac{\mathbf{p} \cdot \Delta \mathbf{r}}{\hbar} \quad (3.25)$$

where  $\mathbf{p}$  is momentum of atom and  $\Delta \mathbf{r}$  is the spatial separation of the two wavepackets. A common question here is which velocity is supposed to be used in this calculation, because there are four different wavepackets at the end of atom interferometer sequence and they all can have different velocities, in principle. This will be discussed later in this section.

Here, the total differential phase of classical  $\pi/2 - \pi - \pi/2$  sequence is calculated as an example. Figure 3.2 shows a general diagram of this sequence. Assume that the atom starts in the ground state at time  $t = 0$  such that  $c_g(0) = 1$  and  $c_e(0) = 0$ . Table 3.1 illustrates the evolution of phase along two interferometer arms.

The two arms combine and then interfere, so the final state amplitudes are given by (with separation phase added)

$$c_g(2T + 2\tau) = -(e^{-i\phi_{1a} - i\phi_{21} - i\phi_{2a} + i\phi_{31} + i\phi_{\text{sep}}^g} + e^{-i\phi_1 - i\phi_{1b} + i\phi_{22} - i\phi_{2b}})/2 \quad (3.26)$$

$$c_e(2T + 2\tau) = -i(e^{-i\phi_{1a} - i\phi_{21} - i\phi_{2a} + i\phi_{\text{sep}}^e} - e^{-i\phi_1 - i\phi_{1b} + i\phi_{22} - i\phi_{2b} - i\phi_{32}})/2 \quad (3.27)$$

The final state populations therefore are calculated as

$$|c_g(2T + 2\tau)|^2 = [1 + \cos(\phi_g)]/2 \quad (3.28)$$

$$|c_e(2T + 2\tau)|^2 = [1 - \cos(\phi_e)]/2 \quad (3.29)$$

Time	Arm $a$	Arm $b$
0	$c_g = 1$	
$\tau/2$	$c_g = 1/\sqrt{2}$	$c_e = -ie^{-i\phi_1}/\sqrt{2}$
$T + \tau/2$	$c_g = e^{-i\phi_{1a}}/\sqrt{2}$	$c_e = -ie^{-i\phi_1 - i\phi_{1b}}/\sqrt{2}$
$T + 3\tau/2$	$c_e = -ie^{-i\phi_{1a} - i\phi_{21}}/\sqrt{2}$	$c_g = -e^{-i\phi_1 - i\phi_{1b} + i\phi_{22}}/\sqrt{2}$
$2T + 3\tau/2$	$c_e = -ie^{-i\phi_{1a} - i\phi_{21} - i\phi_{2a}}/\sqrt{2}$	$c_g = -e^{-i\phi_1 - i\phi_{1b} + i\phi_{22} - i\phi_{2b}}/\sqrt{2}$
$2T + 2\tau$	$c_e = -ie^{-i\phi_{1a} - i\phi_{21} - i\phi_{2a}}/2$ $c_g = -e^{-i\phi_{1a} - i\phi_{21} - i\phi_{2a} + i\phi_{31}}/2$	$c_g = -e^{-i\phi_1 - i\phi_{1b} + i\phi_{22} - i\phi_{2b}}/2$ $c_e = ie^{-i\phi_1 - i\phi_{1b} + i\phi_{22} - i\phi_{2b} - i\phi_{32}}/2$

Table 3.1: Evolution of phase during a  $\pi/2 - \pi - \pi/2$  interferometer sequence. The atom starts in pure ground state and  $\tau$  denotes  $\pi$ -pulse length and  $T$  is the time between Raman pulses, commonly referred as interrogation time. Refer to figure 3.2 for explanation of the variables.

where

$$\phi_g = -\phi_{1a} - \phi_{21} - \phi_{2a} + \phi_{31} + \phi_1 + \phi_{1b} - \phi_{22} + \phi_{2b} + \phi_{\text{sep}}^g \quad (3.30)$$

$$\phi_e = -\phi_{1a} - \phi_{21} - \phi_{2a} + \phi_{32} + \phi_1 + \phi_{1b} - \phi_{22} + \phi_{2b} + \phi_{\text{sep}}^e \quad (3.31)$$

We will prove these two phases are exactly the same, so that the total population ( $|c_g(2T + 2\tau)|^2 + |c_e(2T + 2\tau)|^2$ ) is always 1. Before going into detailed discussion, we first note that this output phase can be categorized into three parts: 1) path phase

$$\phi_{\text{path}} = \phi_{1b} + \phi_{2b} - \phi_{1a} - \phi_{2a} \quad (3.32)$$

as the path integral going through the loop of interferometer diagram; 2) separation phase ( $\phi_{\text{sep}}^g$  and  $\phi_{\text{sep}}^e$ ); and 3) laser phase which two states get different quantities:

$$\phi_{\text{laser}}^g = \phi_1 - \phi_{21} - \phi_{22} + \phi_{31} \quad (3.33)$$

$$\phi_{\text{laser}}^e = \phi_1 - \phi_{21} - \phi_{22} + \phi_{32} \quad (3.34)$$

We now look at the separation phase in more detail. Suppose before the last  $\pi/2$ -pulse, wavepacket in the path  $2b$  is moving at velocity  $\mathbf{v}_g$ , and wavepacket in the

path  $2a$  is moving at velocity  $\mathbf{v}_e$ , and their separation is  $\Delta\mathbf{r}$  (pointing from path  $b$  to path  $a$ ). The last  $\pi/2$  pulse has a wave vector of  $\mathbf{k}_{\text{eff}}$  thus gives a recoil kick of  $\mathbf{v}_{r3} = \hbar\mathbf{k}_{\text{eff}}/m$ . Due to the separation of two wavepackets,  $\phi_{31}$  and  $\phi_{32}$  are not the same and are related by

$$\phi_{31} = \phi_{32} + \mathbf{k}_{\text{eff}} \cdot \Delta\mathbf{r}. \quad (3.35)$$

The velocities of the two wavepackets in ground state after the last  $\pi/2$ -pulse are  $\mathbf{v}_g$  and  $(\mathbf{v}_e - \mathbf{v}_{r3})$  (in the ideal case these two velocities are exactly the same). The separation phase of the ground state is calculated using the average speed of these two velocities (detailed treatment can be found in the next section)

$$\phi_{\text{sep}}^g = \frac{m(\mathbf{v}_g + \mathbf{v}_e - \mathbf{v}_{r3})}{2} \cdot \Delta\mathbf{r}/\hbar. \quad (3.36)$$

Similarly

$$\phi_{\text{sep}}^e = \frac{m(\mathbf{v}_e + \mathbf{v}_g + \mathbf{v}_{r3})}{2} \cdot \Delta\mathbf{r}/\hbar. \quad (3.37)$$

It's clear that the excited state and ground state have different laser phase and separation phase contribution, but it's easy to prove that the sum of these two is exactly the same:

$$\phi_{\text{sep}}^g + \phi_{\text{laser}}^g = \phi_{\text{sep}}^e + \phi_{\text{laser}}^e \quad (3.38)$$

As a result, the total phase of the two states are exactly the same, as expected.

It is important to note that breaking down total phase into these three categories is totally artificial, but is convenient for calculation and modeling. There is no physical quantity that corresponds to the laser phase or path phase, and the only physically observable quantity is the total phase. One can transform all the calculation into a moving frame, and finds both the path phase and separation phase are different, thus making the path phase and separation phase totally arbitrary and meaningless. The sum of these two phases is still the same as in the lab frame, and special relativity guarantees the laser phase is an invariant under Lorentz transformation. The total phase, or the population ratio between two states, is thus also an invariant under inertial frame transformation, as it should be.

Another interesting thought is that in fact we do not detect atoms right after the

last  $\pi/2$ -pulse. The states continue to evolve after the last  $\pi/2$ -pulse. In non-ideal condition, the final interferometer phase does depend on the detection time. However, for all practical experiments in atom interferometry, the two wavepackets following two arms of interferometer must be reasonably close in space and their classical velocities must be very close too (if not, then recoil kicks during interferometer must have introduced a large thermal-velocity-dependent phase and that would wash out the interferometer contrast). This ensures the phase dependence on the detection time is negligibly small, and therefore interferometry phase calculation often assumes the detection is right after the interferometer sequence.

### 3.2.2 Wave Packet Approach

While the path integral approach introduced in the previous section is a powerful tool, it is unable to predict the loss of interferometer contrast due to the partial overlap of wavepackets at the end of interferometer. While partial overlap of wavepackets is not present with the ideal interferometer sequence and condition, it is an important topic in general and one of the important aspects in decorrelating platform noise in dynamic environment. We here discuss a wavepacket approach to calculate the interferometer phase output as well as the contrast reduction. Since the math in this approach is more complicated, only the case of free space condition (no gravity) will be discussed, but the results of contrast reduction is generic even with potential energy added. Similar analysis can be found in [71] and [72].

We start with wave packet representation. After loading atoms, every atom can be treated as a coherent Gaussian wave packet. We express Gaussian wave packet in space:

$$\psi(x) = \frac{1}{\sqrt{\sqrt{\pi}x_a}} \exp\left(-\frac{x^2}{2x_a^2}\right) \cdot \exp\left(i\frac{m}{\hbar}v_c(x-x_0)\right), \quad (3.39)$$

where  $x_0$  and  $v_c$  are classical position and velocity of this atom,  $x_a$  is the initial coherent length on the order of hundreds of nanometers. Above can be expressed as

a set of momentum eigenstates (normalization factor omitted):

$$\psi(x) = \int_{-\infty}^{+\infty} dv \cdot \exp\left(-\frac{(v - v_c)^2}{2v_a^2}\right) \cdot \exp\left(i\frac{m}{\hbar}v(x - x_0)\right), \quad (3.40)$$

where

$$v_a = \frac{\hbar}{mx_a}. \quad (3.41)$$

(Momentum spread and spatial spread are inversely proportional, or uncertainty principle.) Each momentum eigenstate:

$$\psi_v(v, x, t = 0) = \exp\left(i\frac{m}{\hbar}v(x - x_0)\right) \quad (3.42)$$

is in fact a de Broglie plane wave. Because this is a free particle, its phase velocity is  $v/2$ , so this eigenstate evolves as:

$$\psi_v(v, x, t) = \exp\left(i\frac{m}{\hbar}v\left(x - x_0 - \frac{v}{2}t\right)\right). \quad (3.43)$$

This is simply just the solution of Schrodinger equation to a free particle. Now we can look at the wave packet evolution:

$$|\psi(x, t)|^2 = \left| \int_{-\infty}^{+\infty} dv \cdot \exp\left(-\frac{(v - v_c)^2}{2v_a^2}\right) \psi_v(v, x, t) \right|^2 \quad (3.44)$$

$$\propto \exp\left(-\frac{(x - x_0 - v_c t)^2}{x_a^2 + v_a^2 t^2}\right) \quad (3.45)$$

So at time  $t$ , the wave packet center is at  $(x_0 + v_c t)$ , as expected; and also wave packet size becomes  $(x_a^2 + v_a^2 t^2)^{1/2}$ .

### 3.2.2.1 Wave Packet and Atom Cloud

To find ensemble behavior, we have to integrate over  $v_c$  and  $x_0$ . We assume they obey the following Gaussian distribution:

$$f_v(v_c) \propto \exp\left(-\frac{v_c^2}{2v_t^2}\right), \quad (3.46)$$

$$f_x(x_0) \propto \exp\left(-\frac{x_0^2}{x_t^2}\right), \quad (3.47)$$

and the physical meaning of  $v_t$  and  $x_t$  will be interpreted later in this section.

As a result, the atom number distribution over space is:

$$N(x) \propto \int_{-\infty}^{+\infty} dx_0 f_x(x_0) \int_{-\infty}^{+\infty} dv_c f_v(v_c) \cdot \exp\left(-\frac{(x - x_0 - v_c t)^2}{x_a^2 + v_a^2 t^2}\right) \quad (3.48)$$

$$\propto \exp\left(-\frac{x^2}{r(t)^2}\right), \quad (3.49)$$

where

$$r(t)^2 = x_a^2 + x_t^2 + (v_a^2 + 2v_t^2)t^2. \quad (3.50)$$

Classically, for collisionless expansion over a time  $t$  the 1/e-radius of the atom cloud is (see, e.g. [73] page 59)

$$r(t)^2 = r(0)^2 + 2\frac{k_b T_a}{m} t^2. \quad (3.51)$$

Compared with our wave packet result, we have initial cloud size:

$$r_0 = r(0) = \sqrt{x_a^2 + x_t^2}. \quad (3.52)$$

And to define classical temperature  $T_a$ , compare the second term in the  $r(t)$  formula, we have:

$$T_a = \frac{m}{2k_b}(v_a^2 + 2v_t^2), \quad (3.53)$$

We define rms thermal velocity:

$$v_{\text{rms}} = \sqrt{\frac{k_b T_a}{m}} = \sqrt{v_t^2 + v_a^2/2}. \quad (3.54)$$

We'll see later that our experiment cannot discriminate  $x_a$  from  $x_t$ , nor  $v_a$  from  $v_t$ . The interferometer contrast and phase only depends on  $r_0$  and  $v_{\text{rms}}$ .

### 3.2.2.2 Wave Packet Interacting with Raman Pulse

For a momentum eigenstate, the de Broglie wave phase is:

$$\phi(v, x, t) = \frac{m}{\hbar}v \left( x - x_0 - \frac{v}{2}t \right). \quad (3.55)$$

Suppose at  $t = t_0$ , it receives a  $\pi$  pulse, the spatially dependent laser phase  $\phi_L(x)$  is imprinted on the de Broglie wave:

$$\phi_L(x) = k_{\text{eff}}(x - x_0 - v_c t_0) + \phi_1, \quad (3.56)$$

where we reference laser phase to the wave packet center where laser phase is  $\phi_1$ . The de Broglie wave phase right after pulse is (Note  $k_{\text{eff}} = mv_r/\hbar$  where  $v_r$  is recoil velocity):

$$\phi'(v, x, t_0) = \phi(v, x, t_0) + \phi_L(x) = \frac{m}{\hbar}(v + v_r)x + C \quad (3.57)$$

where constant  $C$  does not depend on  $v, x, t$ . The physical meaning of this expression is that Raman pulse transforms the de Broglie phase spatial dependence to a new wave number  $m(v + v_r)/\hbar$ , which is expected from the recoil kick. The de Broglie wave phase then continues to evolve after the pulse:

$$\phi'(v, x, t) = \phi'(v, x, t_0) - \frac{m}{\hbar} \frac{(v + v_r)^2}{2} (t - t_0). \quad (3.58)$$

We can verify how the new wave packet evolves:

$$|\psi'(x, t)|^2 = \left| \int_{-\infty}^{+\infty} dv \cdot \exp\left(-\frac{(v - v_c)^2}{2v_a^2}\right) e^{i\phi'(v, x, t)} \right|^2 \quad (3.59)$$

$$\propto \exp\left(-\frac{(x - x_0 - v_c t - v_r(t - t_0))^2}{x_a^2 + v_a^2 t^2}\right) \quad (3.60)$$

Wave packet center motion agrees with classical picture, and Raman pulse does not change how the wave packet size increases.

We now proceed with two concrete examples of calculation of complete interferometer sequence. Results will be used in later sections.

### 3.2.2.3 Example 1: $\delta T$ -Scan

We prepare atoms at  $t = 0$ , and do first  $\pi/2$ -pulse at  $t = t_0$ , second  $\pi$ -pulse at  $t = t_0 + T$ , third  $\pi/2$ -pulse at  $t = t_0 + 2T + \delta T$ , and finally detect at  $t = t_f$ . This is a sequence we used to characterize interferometer SNR. we will see  $t_0$  and  $t_f$  eventually drop out from the expression. For simplicity, we do the calculation in space, i.e., no potential energy. We first look at a single atom which starts as a wave packet. A momentum eigenstate  $\psi_v(v, x, t = 0)$  evolves over time, and goes through three Raman pulses. Using rules in the previous section, we can calculate the wave function of this eigenstate at detection:  $\psi_{v1}(v, x, t = t_f)$  and  $\psi_{v2}(v, x, t = t_f)$  for two paths respectively. The wave packets at detection from two paths are:

$$\psi_1(x) = \int_{-\infty}^{+\infty} dv \cdot \exp\left(-\frac{(v - v_c)^2}{2v_a^2}\right) \psi_{v1}(v, x, t = t_f) \quad (3.61)$$

$$\psi_2(x) = \int_{-\infty}^{+\infty} dv \cdot \exp\left(-\frac{(v - v_c)^2}{2v_a^2}\right) \psi_{v2}(v, x, t = t_f) \quad (3.62)$$

The probability of detecting this atom is:

$$P_a = \int_{-\infty}^{+\infty} dx |\psi_1(x) + \psi_2(x)|^2 \quad (3.63)$$

Despite the fact that the calculation is indeed complicated, the result is simple:

$$P_a = \frac{1}{2} + \frac{1}{2} \exp\left(-\frac{v_r^2 \cdot \delta T^2}{4x_a^2}\right) \cos\left(\phi_1 - \phi_{21} - \phi_{22} + \phi_{31} - \frac{mv_r^2 \delta T}{2\hbar}\right), \quad (3.64)$$

where 4 laser phases are defined at wave packet center, so:

$$\phi_1 - \phi_{21} - \phi_{22} + \phi_{31} = k_{\text{eff}} \delta T (v_c + v_r/2) + \phi_{\text{scan}} \quad (3.65)$$

( $\phi_{\text{scan}}$  is some extra laser phase shift used for scanning fringe.). Plug in the laser phase, we see  $P_a$  is a function of  $v_c$ :

$$P_a(v_c) = \frac{1}{2} + \frac{1}{2} \exp\left(-\frac{v_r^2 \cdot \delta T^2}{4x_a^2}\right) \cos(\phi'_{\text{scan}} - k_{\text{eff}} v_c \delta T) \quad (3.66)$$

To get normalized atom number at this output port, we integrate over  $v_c$

$$P = \int_{-\infty}^{+\infty} dv_c f_v(v_c) \cdot P_a(v_c) = (1 + \chi \cos(\phi_{\text{scan}}))/2 \quad (3.67)$$

where contrast:

$$\chi = \exp\left(-\frac{\delta T^2}{(2x_a/v_r)^2}\right) \exp\left(-\frac{\delta T^2}{2/(k_{\text{eff}}v_t)^2}\right) \quad (3.68)$$

With a little math,

$$\chi = \exp\left(-\frac{\delta T^2}{2/(k_{\text{eff}}v_{\text{rms}})^2}\right) \quad (3.69)$$

This means, by measuring contrast envelope of  $\delta T$ -scan, we can not distinguish wave packet momentum spread from classical thermal velocity. Only the overall velocity distribution rms, or classical temperature, matters. This  $\delta T$ -scan provides a way to measure atom cloud temperature (see section 7.3).

### 3.2.2.4 Example 2: Pitch Noise

Suppose Raman axis is  $x$ , and beams are steered by some small angle  $\theta_1, \theta_2, \theta_3$  in the  $xOy$  plane during three pulses. The wave packet calculation has to be done in two dimensions  $x$  and  $y$ , but to the 1st order, the  $x$  part of the interferometer is nicely closed and does not decrease contrast, so we only have to deal with the  $y$  part. In the following equations,  $v_c$  is wave packet center velocity along  $y$  axis. The probability of detecting a single atom in the ground state is

$$P_a(v_c, y_0) = \frac{1 + \chi_1 \cos \phi(v_c, y_0)}{2}, \quad (3.70)$$

where single atom contrast is:

$$\begin{aligned} \chi_1 &= \exp\left(-\frac{(\theta_1 - 2\theta_2 + \theta_3)^2 v_r^2}{4v_a^2}\right) \\ &\cdot \exp\left(-\frac{[t_0(\theta_1 - 2\theta_2 + \theta_3) + 2T(-\theta_2 + \theta_3)]^2 v_r^2}{4x_a^2}\right), \end{aligned} \quad (3.71)$$

and single atom phase depends on  $v_c$  and  $y_0$  (2nd order  $\theta_i^2$  terms ignored):

$$\phi(v_c, y_0) = 2k_{\text{eff}}v_c(\theta_3 - \theta_2)T + k_{\text{eff}}(y_0 + v_ct_0)(\theta_1 - 2\theta_2 + \theta_3) + \phi_{\text{scan}}. \quad (3.72)$$

By integrating  $P_a(v_c, y_0)$  over  $v_c$  and  $y_0$ , we get overall ensemble contrast  $\chi$ :

$$\begin{aligned} \chi &= \chi_1 \cdot \exp\left(-\frac{(\theta_1 - 2\theta_2 + \theta_3)^2 k_{\text{eff}}^2 x_t^2}{4}\right) \\ &\cdot \exp\left(-\frac{[t_0(\theta_1 - 2\theta_2 + \theta_3) + 2T(-\theta_2 + \theta_3)]^2 k_{\text{eff}}^2 v_t^2}{2}\right) \end{aligned} \quad (3.73)$$

With a little math...

$$\begin{aligned} \chi &= \exp\left(-\frac{(\theta_1 - 2\theta_2 + \theta_3)^2 k_{\text{eff}}^2 r_0^2}{4}\right) \\ &\cdot \exp\left(-\frac{[t_0(\theta_1 - 2\theta_2 + \theta_3) + 2T(-\theta_2 + \theta_3)]^2 k_{\text{eff}}^2 v_{\text{rms}}^2}{2}\right). \end{aligned} \quad (3.74)$$

So in this pitch noise model, final contrast only depends on the initial cloud size  $r_0$  and classical rms thermal velocity  $v_{\text{rms}}$ . Interestingly, contrast depends on  $t_0$ , the time between the 1st Raman pulse and cooling (or the last incoherent process event). This pitch noise contrast calculation is one of the foundations of platform noise decorrelation model.

### 3.2.3 Acceleration Measurement

The analysis of the simplest atom interferometer sequence  $\pi/2 - \pi - \pi/2$  is outlined above. We now proceed with concrete result. It can be shown that [70] in a uniform gravity field  $\mathbf{g}$ , this interferometer sequence gives a gravity-dependent phase, no matter what the initial spatial location or initial thermal velocity any particular atom has:

$$\phi = \mathbf{k}_{\text{eff}} \cdot \mathbf{g}T^2, \quad (3.75)$$

where  $T$  is the interrogation time. The center  $\pi$ -pulse steers wavepackets back together and interfere, cancels the initial thermal velocity terms in phase. This is important in that all the atoms in the ensemble coherently contribute to the acceleration-dependent phase measurement, resulting in a significantly boosted signal-to-noise ratio (SNR) without losing interference contrast.

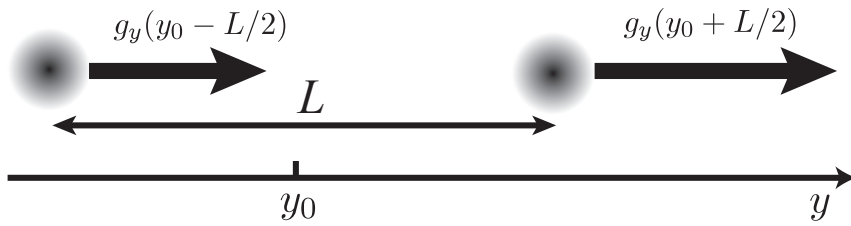


Figure 3.3: Gravity Gradient Measurement

By simultaneously making two gravity measurements spatially separated by a distance  $L$  (baseline, see figure 3.3), the gravity gradient along the Raman beam axis can be derived:

$$T_{yy}(y_0) \approx \frac{g_y(y_0 + L/2) - g_y(y_0 - L/2)}{L}. \quad (3.76)$$

Here  $g_y(y)$  denotes the component of gravity along Raman beam axis and  $y_0$  is the midpoint of these two accelerometers. As mentioned in section 1.1.2, platform noise is largely canceled in gravity gradient measurement, so gradiometer is therefore advantageous in dynamic environment such as survey.

Essentially, the atom accelerometer measures the relative motion between inertial frame, which is defined by the atom de Broglie wave, and the lab frame, which is defined by Raman beams referencing to the delivery optics mounted on the platform. Depending on the actual scenario, the atom accelerometer can be used to measure platform acceleration, or surrounding gravity, or a combination of both. When two acceleration measurements are made simultaneously, the optical coupling by Raman beams not only makes the atom gradiometer baseline easily extendable, but also enables a large common-mode platform noise rejection.

### 3.3 Raman Beam Path Asymmetry

As mentioned in section 3.1, although two-photon transition requires two independent optical frequencies  $\omega_1$  and  $\omega_2$ , only the frequency difference ( $\omega_1 - \omega_2$ ) is required to be ultra stable to make a precision measurement. The individual optical frequency does not need to be ultra stable. While it is true that the stability of frequency difference must be at sub-Hz level, the individual optical frequency cannot be arbitrary. It has to be in a certain range and relatively stable to ensure stable ac Stark shift and other things. Besides that, Raman beam path asymmetry puts an even more restrict constrains on the stabilities of  $\omega_1$  and  $\omega_2$ .

We assume  $\omega_1$  is generated from an optical-frequency-lock setup, and  $\omega_2$  is generated from  $\omega_1$  with a microwave frequency offset  $\omega_{eg}$ :

$$\omega_2 = \omega_1 - \omega_{eg}. \quad (3.77)$$

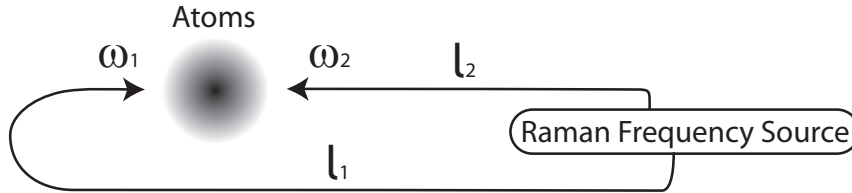


Figure 3.4: Raman beam path asymmetry for single sensor.

Here we assume the noise in  $\omega_{eg}$  is negligibly small. Figure 3.4 shows a generic Raman beam scheme typically in atom interferometry experiment. Because the distances between atom and the frequency source of Raman beams are different, the phases the atom sees from the two beams are not generated at exactly the same time. From the diagram, we know that at time  $t_1$ :

$$\phi_1(t_1) = \int_0^{t_1 - l_1/c} \omega_1(t) dt \quad (3.78)$$

$$\phi_2(t_1) = \int_0^{t_1 - l_2/c} \omega_2(t) dt \quad (3.79)$$

The effective laser phase imprinted by the two-photon Raman transition is

$$\begin{aligned}\phi_{\text{eff}}(t_1) &= \phi_1(t_1) - \phi_2(t_1) = \int_{t_1-l_2/c}^{t_1-l_1/c} \omega_1(t)dt + \int_0^{t_1-l_2/c} \omega_{eg}dt \\ &\approx \omega_1(t_1)\Delta l/c + \phi_{eg}(t_1 - l_2/c),\end{aligned}\quad (3.80)$$

where  $\Delta l = l_2 - l_1$  is the path imbalance of two Raman beams, and  $\phi_{eg}$  is the microwave oscillator phase which is ultra stable and will be ignored in this analysis.

With the standard  $\pi/2 - \pi - \pi/2$  sequence, the  $\omega_1$ -dependent laser phase contribution is (ignoring all other constant and relatively stable phase terms):

$$\Delta\phi = (\omega_1(t_1) - 2\omega_1(t_1 + T) + \omega_1(t_1 + 2T))\Delta l/c \quad (3.81)$$

Assume noise characteristic in  $\omega_1(t)$  is primarily much shorter time-scale than  $T$ , and its standard deviation is  $\delta_\omega$ , then

$$\delta_{\Delta\phi} = \sqrt{6}\delta_\omega\Delta l/c. \quad (3.82)$$

The phase noise therefore scales with Raman beam asymmetry  $\Delta l$ . This was illustrated in an ultra-short  $T$  experiment as shown in figure 3.5.

In practice, often two sensors make measurements simultaneously and the differential phase between them is the desired measurement quantity. The simplified Raman beam path diagram is shown in figure 3.6, and the  $\omega_1$ -dependent terms in the differential phase is:

$$\Delta\phi = 2(\omega_1(t_1) - 2\omega_1(t_1 + T) + \omega_1(t_1 + 2T))L/c, \quad (3.83)$$

and noise

$$\delta_{\Delta\phi} = 2\sqrt{6}\delta_\omega L/c. \quad (3.84)$$

For our typical measurement,  $L \approx 1$  m, and  $\delta_{\Delta\phi}$  is required to be around or below 1 mrad. This puts an upper limit on the noise of single optical frequency  $\omega_1$  on the order of 10 kHz. It is therefore essential to have a cavity-locked laser as the master Raman light source to make our precision gravity gradient measurement.

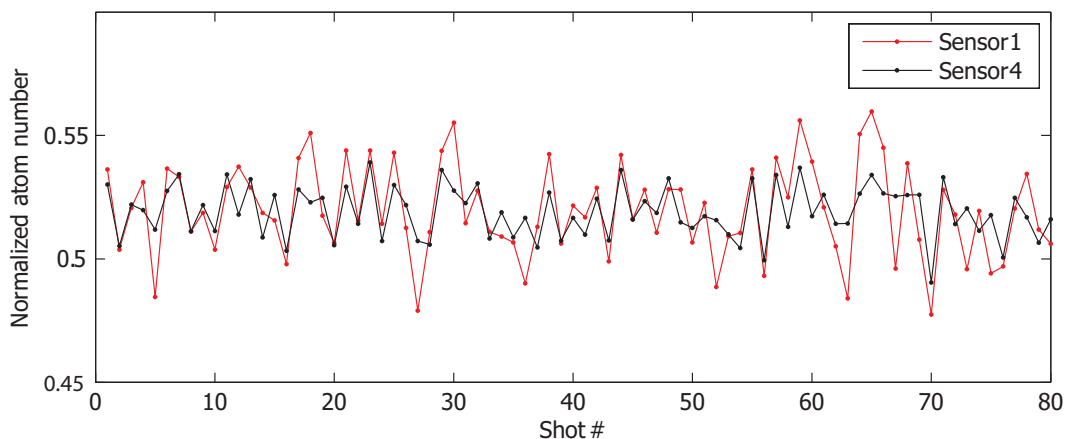


Figure 3.5: Ultra-short  $T$  illustrating Raman beam path asymmetry: a  $T = 70 \mu\text{s}$   $\pi/2 - \pi - \pi/2$  atom interferometer sequence is programmed, and the Raman phase is switched between pulses such that the interferometer phase output is near the middle of the fringe. Time record of two sensors are captured individually, and Sensor 4 clearly shows smaller noise (SNR of 60 in Sensor 4 compared to 24 in Sensor 1) because two Raman beams reach Sensor 4 with more balanced path lengths. Experiment also shows that when additional fibers are added in the Raman beam path such that Sensor 1 has more balanced Raman beam paths, Sensor 4 becomes noisier than Sensor 1.

### 3.4 Multi-Photon Sequence

Besides the simplest  $\pi/2 - \pi - \pi/2$  pulse sequence, more advanced pulse sequences can be used to measure rotation or enhance acceleration measurement sensitivity. The  $\pi/2 - \pi - \pi - \pi/2$  sequence is often used for rotation rate sensing [45, 48]. Here we discuss the “next-level-up” multi-photon sequence in acceleration measurements:  $4\hbar k$  sequence which is shown in figure 3.7.

For the  $4\hbar k$  sequence, time between the first two optical  $\pi$ -pulses and the last two

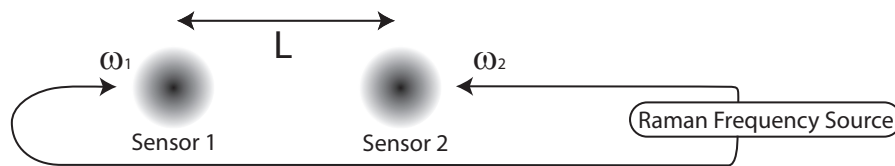


Figure 3.6: Raman beam path asymmetry for dual sensor setup.

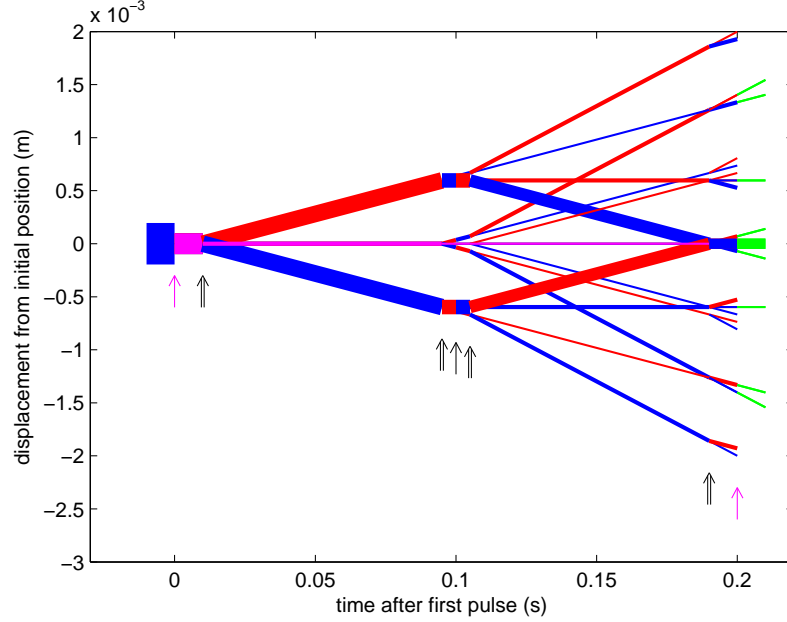


Figure 3.7: Recoil diagram of  $4\hbar k$  sequence:  $\pi/2(\text{microwave}) - \pi - \pi - \pi(\text{microwave}) - \pi - \pi - \pi/2(\text{microwave})$ . The center microwave pulse is used to reverse atomic states so that the optical Raman pulse direction ( $\mathbf{k}_{\text{eff}}$ ) does not have to be reversed. In this figure, blue line represents the ground state atoms path, while red represents the excited state. Optical  $\pi$ -pulse efficiency is set to 90% so many non-coherent atom states are produced outside the desired atom interferometer loop. All possible interferences are represented by green traces after the last microwave  $\pi/2$ -pulse, and different interference path has different inertial sensitivity.

must be the same ( $T$ ), and the time between the second and third optical  $\pi$ -pulses is denoted as  $T'$ . The phase output of this sequence is

$$\phi = 2\phi_1 - 2\phi_2 - 2\phi_3 + 2\phi_4 = 2k_{\text{eff}}a(T^2 + TT') \quad (3.85)$$

where acceleration  $a$  is measured along Raman beam axis ( $\mathbf{k}_{\text{eff}}$ ). In the limit of  $T' = 0$ , this  $4\hbar k$  sequence is twice more sensitive to acceleration compared with the simplest  $\pi/2 - \pi - \pi/2$  ( $2\hbar k$ ) sequence with the same interrogation time  $T$ . In our atomic fountain, it is fairly easy to reconfigure the pulses to do  $4\hbar k$  sequence, as shown in figure 3.8. Time  $T$  and  $T'$  can be varied by launching the atoms at different velocities.

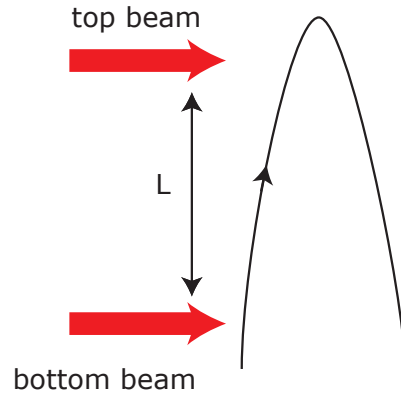


Figure 3.8: Fountain setup of  $4\hbar k$  sequence.

One interesting result is that no matter how fast we launch the atoms (as long as it reaches the top beam), the phase is always the same:

$$\phi = 2k_{\text{eff}}a(T^2 + TT') = 4k_{\text{eff}}aL/g. \quad (3.86)$$

It is therefore not advantageous to increase the launching velocity when reconfiguring system from  $2\hbar k$  sequence to  $4\hbar k$  sequence, if optical alignment is not to be touched.

# Chapter 4

## Experimental Apparatus

Our atom interferometry apparatus involves tremendous amount of engineering efforts. Previous generation of laboratory-size instrument (e.g. [52]) has been miniaturized and fitted in a boxtruck. A high level system block diagram is shown in figure 4.1. This chapter describes some details of our apparatus, including the control, electronics, laser, and sensor systems, as well as the boxtruck which enables the gravity gradient survey. Some parts that were thoroughly documented in [74] chapter 4 will only be briefly outlined here.

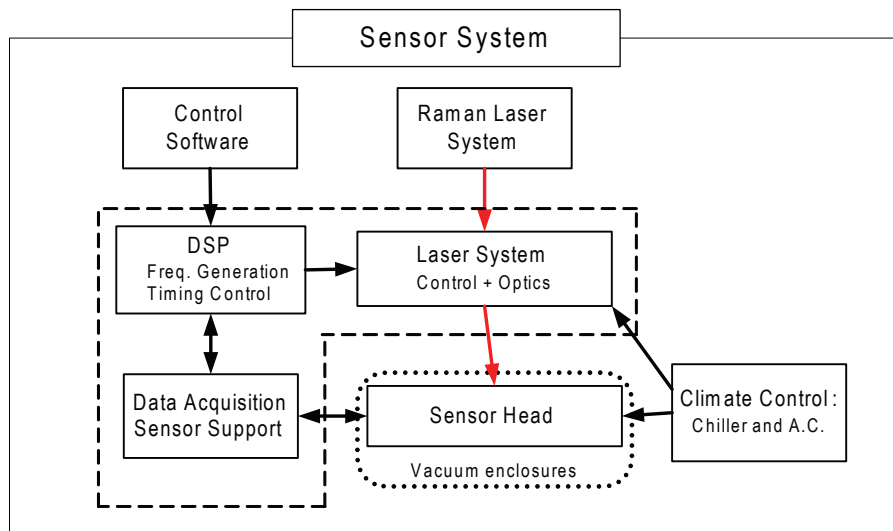


Figure 4.1: A high level sensor system block diagram.

## 4.1 Portable Laser System

The portable laser and electronics system in our apparatus are specifically designed to work together. All these systems are fitted in several aluminium frames which measure 9 inches by 15 inches. These frames can be stacked with cooling layer inserted (see figure 4.2). Among these frames are two optical frames, namely master laser frame and amplifier laser frame.

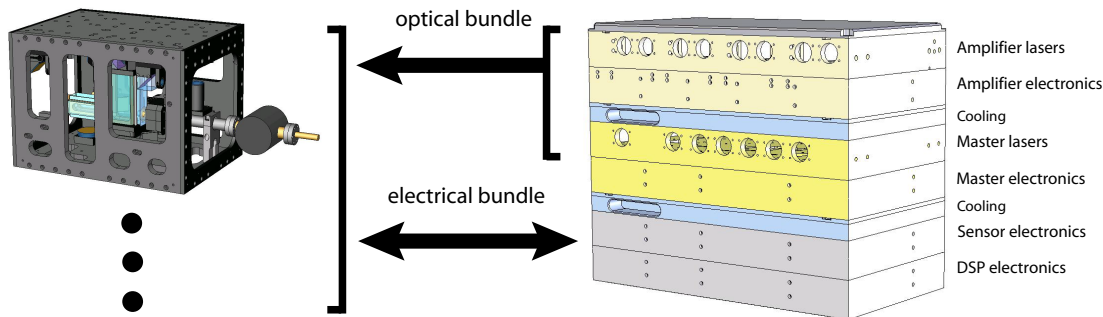


Figure 4.2: A picture of the laser and control electronics frame stack assembly. These frames deliver laser beams and electrical control signals to the sensors and also acquire signals from the sensors.

The 4 independent optical beams used to trap, cool, launch, and detect the Cs atoms are generated in the master laser frame using Yokogawa Distributed Bragg Reflector (DBR) and Eagleyard Distributed Feedback (DFR) diode lasers. The absolute frequencies are referenced internally to Cs transitions using saturation spectroscopy technique to derive an error signal for feedback to the diode laser [75]. The light from the master frame is fed into the amplifier frame where it is then amplified up to obtain the required power by a slave diode laser (SDL).

The narrow-linewidth light used to perform the stimulated Raman transitions is obtained from an external cavity-stabilized diode laser using Pound-Drever-Hall technique [76, 77]. Light from New Focus Vortex laser light is fed into a cavity with Finesse  $\sim 8000$ . The cavity error signal derived from the cavity reflection feeds back into Vortex laser. The cavity length and absolute frequency are fixed by locking to a Cs transition using similar technique as in the master laser frame (see figure 4.3).



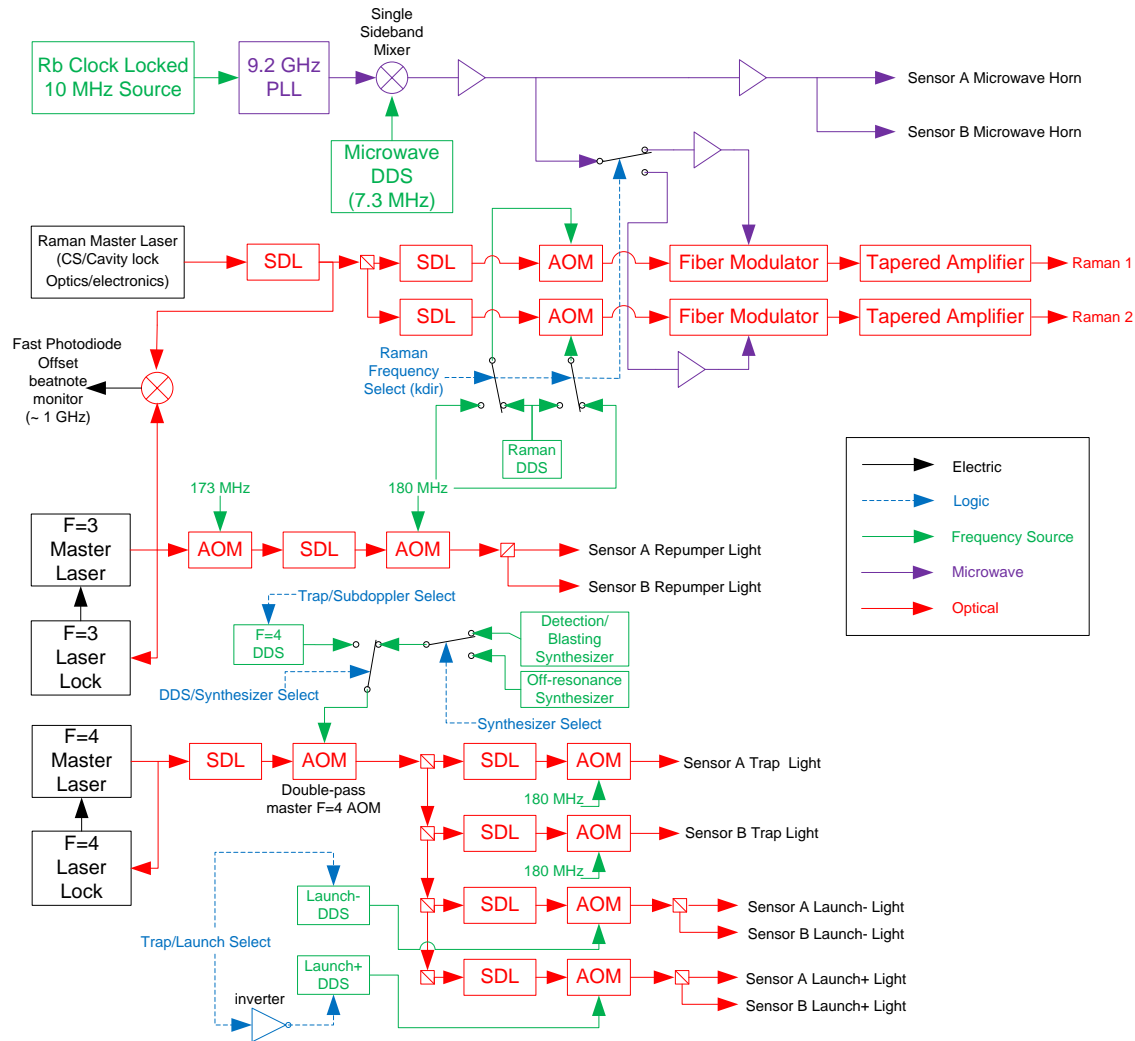


Figure 4.4: Block diagram of laser/frequency generation and distribution.

processor (DSP) which interfaces with the Windows application, sets the frequency and power desired at each point in the timing sequence. Programmable synthesizers and direct digital synthesizers (DDSs) are used to generate the variable frequencies required for microwave and optical sources (see figure 4.4). The system also manages operating parameters of the laser diodes including current and temperature, as well as all sensor parameters, including magnetic coils, Cs vapor and vacuum management, as discussed in the next section.

### 4.3 Sensor Hardware

The sensor, where Cs atoms are loaded to make measurement, is comprised of a Zerodur glass Cs vapor cell (see figure 4.5). Zerodur is perfectly machinable and polishable, has almost zero thermal expansion coefficient, and has very low Helium permeability, it is therefore perfect for optical access and stable atom interferometry operation. This glass cell is held under ultra-high vacuum (UHV), along with the delivery optics, Cs temperature control, magnetic coils for trapping, 3-axis bias magnetic coils, microwave horn, photo-detector, and 3-axis magnetometer. The hardware is mounted in an aluminium chassis and surrounded by two layers of Mu-metal magnetic shielding. In-sensor magnetometers are used to servo bias magnetic coil currents such that the magnetic field inside sensor head can be maintained at a constant value even when the apparatus is moved to another location with different earth magnetic field.

In order to reduce Raman beam steering effects, the sensor heads, Raman laser delivery optics, and Raman beam path are entirely contained within a low-vacuum ( $10^{-2}$  Torr) aluminium enclosure (see figure 4.6). This low-vacuum is maintained by a standard rotary-vane roughing pump. Hundreds of electrical signals are fed into the low-vacuum enclosure using a few multi-pin feedthroughs. Special procedure has been developed to retrofit the standard single-mode fibers to feedthrough the low-vacuum enclosure, without introducing air leakage or degrading optical performance. Two Raman beams are delivered to sensors using a few mirrors and a corner cube (see figure 4.6). Four critical mirrors and the corner cube have New Focus Picomotors



Figure 4.5: A picture of the Zerodur ultra-high vacuum cell.

mounted so that both Raman beam alignments can be fully controlled by computer.

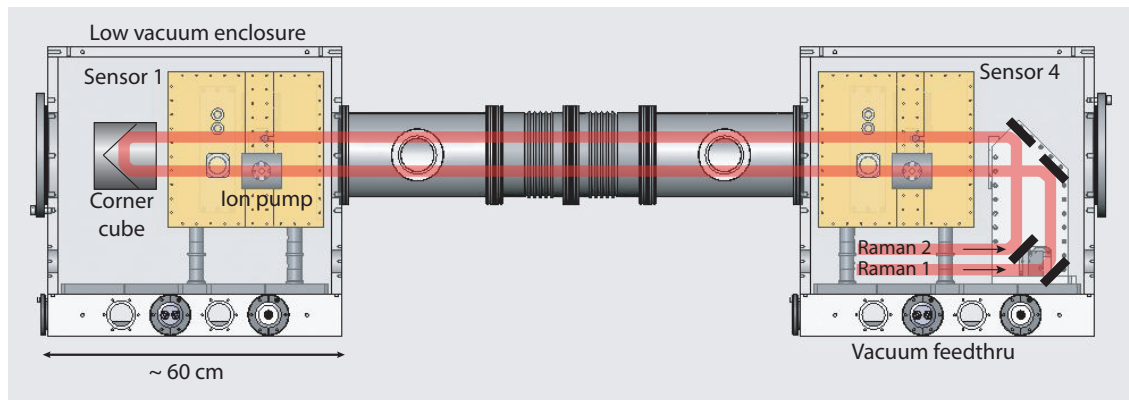


Figure 4.6: Schematic of the Raman laser delivery.

## 4.4 Mobile Laboratory in a Truck

The forementioned apparatus has been tested in the lab with convincing performance (see section 8.1), and was then moved into a boxtruck in order to conduct mobile gravity gradient measurement. All the supporting instruments are fitted inside truck, mostly using rack-mounts. The ambient temperature inside the truck is controlled with a wall-mount air conditioning unit and compressor, the latter being mounted on

the outside.

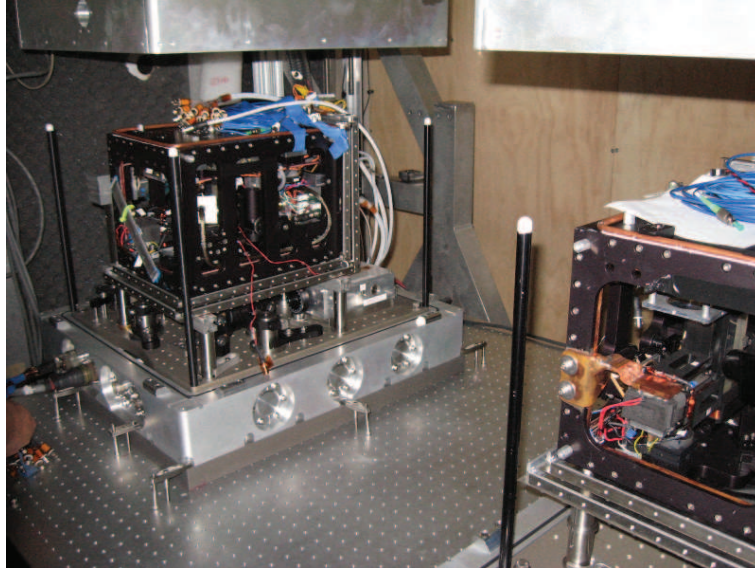


Figure 4.7: A picture of the experimental apparatus: low-vacuum enclosures are lifted to show the sensor heads. The bases of the low-vacuum enclosure are mounted down to the actively-stabilized platform inside the boxtruck.

The sensor heads and low-vacuum enclosures are mounted on top of a custom levelling platform (see figure 4.7) based on a 3-axis gimbal, which was developed by a mechanical engineering team. This platform is actively stabilized with a low-frequency servo loop using an LN250 inertial measurement unit (IMU) mounted on the platform. Another LN250 is mounted on the truck floor to provide feedforward signal to the platform control, particularly useful when truck is moving. This platform control system performs very well such that the sensor system is able to identify gravity gradient signature even when the truck is continuously moving [78].

The truck is equipped with an electric motor and a Differential Global Positioning System (DGPS). The electric motor is capable of smoothly driving the truck with a speed as low as 1 cm/s. DGPS provides centimeter-level accuracy of the truck position and can potentially be used to guide the truck motion and even the steering if a secondary DGPS is installed.

# Chapter 5

## Data Analysis

Precision measurement is often accompanied by a tremendous amount of work in data analysis. In our particular apparatus, we have learned that optimal processing algorithm can often squeeze out every last bit of instrument potential, and in certain cases provide more than 30% boost in system performance. This chapter outlines various data analysis methods and tools we used in the data processing, as well as some issues we identified and solved.

### 5.1 Ellipse Fitting

Ellipse fitting algorithm was initially studied in computer graphics [79] and then applied to atom interferometry to extract differential phase between two atomic sensors [80]. Suppose two sensors output signals (without noise):

$$\begin{cases} x = C_x + A_x \sin(\phi_c) \\ y = C_y + A_y \sin(\phi_c + \phi_d) \end{cases} \quad (5.1)$$

where  $\phi_c$  is the common phase (completely random in our apparatus) shared between two sensors and  $\phi_d$  is the differential phase that we are interested in. One can eliminate unknowns  $C_x, A_x, C_y, A_y, \phi_c$  and get:

$$Ax^2 + Bxy + Cy^2 + Dx + Ey + F = 0 \quad (5.2)$$

with  $B^2 - 4AC < 0$ , which is a general form of ellipse equation. The differential phase can be extracted from the coefficients:

$$\phi_d = \arccos\left(-\frac{B}{2\sqrt{AC}}\right), \quad (5.3)$$

with the convention that  $A$  and  $C$  are positive. With noise present in the data, the least-square-fitting provides an approximate method to extract the differential phase by minimizing the following quantity:

$$\sum_i (Ax_i^2 + Bx_iy_i + Cy_i^2 + Dx_i + Ey_i + F)^2, \quad (5.4)$$

where the sum goes through all the data points. To avoid trivial solution of all coefficient being zero, condition  $B^2 - 4AC = -1$  is commonly used as an additional constrain (for use with Lagrange multipliers) in the fitting. Likewise, condition  $F = 1$  can also be used in the case of sufficiently low noise (i.e. eyes can clearly trace out an ellipse). The advantage of using condition  $F = 1$  is that the algebra is simpler for implementation and results faster processing speed, particularly useful in real-time applications.

The above algorithm is often referred as “unconstrained ellipse fitting”. In certain cases, the offsets  $C_x, C_y$  and amplitudes  $A_x, A_y$  are known or predetermined by a clean measurement. As a result, one might want to carry out a “constrained ellipse fitting” by fixing the offsets and amplitudes. We first normalize the data in equation 5.1

$$\begin{cases} x_n = \frac{x - C_x}{A_x} = \sin(\phi_c) \\ y_n = \frac{y - C_y}{A_y} = \sin(\phi_c + \phi_d) \end{cases} \quad (5.5)$$

By eliminating  $\phi_c$ , we have

$$y_n^2 - 2x_ny_n \cos \phi_d + x_n^2 - 1 + \cos^2 \phi_d = 0. \quad (5.6)$$

Similarly, we can find optimal  $\phi_d$  using least-square-fitting by minimizing the following

quantity:

$$\sum_i (y_{ni}^2 - 2x_{ni}y_{ni} \cos \phi_d + x_{ni}^2 - 1 + \cos^2 \phi_d)^2. \quad (5.7)$$

This constrained ellipse fitting algorithm was verified and has much less systematic error when  $\phi_d$  is small, compared with unconstrained ellipse fitting. However it requires preknowledge of offsets and amplitudes, making it suitable only for non-realtime processing and certain data decorrelation cases. If not specified, “ellipse fitting” refers to unconstrained ellipse fitting throughout this thesis.

### 5.1.1 Ellipse Fitting Noise and Systematic Error

In experiment, we typically characterize system noise by taking the standard deviation of a time series of ellipse-fitting phases (per-ellipse phase noise). We sometimes want to compare this per-ellipse phase noise with some characteristic per-shot noise such as phase noise induced by Raman laser frequency instability. The conversion between per-ellipse phase noise and per-shot phase noise is not as trivial as just a simple  $\sqrt{N}$  factor (where  $N$  is the number of data points per ellipse). We approach this problem by simple simulation without worrying about the strict statistical model. The result with  $N = 20$  is shown in figure 5.1. This conversion factor is slightly lower than  $\sqrt{N}$ , indicating that ellipse fitting does not reach the limit of statistical error. This conversion factor is a function of per-shot noise  $\sigma_\phi$  and the differential phase  $\phi_d$ , but when  $\sigma_\phi$  is reasonably small, and  $\phi_d$  is reasonably away from 0 and  $\pi$ , the conversion factor is only a function of  $\phi_d$ .

The conversion factor is proportional to  $\sqrt{N}$ , therefore measurement sensitivity, or how fast one can integrate down the measurement noise, is independent of the  $N$  used in the data analysis (see figure 5.2). However, in practice, long-term system drift often kicks in as  $N$  increases. For our particular apparatus, sample characteristic can be found in [74], section 5.2.1, and  $N = 20$  is selected as the generic optimal value.

The other interesting aspect is the systematic error of ellipse fitting. Simulation shows (see figure 5.3) that ellipse fitting has nonnegligible systematic error (i.e., biased estimation) when phase noise is large. Also, we can see  $\phi_d = \pi/2$  is the desired condition for ellipse fitting because it results negligible systematic error and minimum

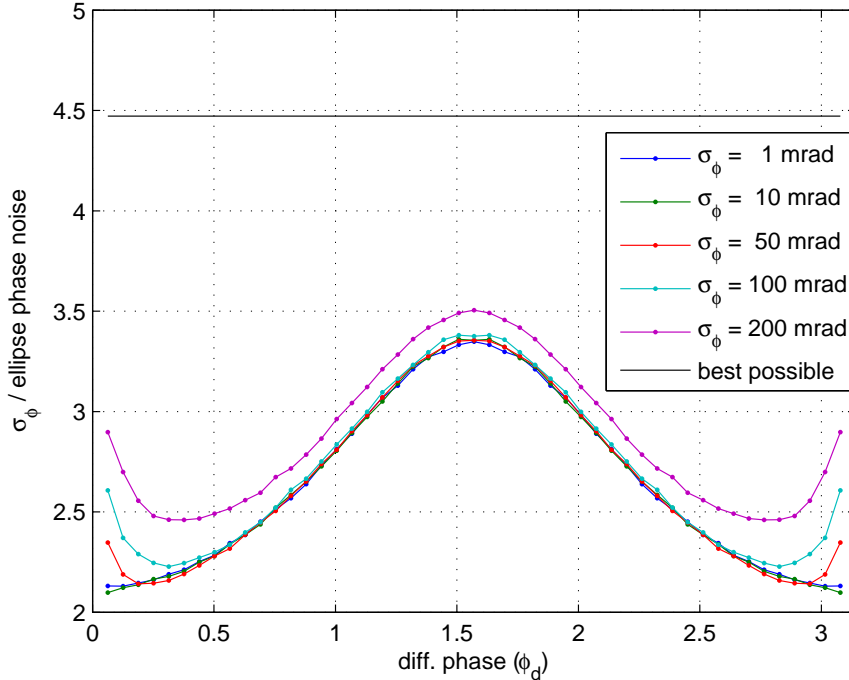


Figure 5.1: Ellipse fitting noise conversion factor from per-shot noise to per-ellipse noise. The number of points per ellipse ( $N$ ) is fixed at 20 in this simulation. This conversion factor is slightly lower than the statistical limit (best possible  $\sqrt{N}$ ), and is a function of per-shot noise  $\sigma_\phi$  and the differential phase  $\phi_d$ , but when  $\sigma_\phi$  is reasonably small, and  $\phi_d$  is reasonably away from 0 and  $\pi$ , the conversion factor is only a function of  $\phi_d$ .

per-ellipse phase noise.

The above analysis assumes phase-noise-only model. In practice, contrast noise can play a role in the system noise too (see, e.g. section 7.1.1). Detailed study has been done in comparison with Bayesian estimator algorithm [81].

### 5.1.2 Single Ellipse Fitting Residue

Phase noise can also be inferred from a single ellipse fitting residue, just like in the simplest linear fitting. In the case of ellipse fitting, the conversion from ellipse fitting residue to actual phase noise is not straightforward. One can certainly go through the

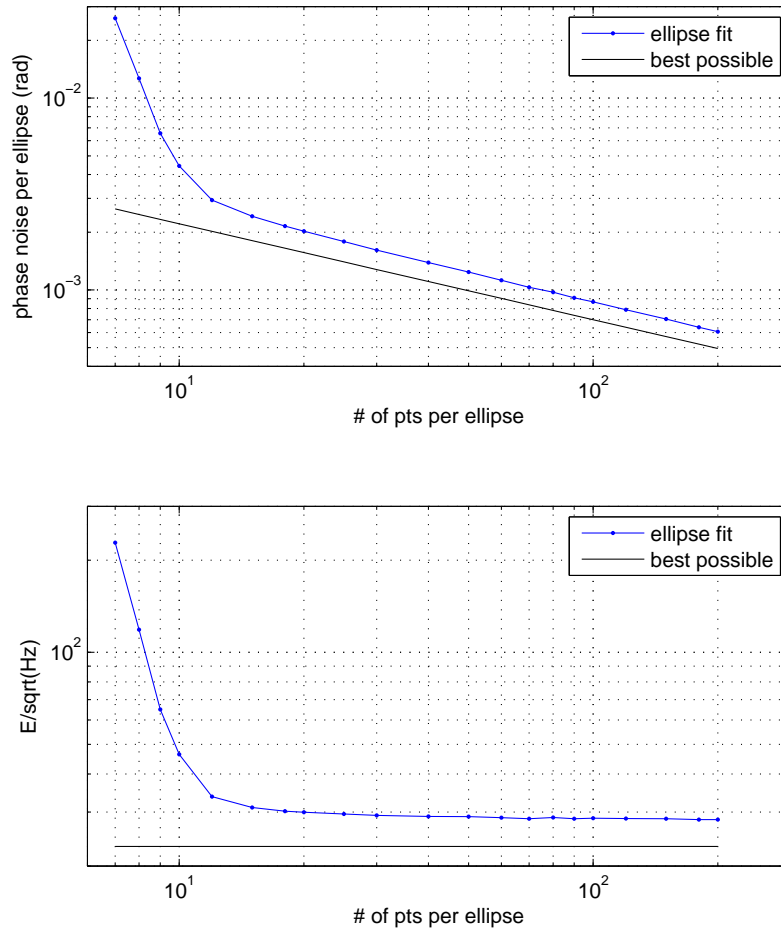


Figure 5.2: Ellipse fitting noise integration: the top figure shows how the phase noise per ellipse decreases proportionally as  $1/\sqrt{N}$ , therefore the interferometer sensitivity shown in the bottom figure is almost independent of  $N$  as long as  $N$  is reasonably large ( $N > 15$ ). Parameters in this simulation are: phase noise 7 mrad/shot, interrogation time  $T = 85$  ms, baseline  $L = 1.8$  m, and repetition rate 2.5 Hz.

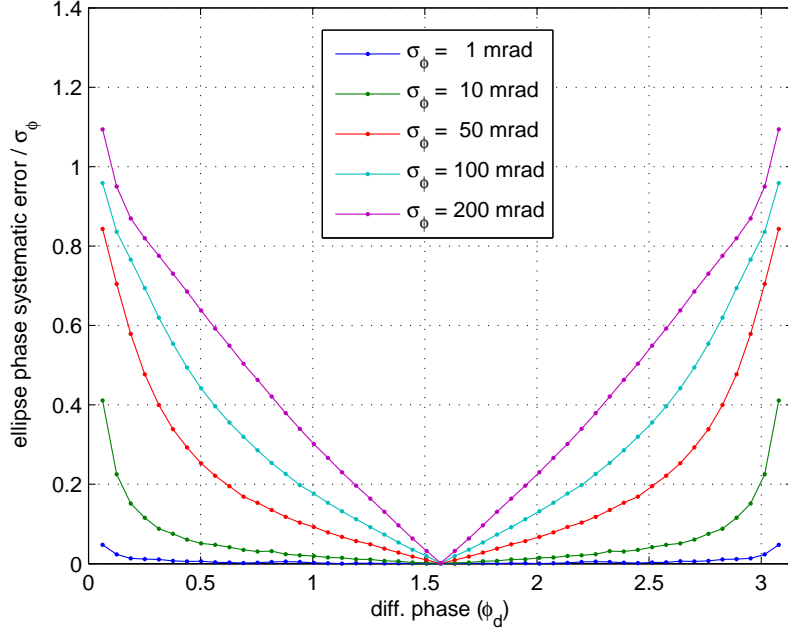


Figure 5.3: Ellipse fitting systematic error: the systematic error is normalized to the per-shot noise level to better illustrate the relationship.  $\phi_d = \pi/2$  is the desired condition for a phase-noise-dominated ellipse fitting.

statistical model with complicated integrals, but practically an empirical simulation is sufficient to give an order-of-magnitude estimation.

We first note that the mapping from per-shot phase noise  $\sigma_\phi$  to ellipse fitting residue  $r$  depends on the ellipse shape ( $A_x, A_y, \phi_d$ ) and the number of data points per ellipse ( $N$ , in the discussion below, it is fixed at 20). It does not seem a wise idea to re-run simulation for every particular ellipse shape. In order to get generic results with minimum amount of simulation, we first study a normalized case in which  $A_x = A_y = 1$ ,  $C_x = C_y = 0$ , and  $F = 1$ . In this case, residue  $r$  only depends on  $\phi_d$  and  $\sigma_\phi$ :

$$r = r(\phi_d, \sigma_\phi). \quad (5.8)$$

This function  $r(\phi_d, \sigma_\phi)$  can be empirically determined by a simulation. For any given  $\phi_d$  and  $\sigma_\phi$ , we first generate  $N = 20$  random data points, assuming only phase noise

is present:

$$\begin{cases} x_{ni} = \sin(\phi_c) \\ y_{ni} = \sin(\phi_c + \phi_d + \sigma_\phi X) \end{cases} \quad i = 1, 2, \dots, N \quad (5.9)$$

where  $\phi_c$  is uniformly distributed in  $[0, 2\pi)$ , and  $X$  is a random variable with standard normal distribution ( $\mu_X = 0, \sigma_X = 1$ ). We use the condition  $F = 1$  to fit an ellipse with coefficients  $A_t, B_t, C_t, D_t, E_t$ , and  $F_t = 1$ , and then find the residue for this particular dataset:

$$r_t^2 = \frac{1}{N} \sum_{i=1}^N (A_t x_{ni}^2 + B_t x_{ni} y_{ni} + C_t y_{ni}^2 + D_t x_{ni} + E_t y_{ni} + F_t)^2. \quad (5.10)$$

We repeat the same procedure many times and find the average residue:

$$r^2(\phi_d, \sigma_\phi) = \langle r_t^2 \rangle. \quad (5.11)$$

With a few points in  $\phi_d$  and  $\sigma_\phi$  space, we have a 2-D grid data of  $r = r(\phi_d, \sigma_\phi)$ , and 2-D interpolation can be used to find  $\sigma_\phi$  for any given  $r$  and  $\phi_d$ . We note here that for reasonable phase noise ( $\sigma_\phi < 100$  mrad),  $r$  goes almost linearly with  $\sigma_\phi$ , as expected, thus function  $r$  can be reduced to a linear function:

$$r = r(\phi_d, \sigma_\phi) = k(\phi_d) \sigma_\phi. \quad (5.12)$$

The phase-dependent linear coefficient  $k(\phi_d)$  is shown in figure 5.4.

For general ellipse, we first normalize data as in equation 5.5, and plug these  $x_n$  and  $y_n$  back into ellipse equation 5.2:

$$\begin{aligned} & A(A_x x_n + C_x)^2 + B(A_x x_n + C_x)(A_y y_n + C_y) \\ & + C(A_y y_n + C_y)^2 + D(A_x x_n + C_x) + E(A_y y_n + C_y) + F = 0. \end{aligned} \quad (5.13)$$

We can expand this equation to nominal form, normalize all coefficients to the new constant-term  $F'$ :

$$F' = AC_x^2 + BC_x C_y + CC_y^2 + DC_x + EC_y + F, \quad (5.14)$$

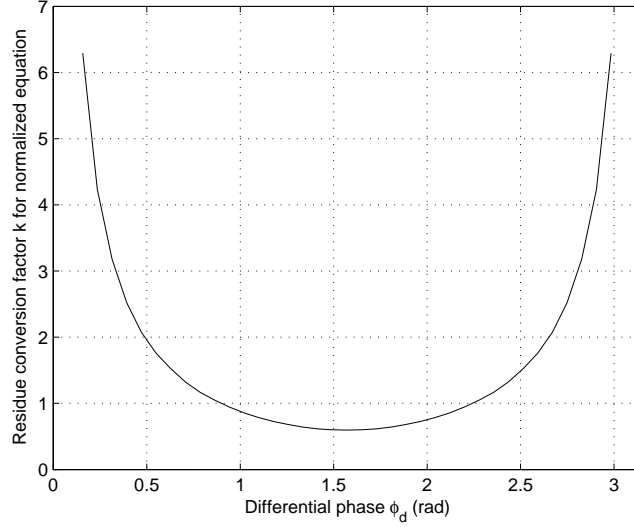


Figure 5.4: Ellipse fitting residue conversion factor for a normalized ellipse equation (equation 5.12). It converts a per-shot phase noise to average residue of a normalized ellipse fitting.

and then we have the normalized form of ellipse with “normalized residue”:

$$r_n^2(\phi_d, \sigma_\phi) = \frac{\frac{1}{N} \sum_{i=1}^N (Ax_i^2 + Bx_i y_i + Cy_i^2 + Dx_i + Ey_i + F)^2}{(AC_x^2 + BC_x C_y + CC_y^2 + DC_x + EC_y + F)^2}. \quad (5.15)$$

Using the normalized residue  $r_n$  and fitted ellipse phase  $\phi_d$ , we can infer  $\sigma_\phi$  by the normalized case simulation (equation 5.12). The actual  $1\sigma$ -confidence interval of  $\sigma_\phi$  can be determined approximately by  $\chi^2$  statistics with degree of freedom of  $N$ .

## 5.2 Phase and Contrast Noise Correction

In many precision measurement experiments, system has been thoroughly studied, and most noise sources have been identified and characterized, although noise itself is not controllable. Nevertheless, there are certain cases that noise can be measured thus decorrelated. For example, in our atom interferometer, Raman laser is locked to an external cavity, so laser frequency noise can be measured, in principle, by the

cavity lock error signal. Generally speaking, our atom interferometer noise can be categorized into two classes: phase noise (noise in  $\phi_d$  in equation 5.1) and contrast noise (noise in  $A_x$  and  $A_y$ ). This section discusses the algorithm to back out the phase noise and contrast noise when both of them are known by independent measurements.

We first modify equation 5.1 to include these two noise sources:

$$\begin{cases} x_d = C_x + A_x \chi \sin(\phi_c) \\ y_d = C_y + A_y \chi \sin(\phi_c + \phi_d + \Delta\phi) \end{cases} \quad (5.16)$$

where  $\chi$  is the reduced relative contrast ( $\chi < 1$ , same in two sensors for simplicity), and  $\Delta\phi$  is phase noise. The aim of phase and contrast noise correction algorithm is to transform original data point  $(x_d, y_d)$  onto the “correct” ellipse regardless of  $\phi_c$ . First of all, we can easily correct the contrast noise:

$$\begin{cases} x_{c0} = (x_d - C_x)/\chi + C_x \\ y_{c0} = (y_d - C_y)/\chi + C_y. \end{cases} \quad (5.17)$$

And phase correcting algorithm is shown below without derivation <sup>1</sup>:

$$\begin{cases} x_c = x_{c0} \\ y_c = (y_{c0} - C_y) \cos(\Delta\phi) \\ \quad + \frac{\sin(\Delta\phi)}{\sin(\phi_d + \Delta\phi)} \left( \frac{A_y}{A_x} (x_{c0} - C_x) - \cos(\phi_d + \Delta\phi) (y_{c0} - C_y) \right) + C_y. \end{cases} \quad (5.18)$$

This algorithm is graphically shown in figure 5.5. An important application of this contrast and phase error correction is platform motion decorrelation.

A proof-of-principle implementation of this algorithm is performed in a microwave clock experiment. Non-common random phase noise is intentionally added to the dual-fountain microwave clock by changing the bias magnetic field strength in only one of the sensors, and the bias current change (although random) is simultaneously recorded in order to decorrelate this phase noise. The  $|m_F = 0\rangle$  level of atoms used in the clock have second-order sensitivity to this magnetic field change, thus the

---

<sup>1</sup>Sean Roy first worked out this algorithm.

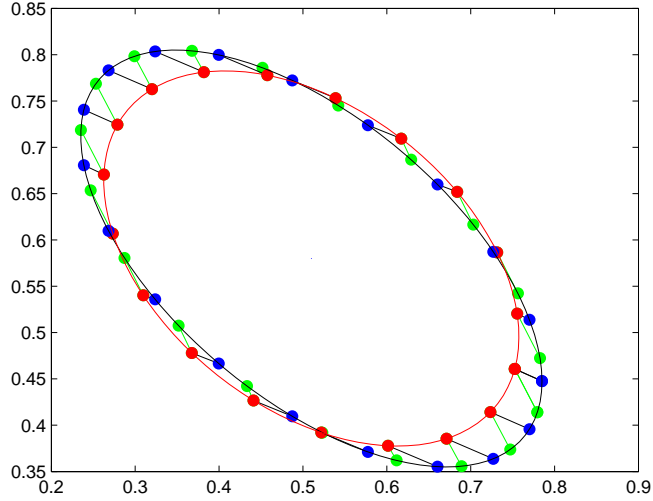


Figure 5.5: An example of phase and contrast noise correction. The clean data is shown as blue points on the correct blue ellipse. With contrast and phase noise, the data are shrunk and rotated onto the red ellipse. With correcting algorithm the data points are shifted to green points back on the correct ellipse, thus giving correct phase output by ellipse fitting. Note that the correcting algorithm does not necessarily correct data point back to the corresponding original point due to the lack of knowledge of common phase noise  $\phi_c$ .

differential phase change is:

$$\Delta\phi(\Delta B) = K(B_0 + \Delta B)^2 - KB_0^2 = k_1\Delta I + k_2(\Delta I)^2, \quad (5.19)$$

where we assume the bias field is proportional to the bias current applied:  $B \propto I$ . Coefficients  $(k_1, k_2)$  can be fitted by minimizing the total distance of corrected data points using the above model to the clean ellipse (which is acquired when no phase noise is added). The fitted coefficients  $(k_1, k_2)$  are very close to what the sensor geometry predicts, and this algorithm reduces the ellipse fitting noise from 39 mrad/ellipse rms to 1.1 mrad/ellipse (see figure 5.6), remarkably close to the microwave clock performance limit 0.5 mrad/ellipse. The remaining noise may result from the inhomogeneity of the magnetic field across the atom cloud.

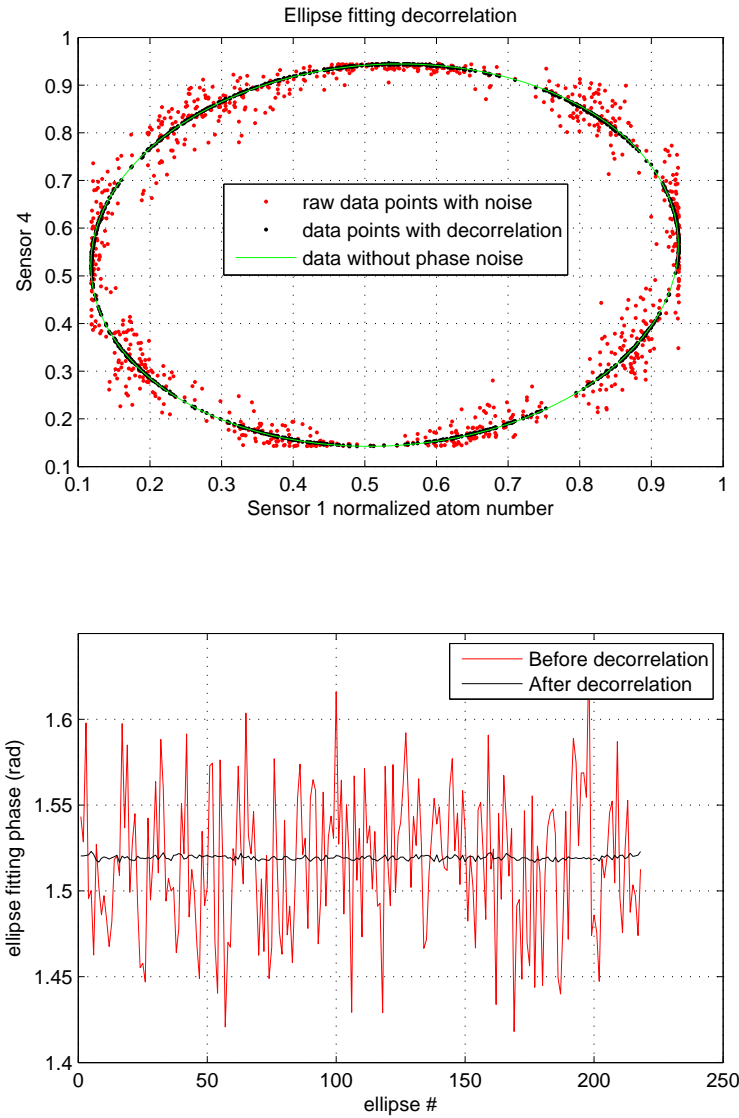


Figure 5.6: Phase correction in microwave clock: non-common phase noise is added to the microwave clock by changing the bias magnetic field in one of the two sensors. The bias current change is recorded simultaneously to decorrelate this phase noise by post-processing. The decorrelation algorithm reduces the ellipse fitting noise from 39 mrad/ellipse rms to 1.1 mrad/ellipse.

### 5.3 Direct Phase Extraction

The problem with ellipse fitting introduced in section 5.1 is that the least-square-fitting does not guarantee a bias-free differential phase extraction. In this section we discuss a simple bias-free differential phase extraction from the interferometer.

From normalized data in equation 5.5, we can eliminate  $\phi_c$  to get  $\phi_d$  by using inverse functions (this algorithm is sometimes referred as “asin algorithm” due to the involvement of arcsin function):

$$\phi_d = \begin{cases} |\arcsin(y) - \arcsin(x)| \\ \arccos(\cos(\pi - \arcsin(x) - \arcsin(y))) \end{cases} \quad (5.20)$$

Note special care has to be taken to ensure the result  $\phi_d$  is in the desired range of  $[0, \pi]$ . Eliminating  $\phi_c$  can also be done using mostly algebra:

$$\phi_d = \arccos\left(xy \pm \sqrt{(1-x^2)(1-y^2)}\right) \quad (5.21)$$

Equations 5.20 and 5.21 are essentially the same result. The fact that there are two solutions to a data point  $(x, y)$  is graphically shown in figure 5.7. There are many different ways to select the correct solution of the two. For example, we can choose the one closer to the conventional ellipse fitting result.

Experimental data  $x_i, y_i$  ( $i = 1, 2, \dots, N$ ) yields phase estimation  $\phi_{d(i)}$  using the above direct phase extraction. Phase noise is usually assumed to be normally distributed, so the optimal  $\phi_d$  is what maximizes the likelihood function, or what minimizes  $\sum_i (\phi_d - \phi_{d(i)})^2$ . In other words, the bias-free estimation of  $\phi_d$  is simply the average of all  $\phi_{d(i)}$ . In contrast, ellipse fitting algorithm does not guarantee this maximum likelihood, thus resulting biased estimation. Simulation also verifies that this direct phase extraction method yields the best possible integration of the phase error (i.e., Allan deviation integrates as  $\sigma_\phi/\sqrt{N}$ ), when only phase noise is present. However when contrast noise is also involved, this direct phase extraction is no longer an optimal way of extracting phase. In practice, those points near the middle of the fringe can be weighted more to give a more accurate estimation of differential phase,

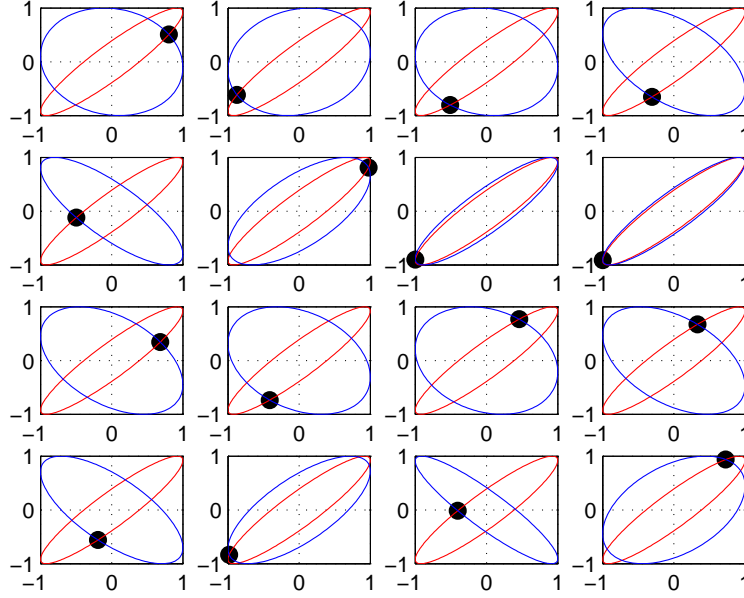


Figure 5.7: Direct phase extraction: two possible ellipses are calculated by given one data point on a predefined normalized ellipse (as in equation 5.5). The red ellipse is the actual predefined ellipse which is the same throughout all 16 trials.

therefore a simple weighting function can be the reciprocal of the product of the two  $\arcsin()$  function slopes in equation 5.20 (the steeper the slope is, the better phase sensitivity, thus requiring more weighting):

$$W(x, y) = \left| \frac{d[\arcsin(y)]}{dy} \cdot \frac{d[\arcsin(x)]}{dx} \right|^{-1} = \sqrt{(1-x^2)(1-y^2)}. \quad (5.22)$$

A more complete and systematic framework, namely the Bayesian estimation [81], has been established and preliminary theoretical study shows that it could reduce the noise and systematic error associated with ellipse fitting. Nevertheless, both the Bayesian estimation and the direct phase extraction method require preknowledge of data offsets  $C_x, C_y$  and amplitudes  $A_x, A_y$ , and are computationally intensive to implement, therefore it is rarely used in our experiment up to now.

## 5.4 Sine Fitting

Ellipse fitting provides a very robust way to extract differential phase between two atomic sensors, but in some cases, sine curve has to be fitted with single sensor data to extract individual phase of that sensor. This is particularly important in microwave clock study because common phase noise is usually very low and single sensor carries important clock phase information. Suppose we have  $N$  data points  $(x_n, y_n)$  that trace a sine curve roughly as

$$y_n \approx A \sin(\omega x_n + \phi) + C. \quad (5.23)$$

One can find optimal fitting parameters  $(A, \omega, \phi, C)$  by minimizing the following quantity:

$$P = \sum_{i=1}^N [y_n - A \sin(\omega x_n + \phi) - C]^2. \quad (5.24)$$

Fast least-square fitting cannot be applied here due to the nature of transcendental function, and this is a four parameter optimization problem which runs very slowly. However, if  $\omega$  is predetermined, then this optimization problem can be linearized:

$$P = \sum_{i=1}^N [y_n - A \cos(\phi) \sin(\omega x_n) - A \sin(\phi) \cos(\omega x_n) - C]^2. \quad (5.25)$$

Here linear coefficients  $(A \cos(\phi), A \sin(\phi), C)$  can be solved by fast least-square fitting, thus optimal  $(A, \phi, C)$  can all be determined. One can then vary  $\omega$  to find overall optimal solution. This one-parameter optimization algorithm runs very fast.

## 5.5 Dedrifting and Allan Deviation

Due to various drifting sources, absolute phase in atom interferometer is often drifting. The best method to average down a gravity gradient signal is to move the interferometer between the measurement spot and a reference spot in a regular interval. In this case, two methods of dedrifting algorithm have been developed to take out the absolute phase drifts.

Suppose we make a series of phase measurements  $\phi_i (i = 1, 2, 3, \dots)$  and we move interferometer every  $Y$  measurements. The phases measured at position A are:

$$y_i = \phi_{i+2Y \lfloor (i-1)/(2Y) \rfloor} \quad (5.26)$$

and the phases measured at position B are:

$$x_i = \phi_{i+Y+2Y \lfloor (i-1)/(2Y) \rfloor} \quad (5.27)$$

Without drift, the phase change between two positions can simply be averaged as  $M = \langle x_i \rangle - \langle y_i \rangle$ . The simplest direct subtraction method outputs gravity gradient phase as

$$M_i = x_i - y_i \quad (5.28)$$

but is susceptible to absolute phase drift.

If we assume the absolute phase drift is linear locally, one can model this drift with

$$\phi_n = \alpha_0 + \alpha_1 n. \quad (5.29)$$

And then

$$\begin{cases} y_i = x_i - \alpha_1 Y - M_i \\ y_{i+Y} = x_i + \alpha_1 Y - M_i \end{cases} \implies M_i = x_i - \frac{y_i + y_{i+Y}}{2}. \quad (5.30)$$

One can also model drift as quadratic:

$$\phi_n = \alpha_0 + \alpha_1 n + \alpha_2 n^2 \quad (5.31)$$

and this local curvature dedrifting method gives gravity gradient phase output as:

$$M_i = \frac{-y_i + 3x_i - 3y_{i+Y} + x_{i+Y}}{4}. \quad (5.32)$$

These two dedrifting algorithms have been successfully applied in our experiment to extract gravity gradient signal when fast thermal transient in absolute interferometer phase is present. However, the problem of the above two dedrifting algorithms is

that they underestimate short-term noise in Allan deviation. Suppose the system has no drift and the noise is completely white with standard deviation of  $\sigma$  per phase measurement. Without dedrifting, Allan variance of  $M$  simply goes as  $\sigma_M^2(N) = 2\sigma^2/N$  where  $N$  is the average window size. One can prove the Allan variance in local linear dedrifting algorithm is

$$\sigma_M^2(N) = \begin{cases} \frac{2\sigma^2}{N} \frac{3}{4} & N \leq Y/2 \\ \frac{2\sigma^2}{N} \left( \frac{1}{2} + \frac{Y}{8N} \right) & Y/2 \leq N \leq Y \\ \frac{2\sigma^2}{N} \left( 1 - \frac{3Y}{8N} \right) & Y \leq N \end{cases} \quad (5.33)$$

Local curvature dedrifting algorithm gives Allan variance as:

$$\sigma_M^2(N) = \begin{cases} \frac{2\sigma^2}{N} \frac{5}{8} & N \leq Y/2 \\ \frac{2\sigma^2}{N} \left( \frac{1}{4} + \frac{3Y}{16N} \right) & Y/2 \leq N \leq Y \\ \frac{2\sigma^2}{N} \left( 1 - \frac{9Y}{16N} \right) & Y \leq N \end{cases} \quad (5.34)$$

Apparently, local linear dedrifting underestimates short-term Allan variance by 25%, while local curvature dedrifting by 37.5%. However, both of them give correct estimation of long-term Allan variance. Figure 5.8 shows the short-term and long-term behavior of Allan deviation of different algorithms.

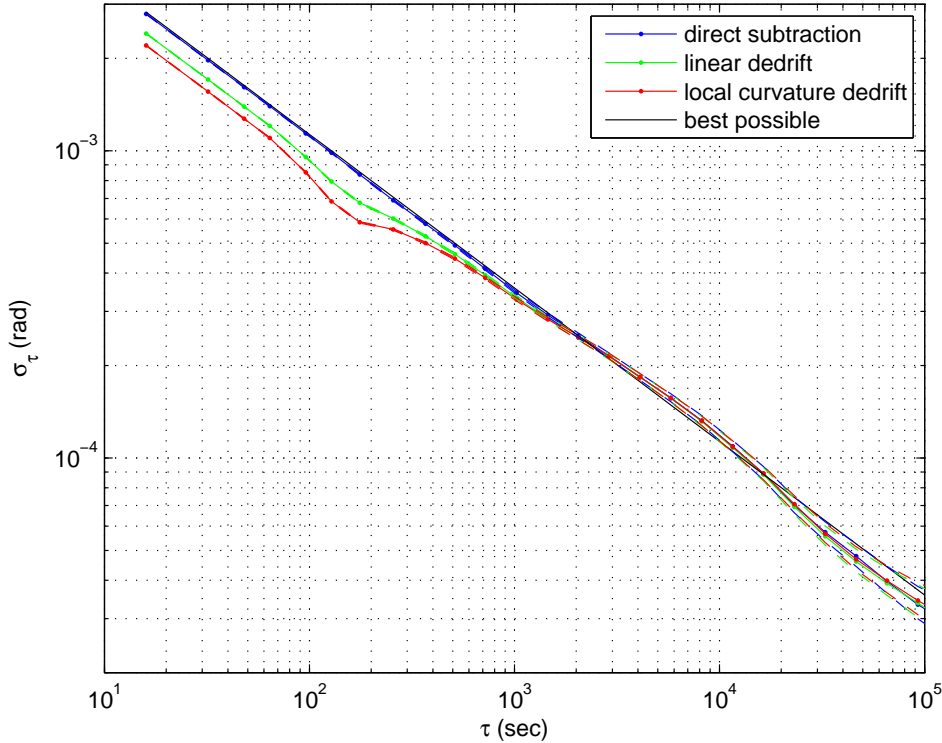


Figure 5.8: Allan deviation of dedrifted signal: different dedrifted algorithm has very different behavior at short-term end, confirmed by theory. Parameters in this simulation are: differential phase noise 2 mrad/ellipse, and sampling rate 9 sec/ellipse.

## 5.6 Derivative and Differential Measurement

We measure gravity gradient by the difference of signals from two sensors separated by a distance  $L$  called baseline:

$$T_{yy}(y_0) \approx \frac{g_y(y_0 + L/2) - g_y(y_0 - L/2)}{L}. \quad (5.35)$$

This, basically, is to approximate a derivative quantity measurement with a differential method, and is accurate only up to the first order (i.e., when  $T_{yy}(y)$  is linear). In practice, a post-processing algorithm can correct second-order error by using adjacent measurements, and is outlined below.

Suppose we make three measurements at location  $y = y_0 - y_L, y_0, y_0 + y_R$ :

$$\left\{ \begin{array}{l} \frac{g_y(y_0 - y_L + L/2) - g_y(y_0 - y_L - L/2)}{L} = T_0 - T_L \\ \frac{g_y(y_0 + L/2) - g_y(y_0 - L/2)}{L} = T_0 \\ \frac{g_y(y_0 + y_R + L/2) - g_y(y_0 - y_R - L/2)}{L} = T_0 + T_R \end{array} \right. \quad (5.36)$$

We assume quadratic trend of  $T_{yy}(y)$  near the location  $y = y_0$ , or:

$$g_y(y) = g_0 + g_1(y - y_0) + g_2(y - y_0)^2 + g_3(y - y_0)^3. \quad (5.37)$$

Here  $g_0$  is the background gravity which does not affect gravity gradient  $T_{yy}(y)$ , so with three unknowns and three equations in 5.36, we can solve:

$$T_{yy}(y_0) = \left. \frac{dg_y(y)}{dy} \right|_{y=y_0} = g_1 = T_0 + \frac{L^2(T_L y_R - T_R y_L)}{12y_L y_R (y_L + y_R)}, \quad (5.38)$$

where the second term is the correction term, which is on the order of 10 E, same order of magnitude as our measurement error. This algorithm is graphically shown in figure 5.9, and was used in data processing of our gravity gradient survey. In principle, more sophisticated correcting algorithm can be developed if the measurements are taken nearly continuously.

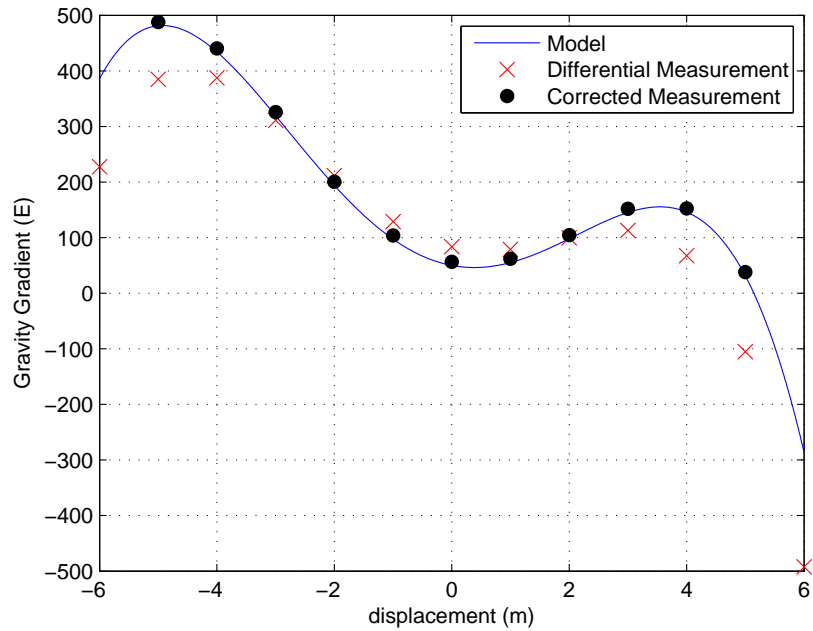


Figure 5.9: Differential measurement correction: measurement baseline is exaggerated in this simulation ( $L = 4$  m) to clearly show the correcting algorithm. This correction is very effective particularly near the peak or valley of the curve.

# Chapter 6

## Error Model

The fact that atom interferometer runs on the surface of the Earth which constantly rotates complicates the analysis. A complete model of atom interferometer sequence has to either use the Earth frame, in which case special care has to be taken because this is not an inertial frame, or use the inertial frame, in which case all the coordinates have to be carefully converted to and from lab (Earth) frame. Details of the Earth frame analysis can be found in [70]. In this section, we discuss a complete error model of the  $\pi/2 - \pi - \pi/2$  sequence. The analysis can be extended to general interferometer sequence, although the math becomes considerably more complicated when additional pulses are added.

### 6.1 Analysis in the Earth Frame

We first model the atom interferometer in the Earth frame. In the geocentric reference frame fixed to the surface of the Earth (see figure 6.1), the Lagrangian can be written as

$$L(\mathbf{r}, \mathbf{v}) = m \left( \frac{v^2}{2} + \mathbf{g} \cdot \mathbf{r} + \frac{1}{2} r_i T_{ij} r_j + \boldsymbol{\Omega} \cdot ((\mathbf{r} + \mathbf{R}) \times \mathbf{v}) + \frac{1}{2} (\boldsymbol{\Omega} \times (\mathbf{r} + \mathbf{R}))^2 \right), \quad (6.1)$$

where  $m$  is the atomic mass,  $\mathbf{R}$  is Earth radius vector from the center of Earth to the center of apparatus (origin of the coordinate system in figure 6.1), vector  $\mathbf{r}$  is the

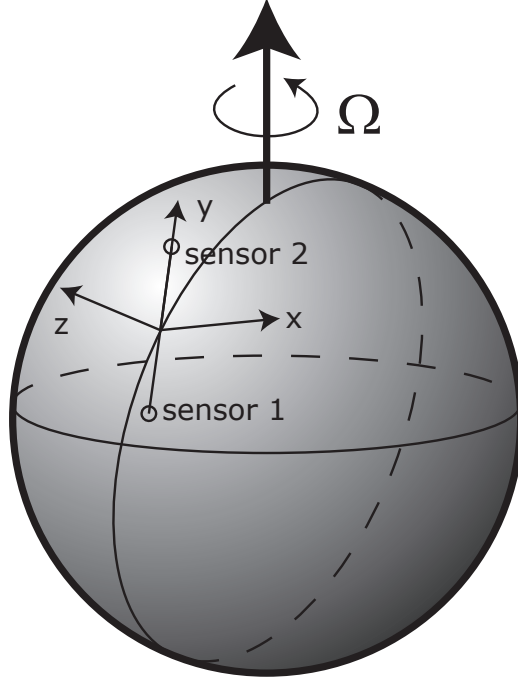


Figure 6.1: Earth frame coordinate system for the calculations. The  $z$ -axis is chosen to point away from the Earth center and the  $y$ -axis is along Raman axis connecting two sensors. Note that  $y$ -axis is not necessarily north-south.

displacement of the atom in the coordinate system,  $\boldsymbol{\Omega}$  is the Earth angular velocity vector,  $\mathbf{g}$  is acceleration due to local gravity, and  $T_{ij}$  is the gravity gradient tensor. We first evaluate the classical trajectories of atoms according to the classical equations of motion:

$$\frac{\partial^2 \mathbf{r}}{\partial t^2} = \mathbf{g} - 2\boldsymbol{\Omega} \times \frac{\partial \mathbf{r}}{\partial t} - \boldsymbol{\Omega} \times (\boldsymbol{\Omega} \times (\mathbf{r} + \mathbf{R})). \quad (6.2)$$

Using parameterized initial conditions of  $\mathbf{r} = \mathbf{r}_0$ , and  $\frac{\partial \mathbf{r}}{\partial t} = \mathbf{v}_0$ , we can obtain the general analytic expressions of the trajectories by solving the differential equation in Taylor expansion form. Terms up to the sixth order expansion in  $t$  are retained in the calculation to ensure practically maximum accuracy of the solution. The interferometer is subdivided into paths corresponding to the classical trajectories associated with wavepacket propagation between the interferometer optical pulses. The initial conditions for each path segment were determined from the final position

and velocity of the previous trajectory segment and the velocity recoil induced by the subsequent optical pulse.

The calculation of interferometer phase just follows the theory introduced in section 3.2. Briefly, the interferometer phase breaks down into three categories: laser phase is evaluated at the time of optical pulse, path phase is evaluated using full Lagrangian along classical trajectory, and separation phase is evaluated using the final separation and the average velocity of the wavepackets. Terms higher than the fifth order of  $t$  can be ignored in the intermediate steps to reduce the complexity of computation.

### 6.1.1 Symbols Used in the Model

We now introduce a concrete set of generic symbols used in our model. Refer to figure 3.2 for recoil diagram. Interferometer sequence is: launching at  $t = 0$ , 1st  $\pi/2$ -pulse at  $t = t_0$ , 2nd  $\pi$ -pulse at  $t = t_0 + T$ , 3rd  $\pi/2$ -pulse at  $t = t_0 + 2T$ , and finally detection at  $t = t_0 + 2T + t_d$ . The fact of  $t_d \neq 0$  adds another layer of complexity and as pointed out in section 3.2, setting  $t_d = 0$  is sufficiently accurate in all practical experiment modeling, so here we assume the detection is right after the 3rd pulse. The interferometer phases are as follows:

$$\phi_{\text{path}} = \phi_{1b} + \phi_{2b} - \phi_{1a} - \phi_{2a}, \quad (6.3)$$

$$\phi_{\text{laser}} = \phi_1 - \phi_{21} - \phi_{22} + \phi_{31}, \quad (6.4)$$

$$\phi_{\text{sep}} = \frac{m}{\hbar} \frac{\mathbf{v}_{3a}(t_0 + 2T) + \mathbf{v}_{2b}(t_0 + 2T)}{2} \cdot (\mathbf{r}_{2a}(t_0 + 2T) - \mathbf{r}_{2b}(t_0 + 2T)), \quad (6.5)$$

where  $\mathbf{v}_{3a}(t_0 + 2T)$  represents the velocity of the wavepacket from path 2a at detection, which is  $\mathbf{v}_{2a}(t_0 + 2T)$  plus the recoil kick added by the 3rd  $\pi/2$ -pulse. For a generic model, we assume atom initial conditions are:

$$\mathbf{r}_0 = (r_{ix}, r_{iy}, r_{iz}), \quad (6.6)$$

$$\mathbf{v}_0 = (v_{ix}, v_{iy}, v_{iz}). \quad (6.7)$$

These are initial conditions for a particular atom, and large part of that are from initial spatial spread of atom cloud and thermal velocities. We also denote the initial mean position and mean velocity of the atom cloud as:

$$\mathbf{r}_0^* = (r_{ix}^*, r_{iy}^*, r_{iz}^*), \quad (6.8)$$

$$\mathbf{v}_0^* = (v_{ix}^*, v_{iy}^*, v_{iz}^*), \quad (6.9)$$

and those primarily depends on platform noise during launching. We will see in the following section that  $\mathbf{r}_0$  and  $\mathbf{v}_0$  are used in individual interferometer contrast calculation, and once that is done, the interferometer phase noise only depends on  $\mathbf{r}_0^*$  and  $\mathbf{v}_0^*$ .

The Raman beam wave vector is ideally along  $y$ -axis but can have jitter and non-ideal alignment. We assume Raman beam wavevectors at the time of three pulses are:

$$\mathbf{k}_j = (k_{jx}, k_{\text{eff}} + k_{jy}, k_{jz}), \quad (6.10)$$

where  $j = 1, 2, 3$  representing three pulses. Here  $k_{\text{eff}}$  is the magnitude of the wavevector:  $|\mathbf{k}_j| = k_{\text{eff}}$ , so

$$\frac{k_{jy}}{k_{\text{eff}}} = -\frac{1}{2} \left( \frac{k_{jx}^2}{k_{\text{eff}}^2} + \frac{k_{jz}^2}{k_{\text{eff}}^2} \right), \quad (6.11)$$

so  $k_{jy}$  is second-order term in angular jitter, as expected. Sometimes we may also want to express Raman beam wavevector in terms of platform angular jitter:

$$k_{jx} = -k_{\text{eff}}\theta_{jz}, \quad (6.12)$$

$$k_{jz} = k_{\text{eff}}\theta_{jx}, \quad (6.13)$$

where  $j = 1, 2, 3$ . Here  $\theta_{jx}$  represents rotation around  $x$ -axis (pitch) while  $\theta_{jz}$  is yaw rotation. Note that roll angular jitter  $\theta_{jy}$  does not change Raman beam direction thus is not important here. Nevertheless,  $\theta_{jy}$  is important in calculating atom cloud initial condition and Raman window wedge effects.

The earth rotation:

$$\mathbf{\Omega} = (\omega_x, \omega_y, \omega_z), \quad (6.14)$$

where  $\omega_x$  represents rotation rate around  $x$ -axis (pitch),  $\omega_y$  is roll rotation rate, and  $\omega_z$  is yaw rotation rate. In other words, they are simply the Earth angular velocity vector projected onto three axes and  $|\boldsymbol{\Omega}| \approx 7 \times 10^{-5}$  rad/s.

The local gravity is

$$\mathbf{g} = (0, 0, g_z), \quad (6.15)$$

with  $g_z \approx -9.8$  m/s.

The earth radius vector:

$$\mathbf{R} = (0, 0, R), \quad (6.16)$$

with  $R \approx 6400$  km. And finally, the gravity gradient tensor  $T_{gg}$  is given by:

$$T_{gg} = \begin{pmatrix} T_{xx} & T_{xy} & T_{xz} \\ T_{xy} & T_{yy} & T_{yz} \\ T_{xz} & T_{yz} & T_{zz} \end{pmatrix}. \quad (6.17)$$

### 6.1.2 Contrast Model

With the above set of symbols, we can express the final atom interferometer phase output in hundreds of terms, which can be rearranged in a form that is easily given physical meaning of. We will discuss this in more detail in the next section 6.2. In this section, we only focus on the terms that affects interferometer contrast significantly.

The terms that could reduce interferometer contrast are those that depend on initial position  $\mathbf{r}_0$  and velocity  $\mathbf{v}_0$ , because if a particular phase term depends on these initial conditions, then the atoms with different initial condition get different phase output. In other words, those terms make the phase contribution incoherent across the atom cloud, thus reducing interferometer contrast. The leading contrast-related terms are as follows:

$$\phi_{\text{contrast-related}} = + k_{1x}(r_{ix} + v_{ix}t_0) \quad (6.18)$$

$$- 2k_{2x}(r_{ix} + v_{ix}(t_0 + T)) \quad (6.19)$$

$$+ k_{3x}(r_{ix} + v_{ix}(t_0 + 2T)) \quad (6.20)$$

$$+ k_{1z}(r_{iz} + v_{iz}t_0) \quad (6.21)$$

$$- 2k_{2z}(r_{iz} + v_{iz}(t_0 + T)) \quad (6.22)$$

$$+ k_{3z}(r_{iz} + v_{iz}(t_0 + 2T)) \quad (6.23)$$

The rule of calculating contrast has been outlined in section 3.2.2.4, and here we present the complete result with our symbol set defined in the previous section 6.1.1:

$$\begin{aligned} \chi = & \exp\left(-\frac{(\theta_{1x} - 2\theta_{2x} + \theta_{3x})^2 k_{\text{eff}}^2 r_0^2}{4}\right) \\ & \cdot \exp\left(-\frac{[t_0(\theta_{1x} - 2\theta_{2x} + \theta_{3x}) + 2T(-\theta_{2x} + \theta_{3x})]^2 k_{\text{eff}}^2 v_{\text{rms}}^2}{2}\right) \\ & \cdot \exp\left(-\frac{(\theta_{1z} - 2\theta_{2z} + \theta_{3z})^2 k_{\text{eff}}^2 r_0^2}{4}\right) \\ & \cdot \exp\left(-\frac{[t_0(\theta_{1z} - 2\theta_{2z} + \theta_{3z}) + 2T(-\theta_{2z} + \theta_{3z})]^2 k_{\text{eff}}^2 v_{\text{rms}}^2}{2}\right). \end{aligned} \quad (6.24)$$

Here  $r_0$  is the atom cloud initial 1/e-radius, and  $v_{\text{rms}}$  is the classical rms thermal velocity:

$$v_{\text{rms}} = \sqrt{\frac{k_b T_a}{m}}, \quad (6.25)$$

where  $k_b$  is the Boltzmann constant, and  $T_a$  is the classical thermal temperature of the atom cloud.

The atom cloud is detected as an assemble, with corresponding phase averaged over all the atoms in the cloud. Since the total phase of a single atom contains only linear terms of its initial position and velocity, the average phase of the atom cloud has same expression as single atom except the initial condition  $\mathbf{r}_0$  and  $\mathbf{v}_0$  are replaced by the assemble average  $\mathbf{r}_0^*$  and  $\mathbf{v}_0^*$ . In the next section 6.2, interferometer phase model uses initial conditions of  $\mathbf{r}_0^*$  and  $\mathbf{v}_0^*$ , concerning only the overall atom cloud behavior.

### 6.1.3 Platform Noise and Contrast Noise

As discussed in the last sub-section, platform angular noise introduces contrast noise which can be calculated as equation 6.24. Ellipse fitting picks up this contrast noise in the fitting process and mistakenly interprets it as ‘‘apparent’’ phase noise. The

magnitude of this effect can easily be simulated, as shown in figure 6.2. In the contrast-noise-dominated system, it is advantageous to run the interferometer near  $\phi_d = 0$  or  $\phi_d = \pi$  because in that case there are some data points at the middle of both sensors' fringes where contrast noise effect is minimum. This is clearly shown in the simulation as the impact of platform noise on ellipse fitting is much smaller when two sensors are nearly in-phase ( $\phi_d = 0.2$ ). Experimental tests qualitatively and quantitatively confirmed these simulation results.

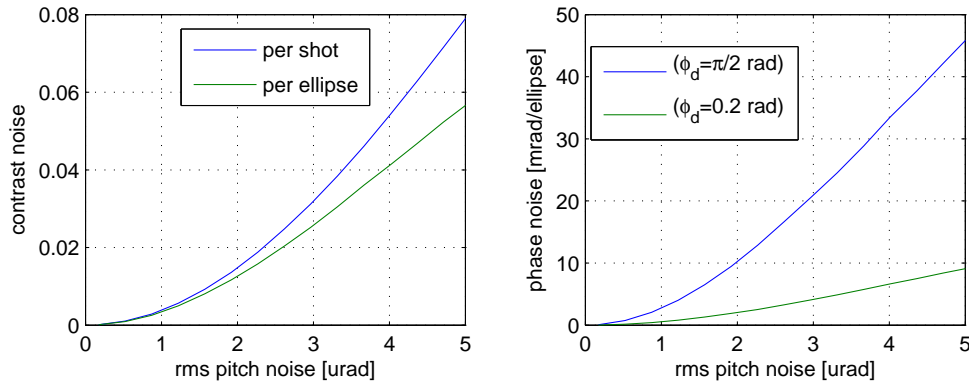


Figure 6.2: Platform noise and contrast noise: the contrast noise itself does not depend on the differential phase between sensors, but its impact on ellipse fitting is much smaller when two sensors are nearly in-phase. Pitch noise is assumed to be white (pitch angles at three pulses are reasonably independent) and is the only noise source. Other parameters:  $r_0 = 2.2$  mm,  $v_{\text{rms}} = 1.2$  cm/s,  $T = 85$  ms, and  $t_0 = 20$  ms.

#### 6.1.4 Term Evaluation

The symbolic model in the Earth frame has been solved by computer, and we numerically evaluated all terms with the following maximumly possible values:

$$T = 85 \text{ ms} \quad (6.26)$$

$$t_0 = 20 \text{ ms} \quad (6.27)$$

$$r_{ix} = 0.005 \text{ m} \quad (6.28)$$

$$r_{iy} = 1 \text{ m} \quad (6.29)$$

$$r_{iz} = 0.005 \text{ m} \quad (6.30)$$

$$v_{ix} = 0.02 \text{ m/s} \quad (6.31)$$

$$v_{iy} = 0.02 \text{ m/s} \quad (6.32)$$

$$v_{iz} = 1 \text{ m/s} \quad (6.33)$$

$$\theta_{jx} = 20 \text{ } \mu\text{rad} \quad (6.34)$$

$$\theta_{jz} = 20 \text{ } \mu\text{rad} \quad (6.35)$$

$$\omega_x = 7 \times 10^{-5} \text{ rad/s} \quad (6.36)$$

$$\omega_y = 7 \times 10^{-5} \text{ rad/s} \quad (6.37)$$

$$\omega_z = 7 \times 10^{-5} \text{ rad/s} \quad (6.38)$$

$$R = 6400 \text{ km} \quad (6.39)$$

$$g_z = -9.8 \text{ m/s} \quad (6.40)$$

$$T_{xx} = T_{yy} = -g_z/R \quad (6.41)$$

$$T_{zz} = 2g_z/R \quad (6.42)$$

Other constants can be found in appendix A. We pick out about hundred terms that are at least 0.1 mrad, and rearrange them into a physically-meaningful form. The result can be understood easily in the inertial frame, and will be discussed in section 6.2.

### 6.1.5 A Note on Numerical Calculation

The above procedure retains symbolic form until the last minute when actual numbers are plugged into individual terms. The advantage of using symbolic calculation is that it is easy to identify physically-meaningful terms and the most difficult part of the calculation, solving differential equations, does not have to be repeated for every shot in parameter optimization and fitting algorithm. However, in certain cases, solving problems completely numerically may also be required. When numerically solve the differential equation, one might run into underflow problem with double-precision numbers in computer. It is easier to see this problem if one expands the centrifugal

force term in equation 6.1:

$$[\boldsymbol{\Omega} \times (\mathbf{R} + \mathbf{r})]^2 = \boldsymbol{\Omega}^2(\mathbf{R} + \mathbf{r})^2 - [\boldsymbol{\Omega} \cdot (\mathbf{R} + \mathbf{r})]^2 \quad (6.43)$$

$$= \boldsymbol{\Omega}^2 R^2 + (\boldsymbol{\Omega} \cdot \mathbf{R})^2 \quad (6.44)$$

$$+ \boldsymbol{\Omega}^2(2\mathbf{R} \cdot \mathbf{r} + r^2) - 2(\boldsymbol{\Omega} \cdot \mathbf{R})(\boldsymbol{\Omega} \cdot \mathbf{r}) - (\boldsymbol{\Omega} \cdot \mathbf{r})^2 \quad (6.45)$$

Note that  $R \approx 6400$  km, while  $r$  is the atom position with respect to its initial position and typically on the order of 5 cm. So the term  $\boldsymbol{\Omega}^2 r^2$  is about  $10^{-16}$  smaller than  $\boldsymbol{\Omega}^2 R^2$  and standard IEEE double-precision number in computer has relative precision of  $10^{-16}$  so the term  $\boldsymbol{\Omega}^2 r^2$  is easily ignored during numerical computation yet all the important gravity terms are in the variable  $r$ . Nevertheless, the terms in the line of 6.44 are the same for two sensors and will be eliminated when differential measurement are made between sensors. Without these terms,  $\boldsymbol{\Omega}^2 r^2$  is only  $10^{-8}$  smaller than other primary terms in the equation and can be retained during computation. Therefore, the numerical evaluation is carried out by essentially throwing away the constant terms in the line of 6.44 and it becomes a valuable tool to verify our symbolic model, which is more computationally intensive.

## 6.2 Analysis in the Inertial Frame

In this section, we analyze atom interferometer in the inertial frame. We first define effective local gravity according to equation 6.2:

$$\mathbf{g}^i = \mathbf{g} - \boldsymbol{\Omega} \times (\boldsymbol{\Omega} \times \mathbf{R}), \quad (6.46)$$

(The superscript  $i$  denotes inertial frame) or:

$$\begin{cases} g_x^i &= -\omega_x \omega_z R \\ g_y^i &= -\omega_y \omega_z R \\ g_z^i &= g_z + \omega_x^2 R + \omega_y^2 R \end{cases} \quad (6.47)$$

So the atom moves according to

$$\begin{cases} r_x^i(t) &= r_{ix}^* + v_{ix}^* t + g_x^i t^2 \\ r_z^i(t) &= r_{iz}^* + v_{iz}^* t + g_z^i t^2 \end{cases} \quad (6.48)$$

The  $\mathbf{k}_{\text{eff}}$  is defined with respect to the Earth frame for every Raman pulse according to equation 6.10:

$$\mathbf{k}(t) = (k_x(t), k_{\text{eff}} + k_y(t), k_z(t)), \quad (6.49)$$

where pulse number  $j$  is replaced by time  $t$ .  $\mathbf{k}_{\text{eff}}$  in the inertial frame is given by

$$\mathbf{k}^i(t) = \mathbf{k}(t) + (\boldsymbol{\Omega} t) \times \mathbf{k}(t), \quad (6.50)$$

or:

$$\begin{cases} k_x^i(t) &= k_x(t) - k_{\text{eff}} \omega_z t + k_z(t) \omega_y t \\ k_z^i(t) &= k_z(t) + k_{\text{eff}} \omega_x t - k_x(t) \omega_y t \end{cases} \quad (6.51)$$

where smaller terms are ignored. With inertial frame representation of  $\mathbf{k}^i(t)$ ,  $\mathbf{r}^i(t)$ , and  $\mathbf{g}^i$ , the interferometer phase can be written as:

$$\phi^i = + k_x^i(t_0) r_x^i(t_0) - 2k_x^i(t_0 + T) r_x^i(t_0 + T) + k_x^i(t_0 + 2T) r_x^i(t_0 + 2T) \quad (6.52)$$

$$+ k_z^i(t_0) r_z^i(t_0) - 2k_z^i(t_0 + T) r_z^i(t_0 + T) + k_z^i(t_0 + 2T) r_z^i(t_0 + 2T) \quad (6.53)$$

$$+ (k_y(t_0) - 2k_y(t_0 + T) + k_y(t_0 + 2T)) r_{iy}^* \quad (6.54)$$

$$+ k_{\text{eff}} (g_y^i + T_{yy} (r_{iy}^* + v_{iy}^* (t_0 + T))) T^2 \quad (6.55)$$

$$+ k_{\text{eff}} (\omega_x^2 + \omega_z^2) r_{iy}^* T^2 \quad (6.56)$$

$$+ \frac{1}{6} k_{\text{eff}} (-g_z^i \omega_x + g_x^i \omega_z) [t_0^3 - 2(t_0 + T)^3 + (t_0 + 2T)^3]. \quad (6.57)$$

This result is explained line by line as following. Line 6.52, 6.54, and 6.53 are laser phase along  $x$ ,  $y$ , and  $z$  axis, respectively. Terms in line 6.54 are very small since  $k_y(t)$  is second-order sensitive to angular jitter, so only  $r_{iy}^*$  ( $\sim 1$  m) is considered here, while motions along Raman axis are ignored ( $v_{iy}^* T \sim 1$  mm).

Line 6.55 is acceleration contribution along Raman axis. Since effective acceleration  $g_y^i$  is defined at the origin of the Earth frame (or the midpoint between two

sensors), the average acceleration the atom cloud senses is  $(g_y^i + T_{yy}(r_{iy}^* + v_{iy}^*(t_0 + T)))$  with extra  $T_{yy}$  term added where the average position of the atom during the interferometer sequence is used.

Line 6.56 gives the apparent gravity gradient terms.  $[(\omega_x^2 + \omega_z^2)r_{iy}^*]$  is the effective centrifugal force around the center of two sensors, and this becomes an effective acceleration the atom interferometer sequence senses.

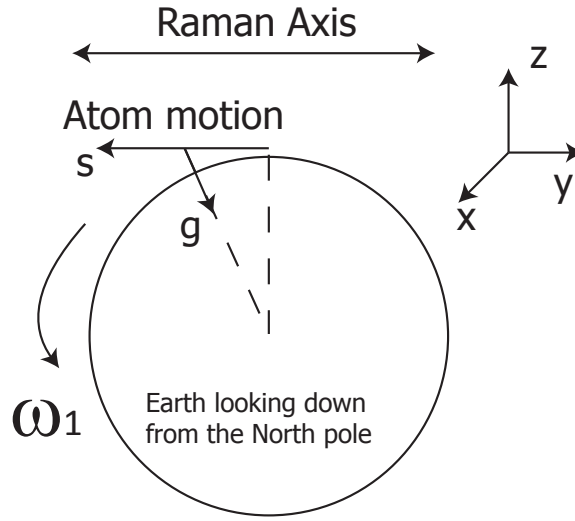


Figure 6.3: Extra phase shift due to earth rotation.

Line 6.57 is an even smaller yet very interesting effect. We consider a simple case to explain this effect: suppose the apparatus is on the equator, and Raman axis is east-west as shown in figure 6.3. In this case  $\omega_y = \omega_z = 0$ , and  $\omega_x = \Omega$  (Earth rotation rate). In the view of inertial frame, atom gets an extra initial velocity along  $y$ -axis during launching due to earth rotation, and to the first order, the extra motion along  $y$ -axis is:

$$s(t) = -\omega_x R t. \quad (6.58)$$

After time  $t$ , the local gravity  $\mathbf{g}$  has projection along Raman axis, so the atom gets extra acceleration of

$$a_{\text{extra}}(t) = g s(t)/R = -\omega_x t g. \quad (6.59)$$

This extra acceleration is in addition to the existing motion and produces extra motion along Raman axis:

$$y_{\text{extra}} = -\frac{1}{6}\omega_x g_z^i t^3, \quad (6.60)$$

and to the first order,  $k_{\text{eff}} \cdot y_{\text{extra}}$  gives extra laser phase shown as one term in line 6.57. In general  $\omega_z \neq 0$ , and one can derive both terms in that line.

The result presented here is only an approximation. However we compared our result with symbolic model using maximumly possible values discussed in section 6.1.4, and proved that our inertial frame model matches the Earth frame model within 0.1 mrad, thus practically the same.

This model calculates single sensor phase output. For dual sensor differential measurement, such as gravity gradient measurement, simply the difference between two such expressions with different initial conditions are used. More precisely, one sensor has  $r_{0y} = -L/2$  while the other has  $r_{0y} = L/2$ , where  $L$  is the measurement baseline. In fact many terms in  $\phi^i$  are common between two sensors and are thus eliminated in differential measurements. This will be discussed in more detail in section 6.5.

## 6.3 Imperfection of Raman Windows

Ideally, there is only vacuum between two atom clouds in two atomic sensors; in reality, our sensors are separated by about one meter and there are two Raman windows between them. Due to manufacture imperfections, these two windows have wedge on the order of few hundred microradians, and they attenuate the Raman beam by about 7% total. Various effects are arised from this Raman window imperfection.

### 6.3.1 Wedge

In our apparatus, Raman window wedge is not along any particular axis, thus can be split into vertical wedge  $\beta_v$  and horizontal wedge  $\beta_h$  components. Vertical wedge contributes the majority of the differential phase we observe between two sensors. Figure 6.4 shows the quadratic dependence of differential phase as a function of the

interrogation time  $T$ :

$$\phi = \mathbf{k}_{\text{eff}} \cdot \mathbf{g}T^2 = k_{\text{eff}} g \beta_v T^2, \quad (6.61)$$

where  $g$  is the local gravity and  $T$  is the interrogation time. This differential phase is arised from the fact that local gravity  $\mathbf{g}$  projects different amount onto Raman axis ( $\mathbf{k}_{\text{eff}}$ ) in two sensors. We usually refer this effect as “little-g projection”.

Note here the wedge angle  $\beta_v$  refers to the beam steering angle in the vertical direction, and  $\beta_v = (n - 1)\alpha_v$  where  $n$  is the index of refraction of the window glass and  $\alpha_v$  is the actual vertical wedge angle between two glass surfaces. In this thesis, wedge angle  $\beta$  always refers to the beam steering angle unless otherwise explicitly specified.

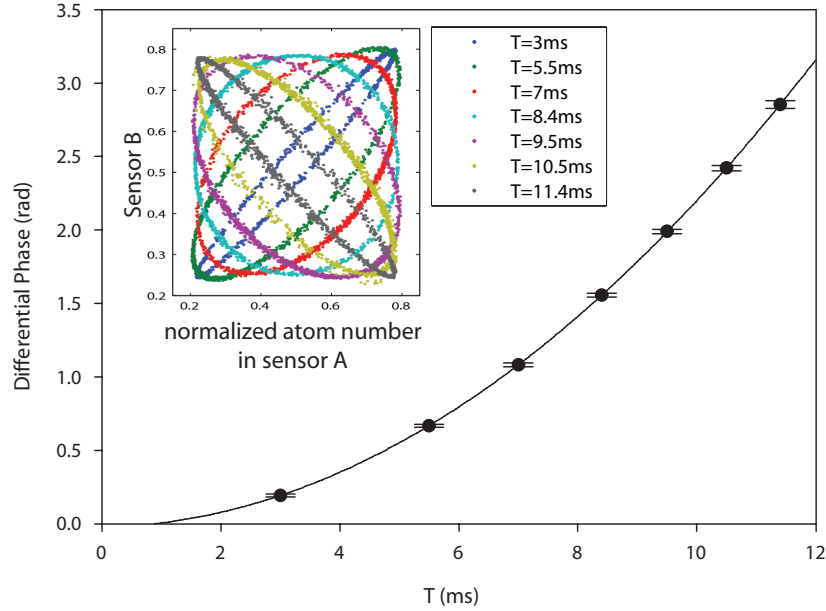


Figure 6.4: Short- $T$  phase v.s.  $T$ : this shows a very good quadratic dependence of phase as a function of the interrogation time  $T$ . The inferred vertical wedge is about  $150 \mu\text{rad}$ . The inset figure shows all the data points that are used to extract differential phase for various  $T$  using ellipse fitting.

The horizontal wedge component  $\beta_h$  does not introduce differential phase when the platform is perfectly levelled. However, when the platform rolls (rotates around

Raman axis),  $\beta_h$  starts to contribute little-g projection:

$$\phi(\theta_y) = k_{\text{eff}} g \beta_h \theta_y T^2 + k_{\text{eff}} g \beta_v (1 - \theta_y^2/2) T^2, \quad (6.62)$$

where  $\theta_y$  is the roll angle. This effect is usually referred as “roll sensitivity”. Differential phase is first order sensitive to horizontal wedge  $\beta_h$ , but is second order sensitive to vertical wedge  $\beta_v$ . The second order term is usually ignored.

Figure 6.5 shows experimental data in our particular apparatus. The inferred horizontal wedge is  $120 \mu\text{rad}$ . This roll sensitivity was reduced by a factor of 10 with a carefully adjusted corrective wedge, thus is not a limiting factor in our gravity gradient survey tests.

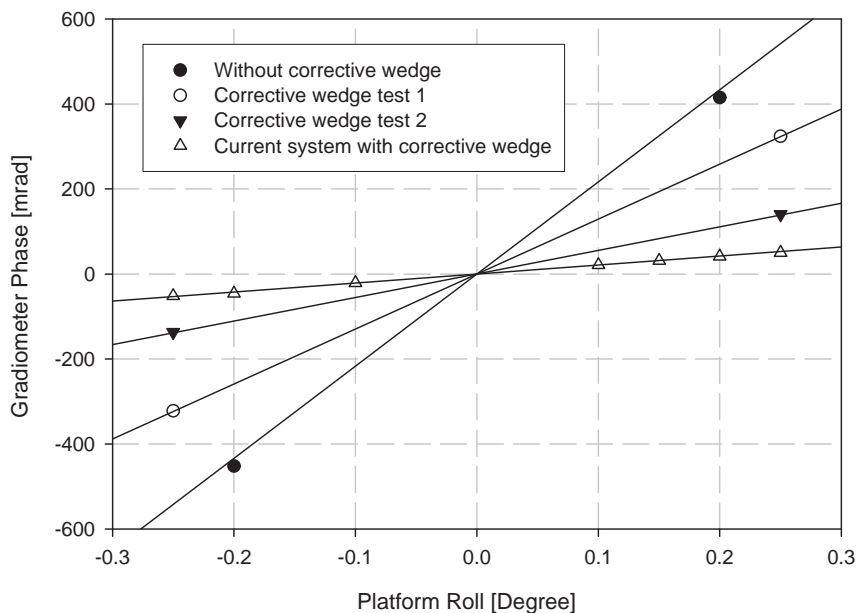


Figure 6.5: Roll sensitivity: various tests are shown, and interrogation  $T$  is always 85 sec in these tests. Roll sensitivity without corrective wedge is about 125 rad/rad. This sensitivity was reduced by a factor of 10 with a carefully adjusted corrective wedge.

Above results concern only the static case. In dynamic case when the platform moves during interferometer sequence, wedge has to be considered in the dynamic

error model which will be discussed in detail in section 6.4.

### 6.3.2 Window Attenuation

In our apparatus, the two Raman windows between atomic clouds attenuate the Raman beam by  $1 - \eta = 7\%$  total, so two sensors receive different Raman beam intensities. This attenuation does not impose a limit on the interferometer performance, but does give some interesting effects in the system.

We observe  $\approx 10$  mrad differential phase shift between sensors when the second pulse length  $t_\mu$  is changed by 5%. The phase shift is primarily from the differential ac Stark effect. From section B.1 we know single sensor gets about  $\pi$  rad ac Stark phase shift per beam during a  $\pi$ -pulse (length  $t_{\mu 0}$ ):

$$\phi_3^{\text{AC}} = \alpha_3 I_3 t_{\mu 0} \approx \pi, \quad (6.63)$$

$$\phi_4^{\text{AC}} = \alpha_4 I_4 t_{\mu 0} \approx \pi, \quad (6.64)$$

when the differential ac Stark is canceled:

$$\alpha_3 I_3 = \alpha_4 I_4, \quad (6.65)$$

thus the differential ac Stark phase shift for single sensor is 0:

$$\phi^{\text{AC}} = \phi_3^{\text{AC}} - \phi_4^{\text{AC}} = 0. \quad (6.66)$$

However, due to window attenuation, this differential ac Stark can never be canceled simultaneously for both sensors (at least in the current Raman beam scheme), so the difference in differential ac Stark phase between two sensors is  $t_\mu$  dependent:

$$\Delta\phi^{\text{AC}} = (\alpha_3 \eta I_3 t_\mu - \alpha_4 I_4 t_\mu) - (\alpha_3 I_3 t_\mu - \alpha_4 \eta I_4 t_\mu) \quad (6.67)$$

$$= (1 - \eta)\alpha_4 I_4 t_\mu - (1 - \eta)\alpha_3 I_3 t_\mu \quad (6.68)$$

$$\approx (1 - \eta)\pi(t_\mu/t_{\mu 0}). \quad (6.69)$$

This explains the phase sensitivity to pulse length. Similar calculation can also explain phase shift when Raman beam intensity is changed or Raman single-photon detuning is changed. In particular, phase sensitivity to Raman single-photon detuning is about 0.07 mrad/MHz.

## 6.4 Wedge Noise Model

When wedge is inserted into the system, correcting terms need to be added to the error model. This mainly includes the optical path length change between the reference point and the sensor, or simply between two sensors. We start with an elementary model.

### 6.4.1 Two-Dimensional Wedge

Figure 6.6 shows a single two-dimensional wedge case and straightforward calculation gives the optical path length between sensor 1 (atom cloud at  $S_1$ ) and sensor 2 ( $S_2$ ):

$$S_{1 \rightarrow 2} = \overline{AB} + n \overline{BC} + \overline{CD} \quad (6.70)$$

$$\approx [l_1 + l_2(1 - \beta^2/2) + \beta(u - h)] - (\beta l_2 + h)\theta - \frac{1}{2}(l_1 + l_2)\theta^2, \quad (6.71)$$

where  $n$  is the index of refraction and  $\beta = (n - 1)(\alpha_1 + \alpha_2)$  is the wedge beam steering angle, the same convention as in the section 6.3.1. One might expect  $l_1$  and  $l_2$  to be symmetric in equation 6.71 but they are not. This is because we define angle  $\theta$  at point  $S_1$ . One can calculate optical path length from  $S_2$  to  $S_1$  by defining a beam angle  $\theta'$  at  $S_2$ , and get:

$$S_{2 \rightarrow 1} \approx [l_2 + l_1(1 - \beta^2/2) + \beta(u)] - (\beta l_1 - h)\theta' - \frac{1}{2}(l_1 + l_2)\theta'^2. \quad (6.72)$$

Using  $\theta' = -\theta - \beta$ , one can prove  $S_{1 \rightarrow 2} = S_{2 \rightarrow 1}$ . Note that during the calculation, retaining second-order terms in  $\cos()$  is essential because that could contain first-order terms of  $\theta$ .

Figure 6.7 adds a second wedge between sensors. One can still calculate optical



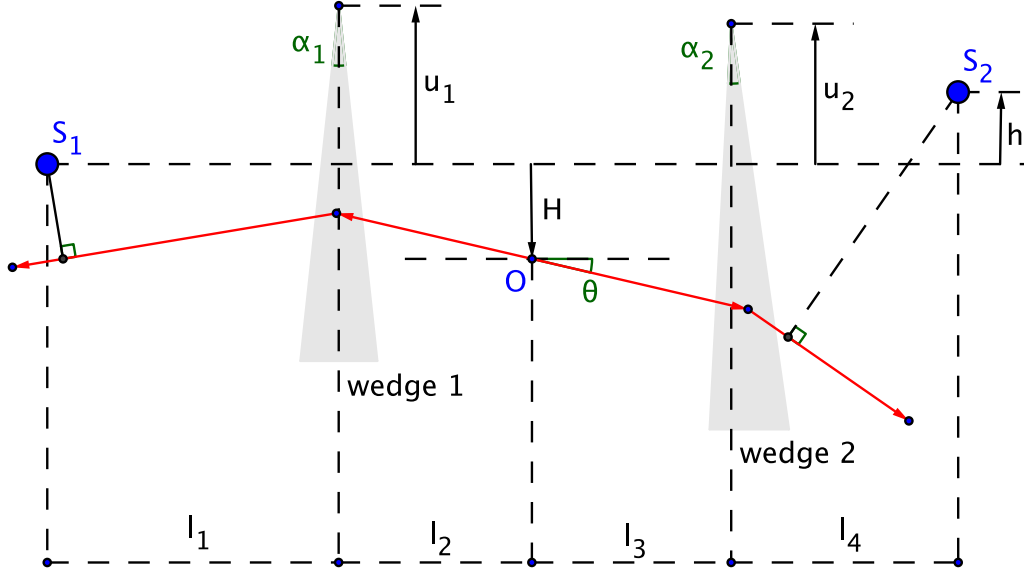


Figure 6.7: Diagram of dual 2D wedge.

path length between sensors as following:

$$\begin{aligned}
 S_{2D0} = & (l_3 + l_4) \left( 1 - \frac{(\theta + \beta_2)^2}{2} \right) - (h + H)(\theta + \beta_2) \\
 & + (l_1 + l_2) \left( 1 - \frac{(-\theta + \beta_1)^2}{2} \right) - (H)(-\theta + \beta_1). \quad (6.74)
 \end{aligned}$$

The correcting terms for this two-dimensional case are:

$$C_{2D} = S_{2D} - S_{2D0} = H(\beta_1 + \beta_2) + \beta_1 u_1 + \beta_2 u_2 + (l_3 \beta_2 - l_2 \beta_1) \theta. \quad (6.75)$$

Note that large part of this correction, especially the first term, is relatively stable. We are more interested in using this wedge model to decorrelate platform motion, which introduces  $\Delta u_1$ ,  $\Delta u_2$ , and  $\Delta \theta$ . The jitter terms to put into the error model are then:

$$\Delta C_{2D} = \beta_1 \Delta u_1 + \beta_2 \Delta u_2 + (l_3 \beta_2 - l_2 \beta_1) \Delta \theta. \quad (6.76)$$

It is important to note that jitter in atom cloud position (i.e.  $\Delta h$ ) does not show

up in  $C_{2D}$  or  $\Delta C_{2D}$ , because it was already fully included in the error model.

### 6.4.2 Three-Dimensional Wedge

Three-dimensional wedge, as in our apparatus, is not simply a linear summation of vertical wedge and horizontal wedge effects. The coupling between these two complicates the analysis. Figure 6.8 shows the coordinate system for our calculation, which is carried out mostly by algebra instead of relying on the visual analysis as in the two-dimensional case.

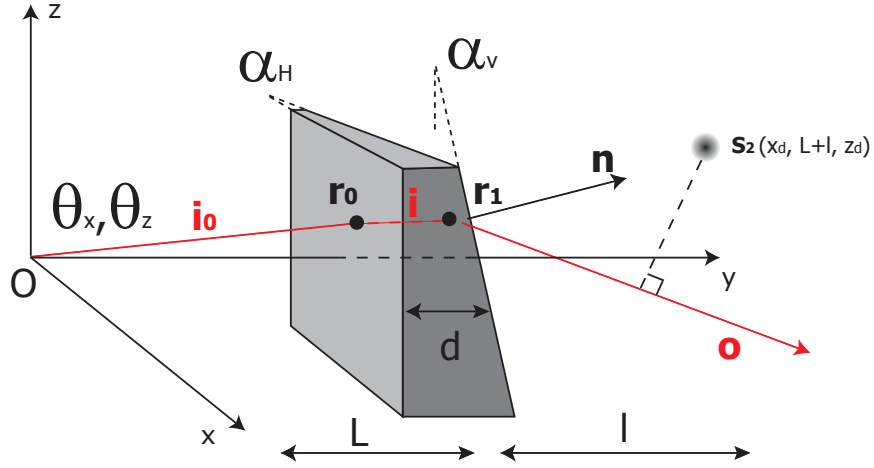


Figure 6.8: 3D single wedge coordinate system for calculation.

Reference point  $O$  is at the origin, and sensor is at  $\mathbf{S}_2 = (x_d, L + l, z_d)$ . Suppose the beam steers by  $\theta_x$  and  $\theta_z$  around  $x$ -axis and  $z$ -axis, respectively. The Raman beam (unit) vector off  $O$  is:

$$\mathbf{i}_0 = \left( -\theta_z, 1 - \frac{\theta_x^2}{2} - \frac{\theta_z^2}{2}, \theta_x \right). \quad (6.77)$$

Without losing generality, we assume the first surface of the wedge is on the plane of  $y = L$ . The Raman beam intersects with this surface at  $\mathbf{r}_0 = (-L\theta_z, L, L\theta_x)$ . The

(unit) beam vector inside the wedge is therefore:

$$\mathbf{i} = \left( -\frac{\theta_z}{n}, 1 - \frac{\theta_x^2}{2n^2} - \frac{\theta_z^2}{2n^2}, \frac{\theta_x}{n} \right), \quad (6.78)$$

where  $n$  is the refractive index of the wedge.

Suppose the wedge angles are  $\alpha_h$  and  $\alpha_v$  in the horizontal and vertical direction, respectively. And as usual, the beam steering angles are denoted as  $\beta_h = (n - 1)\alpha_h$ , and  $\beta_v = (n - 1)\alpha_v$ . Suppose the wedge rotates  $\theta_y$  around  $y$ -axis, then the normal vector of the second surface of the wedge is

$$\mathbf{n} = \left( \alpha_h \cos(\theta_y) + \alpha_v \cos(\theta_y), 1 - \frac{\alpha_h^2}{2} - \frac{\alpha_v^2}{2}, \alpha_v \cos(\theta_y) - \alpha_h \cos(\theta_y) \right). \quad (6.79)$$

Suppose the second surface of the wedge passes through point  $\mathbf{P} = (u_x, L + d, u_z)$ . Here  $d$  denotes the wedge thickness where the Raman beam normally passes through, while  $u_x$  and  $u_z$  represent wedge motion along horizontal and vertical directions, respectively. In this representation, the second surface of the wedge can be expressed as  $(\mathbf{r} - \mathbf{P}) \cdot \mathbf{n} = 0$ , and with the incident beam in the wedge:

$$\frac{x - (-L\theta_z)}{i_x} = \frac{y - L}{i_y} = \frac{z - L\theta_x}{i_z}, \quad (6.80)$$

we can solve the incident point  $\mathbf{r}_1 = (x_1, y_1, z_1)$  on the second surface of the wedge.

With a little vector algebra, we can calculate the outgoing beam (unit) vector off the wedge:

$$\mathbf{o} = n\mathbf{i} + \left( -n(\mathbf{i} \cdot \mathbf{n}) + \sqrt{n^2(\mathbf{i} \cdot \mathbf{n})^2 - n^2 + 1} \right) \mathbf{n}. \quad (6.81)$$

One can verify that to the first order:

$$o_x = -\theta_z - \beta_h - \beta_v \theta_y \quad (6.82)$$

$$o_z = \theta_x - \beta_v + \beta_h \theta_y, \quad (6.83)$$

as expected. The total optical path length can then be calculated as the sum of

segments:

$$S_{3D} = L|\mathbf{r}_0| + n|\mathbf{r}_1 - \mathbf{r}_0| + \mathbf{o} \cdot (\mathbf{S}_2 - \mathbf{r}_1). \quad (6.84)$$

With all second-order terms retained:

$$\begin{aligned} S_{3D} &= l \left( 1 - \frac{\beta_h^2}{2} - \frac{\beta_v^2}{2} \right) + L + d \left( n - 1 + \frac{\beta_h^2}{2} + \frac{\beta_v^2}{2} \right) \\ &\quad + \beta_h(u_x - u_z\theta_y - x_d + z_d\theta_y) \\ &\quad + \beta_v(u_z + u_x\theta_y - x_d\theta_y - z_d) \\ &\quad + [z_d + (l - d)\beta_v]\theta_x + [-x_d - (l - d)\beta_h]\theta_z \\ &\quad + \left[ -\frac{L + l}{2} + \left( \frac{n - 1}{n} \right) \frac{d}{2} \right] (\theta_x^2 + \theta_z^2). \end{aligned} \quad (6.85)$$

Similar to the two-dimensional case, the optical path length in no-wedge case is

$$\begin{aligned} S_{3D0} &= \mathbf{o} \cdot \mathbf{S}_2 \quad (6.86) \\ &= (L + l) \left( 1 - \frac{\beta_h^2}{2} - \frac{\beta_v^2}{2} \right) \\ &\quad - \beta_h x_d - \beta_v x_d \theta_y - \beta_v z_d + \beta_h z_d \theta_y \\ &\quad + [z_d + (L + l)\beta_v]\theta_x + [-x_d - (L + l)\beta_h]\theta_z \\ &\quad - \frac{L + l}{2} (\theta_x^2 + \theta_z^2). \end{aligned} \quad (6.87)$$

The correcting terms are:

$$\begin{aligned} C_{3D} &= S_{3D} - S_{3D0} \quad (6.88) \\ &= d \left( n - 1 + \frac{\beta_h^2}{2} + \frac{\beta_v^2}{2} \right) + L \left( \frac{\beta_h^2}{2} + \frac{\beta_v^2}{2} \right) \\ &\quad + \beta_h(u_x - u_z\theta_y) + \beta_v(u_z - u_x\theta_y) \\ &\quad + (-d - L)\beta_v\theta_x + (d + L)\beta_h\theta_z \\ &\quad + \left( \frac{n - 1}{n} \right) \frac{d}{2} (\theta_x^2 + \theta_z^2). \end{aligned} \quad (6.89)$$

Note atom cloud position jitter  $x_d$  and  $z_d$  are already fully included in the error model  $S_{3D0}$  thus do not appear in  $C_{3D}$ . Like in the two-dimensional case, we are only

interested in the jitter terms  $\Delta\theta_x$ ,  $\Delta\theta_z$ ,  $\Delta u_x$ , and  $\Delta u_z$ . And since in our apparatus  $d \approx 1$  cm, much smaller than  $L \sim 1$  m, we can safely ignore the last line in the above equation. As a result, the jitter terms to put into the error model are:

$$\Delta C_{3D} = \beta_h(\Delta u_x - \Delta u_z \theta_y) + \beta_v(\Delta u_z - \Delta u_x \theta_y) + (L + d)(\beta_h \Delta \theta_z - \beta_v \Delta \theta_x) \quad (6.90)$$

To estimate the order of magnitude of this correction, we consider a special case: suppose the platform rotation center is right below the reference point at the gimbal  $\mathbf{r}_c = (0, 0, -H)$  where  $H$  is the platform height. If the platform has a rotation of  $(\theta_x, \theta_y, \theta_z)$ , the wedge position is then:

$$\begin{pmatrix} u_x \\ \cdot \\ u_z \end{pmatrix} \equiv \mathbf{w} = \begin{pmatrix} \theta_x \\ \theta_y \\ \theta_z \end{pmatrix} \times \begin{pmatrix} 0 \\ L \\ +H \end{pmatrix} = \begin{pmatrix} H\theta_y - L\theta_z \\ \cdot \\ L\theta_x \end{pmatrix} \quad (6.91)$$

Plug  $u_x$  and  $u_z$  into equation 6.90, we get:

$$\Delta C_{3D} = \beta_h H \theta_y + d(\beta_h \theta_z - \beta_v \theta_x), \quad (6.92)$$

in which smaller terms are ignored. Since  $d \ll H$ , this can be further reduced to

$$\Delta C_{3D} = \beta_h H \theta_y \quad (6.93)$$

This result apparently agrees with intuition. In our apparatus,  $\beta_h \sim 100 \mu\text{rad}$ ,  $H \sim 1$  m, and  $\theta_y \sim 1 \mu\text{rad}$ , phase correction due to wedge ( $k_{\text{eff}} \cdot \Delta C_{3D}$ ) is at least a few mrad, big enough to be included in the model.

## 6.5 Gradiometer Error Terms

In section 6.2, we calculated single sensor phase output. For dual sensor differential measurement, such as gravity gradient measurement, we simply take the difference between two such expressions with different initial conditions. More precisely, one sensor has  $r_{0y} = -L/2$  while the other has  $r_{0y} = L/2$ , where  $L$  is the baseline. In

addition, two sensors may have other different parameters. We now make an effort to look at all the error terms in detail. First we consider a relatively ideal condition, and then add in stable apparatus errors that do not change shot-to-shot (e.g., Raman misalignment), and finally consider jitter terms that is caused by platform motion which is not repeatable shot-to-shot.

Similar analysis can be found in [74] section 3.3, [70], and [82].

### 6.5.1 Ideal Condition

We start with a relatively ideal condition. Atoms are perfectly aligned with Raman beams, and their initial velocities are perfectly vertical ( $v_{iz}^* = v_L = 1$  m/s for evaluation). The only non-ideal element we add in here is that the Raman windows between sensors have a total wedge of  $\beta_h$  and  $\beta_v$  (horizontally and vertically, assumed to be both 200  $\mu$ rad in term evaluation). Other symbols use values in section 6.1.4. Table 6.1 shows terms in this ideal case with explanations.

Term	Value [rad]	Notes
$k_{\text{eff}}g_z\beta_vT^2$	$2.04 \times 10^2$	Little-g projection (eq. 6.61)
$-k_{\text{eff}}\beta_hR\omega_y\omega_zT^2$	$7.47 \times 10^{-1}$	Apparent gg (see $g_y^i$ in eq. 6.47)
$k_{\text{eff}}\omega_x^2R\beta_vT^2$	$7.47 \times 10^{-1}$	Little-g projection (see $g_z^i$ in eq. 6.47)
$k_{\text{eff}}\omega_y^2R\beta_vT^2$	$7.47 \times 10^{-1}$	Little-g projection (see $g_z^i$ in eq. 6.47)
$k_{\text{eff}}T_{yy}T^2L$	$1.52 \times 10^{-1}$	Gravity gradient (!)
$-3k_{\text{eff}}\omega_yg_z\beta_hT^3$	$3.75 \times 10^{-3}$	Gyro
$-2k_{\text{eff}}\omega_y\beta_hv_LT^2$	$3.04 \times 10^{-3}$	Gyro

Table 6.1: Gradiometer phase in ideal condition: all terms above 1 mrad are shown, and values are shown in absolute number.

Note that although some of the wedge-induced terms are pretty large, they are stable. Therefore the gravity gradient induced phase shift is the dominant phase shift when the apparatus is translated to a location with a different  $T_{yy}$ . Note that if the apparatus rotates, Earth rotation components  $\omega_i$  could change, and wedge-induced phase shift would show up.

### 6.5.2 Stable Condition

Now we add Raman beam misalignment and initial velocity mismatch between sensors, but we still assume the platform is stable. There are two ways to introduce Raman beam misalignment. One could assume initial position of the second sensor is not at the ideal location  $(0, L/2, 0)$ ; or one could assume the stable Raman beam wavevector is not  $(0, k_{\text{eff}}, 0)$ , or neither. For simplicity, we assume Raman beam wavevector is ideal  $(0, k_{\text{eff}}, 0)$  in the first sensor. We introduce some new symbols in table 6.2.

	<b>Sensor 1</b>	<b>Sensor 2</b>
Initial position $\mathbf{r}_0^*$	$(0, -L/2, 0)$	$(x_h, L/2, x_v)$
Initial velocity $\mathbf{v}_0^*$	$(v_{h0}, v_{b0}, v_L + v_{v0})$	$(v_{h0} + v_h, v_{b0} + v_b, v_L + v_{v0} + v_v)$
Bottom Raman beam $\mathbf{k}_1, \mathbf{k}_3$	$(0, k_{\text{eff}}, 0)$	$(k_{\text{eff}} \beta_h, *, k_{\text{eff}} \beta_v)$
Top Raman beam $\mathbf{k}_2$	$(k_{\text{eff}} \gamma_h, *, k_{\text{eff}} \gamma_v)$	$(k_{\text{eff}} (\beta_h + \gamma_h), *, k_{\text{eff}} (\beta_v + \gamma_v))$

Table 6.2: Symbols for stable gradiometer.

Here  $x_h$  and  $x_v$  represent Raman beam misalignments (1 mm for evaluation),  $v_h$  and  $v_v$  represent transverse initial velocity mismatch between sensors (5 mm/s), and  $\beta_h$  and  $\beta_v$  are the wedge between sensors, as mentioned in the last section. Component labelled \* can be derived from the other two components.  $v_b$  is the longitudinal initial velocity mismatch (1 cm/s, see section 8.3).  $\gamma_h$  and  $\gamma_v$  represent horizontal and vertical misalignments between top and bottom Raman beams, and are typically on the order of 1  $\mu\text{rad}$  (see section 8.5.2). Note that  $\gamma_h$  and  $\gamma_v$  are generally not the same in two sensors, but are assumed to be the same in this section for simplicity (more detailed model calculation shows that even if they differ by about 1  $\mu\text{rad}$ , it does not introduce terms that are important for motion decorrelation in our experiment). The gradiometer phase terms in this stable condition can be found in table 6.3 except those already appeared in table 6.1 (in ideal condition).

Note that  $v_{b0}$ ,  $v_{h0}$  and  $v_{v0}$  terms are very small ( $\sim 10^{-5}$  rad at most), and only initial velocity mismatches  $v_h$  and  $v_v$  really matter in the error terms. The extra term

Term	Value [rad]	Notes
$-2k_{\text{eff}}\omega_z v_h T^2$	$7.60 \times 10^{-2}$	Gyro
$2k_{\text{eff}}\omega_x v_v T^2$	$7.60 \times 10^{-2}$	
$-2k_{\text{eff}}x_h \gamma_h$	$2.95 \times 10^{-2}$	Lever arm
$-2k_{\text{eff}}x_v \gamma_v$	$2.95 \times 10^{-2}$	
$-2k_{\text{eff}}v_h T \gamma_h$	$1.24 \times 10^{-2}$	
$-2k_{\text{eff}}v_v T \gamma_v$	$1.24 \times 10^{-2}$	
$k_{\text{eff}}\beta_v \gamma_v L$	$2.95 \times 10^{-3}$	
$k_{\text{eff}}\beta_h \gamma_h L$	$2.95 \times 10^{-3}$	
$-2k_{\text{eff}}\gamma_h v_h t_0$	$2.95 \times 10^{-3}$	
$-2k_{\text{eff}}\gamma_v v_v t_0$	$2.95 \times 10^{-3}$	

Table 6.3: Gradiometer phase in stable condition: all terms above 1 mrad are shown, and values are shown in absolute number.

due to baseline change during interferometer sequence (because of  $v_b$ ) is  $k_{\text{eff}}T_{yy}v_b T^3$ , which is on the order of 0.1 mrad, and can be ignored in practical analysis. It is also interesting to note that the terms in the two transverse directions (subscript h and v) are symmetric. In the next section where platform jitter terms are added in, we will assume that the jitter is only in yaw, but not in pitch. Corresponding terms in pitch can be easily derived from yaw terms.

### 6.5.3 Jitter Terms

	Sensor 1	Sensor 2
Initial position jitter $\delta \mathbf{r}_0^*$	$(x_{h0}^j, 0, 0)$	$(x_{h0}^j + x_h^j, 0, 0)$
Initial velocity jitter $\delta \mathbf{v}_0^*$	$(v_{h0}^j, 0, 0)$	$(v_{h0}^j + v_h^j, 0, 0)$
1st Raman pulse $\delta \mathbf{k}_1$	$(k_{\text{eff}}\theta_{1z}^j, 0, 0)$	$(k_{\text{eff}}\theta_{1z}^j, 0, 0)$
2nd Raman pulse $\delta \mathbf{k}_2$	$(k_{\text{eff}}\theta_{2z}^j, 0, 0)$	$(k_{\text{eff}}\theta_{2z}^j, 0, 0)$
3rd Raman pulse $\delta \mathbf{k}_3$	$(k_{\text{eff}}\theta_{3z}^j, 0, 0)$	$(k_{\text{eff}}\theta_{3z}^j, 0, 0)$

Table 6.4: Symbols for jitter gradiometer. Noise is added only to yaw for simplicity.

Platform jitter noise is added to yaw as shown in the table 6.4. Superscript  $j$  is used to denote jitter terms.  $x_h^j$  and  $v_h^j$  represent initial position and velocity jitter difference between two sensors (analysis shows that terms related to  $x_{h0}^j$  and  $v_{h0}^j$  are very small), and  $\theta_{1z}^j$ ,  $\theta_{2z}^j$ , and  $\theta_{3z}^j$  represent platform angle at three pulses. We use  $x_h^j = 1$  mm,  $v_h^j = 0.1$  mm/s, and  $\theta_{.z}^j = 10$   $\mu$ rad for term evaluation.

The primary jitter terms are not difficult to write down (see section 6.2):

$$\begin{aligned} \phi = & k_{\text{eff}}(\theta_{1z}^j - 2\theta_{2z}^j + \theta_{3z}^j)(x_h + x_h^j) \\ & + k_{\text{eff}}[(\theta_{1z}^j - 2\theta_{2z}^j + \theta_{3z}^j)t_0 + 2(\theta_{3z}^j - \theta_{2z}^j)T](v_h + v_h^j). \end{aligned} \quad (6.94)$$

Besides these terms, there are some other extra jitter terms on the order of mrad or higher, shown in table 6.5.

Term	Value [rad]	Notes
$k_{\text{eff}}\beta_h H(\theta_{1y}^j - 2\theta_{2y}^j + \theta_{3y}^j)$	$\sim 6 \times 10^{-2}$	Wedge correction (eq. 6.93)
$-k_{\text{eff}}L\beta_h(\theta_{1z}^j - 2\theta_{2z}^j + \theta_{3z}^j)/2$	$\sim 3 \times 10^{-2}$	Lever arm
$-2k_{\text{eff}}\gamma_h x_h^j$	$2.95 \times 10^{-2}$	Lever arm
$-k_{\text{eff}}L((\theta_{1z}^j)^2 - 2(\theta_{2z}^j)^2 + (\theta_{3z}^j)^2)/2$	$\sim 2 \times 10^{-3}$	Lever arm
$-2k_{\text{eff}}\omega_z v_h^j T^2$	$1.52 \times 10^{-3}$	Gyro

Table 6.5: Extra gradiometer phase in jitter condition: all terms above 1 mrad are shown except those already in equation 6.94, and values are shown in absolute number.

Since the wedge correction term and some lever arm terms are pretty big, jitter terms in equation 6.94 are not sufficient for platform noise decorrelations in practice. Also, the wedge correction term shown here only represents a special case, and in general the platform rotation center can be anywhere when our truck freely rolls on the road. Equation 6.90 should be used for wedge error correction, and that may require independent linear motion or rotation center detections on the platform.

# Chapter 7

## Various Noise and Effects Study

Every precision measurement is accompanied by a variety of noise sources, and our gravity gradient measurement apparatus is no exception. This chapter discusses some of the major problems and noise sources we encountered and how we overcome them, with a few other sections summarizing some interesting effects we observed. During noise study, a series of diagnosis tests was also developed to quickly identify problems when the gradiometer performance decreases without any obvious reasons.

### 7.1 Interferometer Simulator

To study various noise effect and to optimize system parameters, an interferometer simulator program using Monte Carlo technique was developed to simulate the atomic process of atom interferometer sequence. In particular, Raman beam intensity profile, atom cloud size and density distribution, atom cloud temperature and thermal motion during interferometer sequence, Raman beam single-photon detuning, and window attenuation between sensors (see section 6.3.2) are all taken into consideration. However, spontaneous emission effects (see section 7.2) and inertial effects mentioned in the error model (chapter 6) are not included in the simulator to simplify the model.

Standard parameters used in the model are shown in table 7.1, and pulse lengths and efficiencies are calculated by the simulator, shown in table 7.2.  $\pi$ -pulse length gets

longer because atom cloud expands during interferometer sequence thus the average Rabi frequency across the cloud decreases. Simulator also predicts overall contrast of this interferometer sequence to be 85%. Various parameters can be varied in this simulator to study noise effect and to find optimal parameters. Two examples will be discussed in the two sub-sections followed.

Parameter	Symbol	Value	Notes
Initial atom cloud 1/e-radius	$r_a$	2.2 mm	Measured by CCD camera
Atom cloud temperature	$T_a$	2.3 $\mu$ K	see section 7.3
Interrogation time	$T$	85 ms	
Raman beam 1/e-radius	$r_b$	6.5 mm	see section 7.1.2
Offset lock setting	$\Delta_O$	1.2 GHz	see figure B.1
Window transmissivity	$\eta$	93%	see section 6.3.2
Raman beam 1 power	$P_1$	130 mW	see figure B.1
Raman beam 2 power	$P_2$	96.3 mW	to null diff. ac Stark shift

Table 7.1: Standard parameters used in interferometer simulator.

Pulse #	Atom cloud 1/e-radius	$\pi$ -pulse length	$\pi$ -pulse efficiency
1	2.2 mm	3.5 $\mu$ s	94%
2	2.6 mm	3.6 $\mu$ s	92%
3	3.6 mm	3.9 $\mu$ s	84%

Table 7.2: Pulse performance calculated by interferometer simulator.

One important aspect of this interferometer simulator based on Monte Carlo technique is the statistical noise level. The more number of atoms per sample, the lower statistical noise in the simulator. Note that this noise has nothing to do with quantum projection noise [83], and the simulator is not subject to quantum projection noise because it calculates the exact final state  $|\Psi\rangle = c_1|g\rangle + c_2|e\rangle$ , and uses the coefficients  $c_1$  and  $c_2$  directly. The statistical noise is from the atom ensemble generation. For every shot a different atom sample is generated and each atom has different initial position and velocity. This randomization directly links to statistical noise. Also this

statistical noise is not pure phase noise, therefore results in section 5.1.1 cannot be applied to convert per-shot noise to per-ellipse noise. Full simulator and ellipse fitting algorithm are repeated to test the statistical noise directly, and the results are shown in table 7.3.

Atom number #	Statistical Noise (mrad/ellipse)
$10^3$	6.3
$2 \times 10^3$	4.2
$10^4$	1.98
$2 \times 10^4$	1.56
$10^5$	0.66
$2 \times 10^5$	0.49

Table 7.3: Noise level of interferometer simulator with different number of atoms in the sample. Ellipse fitting uses 20 data points per ellipse.

To get down to 0.5 mrad/ellipse (apparatus design goal) and study noise sources at that level,  $2 \times 10^5$  of atoms are needed per sample. We now proceed with two applications of this interferometer simulator.

### 7.1.1 Intensity Noise

Interferometry sequence is usually second-order sensitive to power fluctuation of the driving field (either optical or microwave). For example,  $\pi/2 - \pi/2$  microwave clock gives [50]

$$c_g = e^{i(\phi_2 - \phi_1)} \left[ -\sin\left(\frac{\theta_1}{2}\right) \sin\left(\frac{\theta_2}{2}\right) \right] + \cos\left(\frac{\theta_1}{2}\right) \cos\left(\frac{\theta_2}{2}\right), \quad (7.1)$$

where  $\Delta\phi = \phi_2 - \phi_1$  is the differential phase this sequence experiences between two pulses, and pulse area  $\theta_1$  and  $\theta_2$  are ideally  $\pi/2$ . In the presence of microwave power fluctuation, we can express this power noise in terms of pulse area noise:

$$\theta_i = \frac{\pi}{2} + \Delta\theta_i \quad i = 1, 2 \quad (\Delta\theta_i \ll 1). \quad (7.2)$$

And the probability of finding atoms in the starting state is:

$$|c_g|^2 = \frac{1}{2} [1 - \cos(\Delta\phi) \cos(\Delta\theta_1) \cos(\Delta\theta_2) + \sin(\Delta\theta_1) \sin(\Delta\theta_2)]. \quad (7.3)$$

This clearly shows the second-order sensitivity to the power fluctuation  $\Delta\theta_1$  and  $\Delta\theta_2$ .

However, in many cases intensity noise does limit the phase sensitivity of apparatus, and characterizing intensity noise becomes a necessity. Single  $\pi/2$ -pulse performance, commonly referred as  $\pi/2$ -test, is very sensitive to, and usually used to quantify intensity noise. Following equation 2.4, the probability of finding an atom in the other state after a pulse is

$$T(\Omega_{eg}, \delta, \tau) = \frac{\Omega_{eg}^2}{\Omega_{eg}^2 + \delta^2} \sin^2 \left( \sqrt{\Omega_{eg}^2 + \delta^2} \frac{\tau}{2} \right). \quad (7.4)$$

It is easier to work with this equation using “pulse-unit”, or expressing these three parameters in terms of standard condition:

$$\begin{cases} \Omega_{eg} &= \omega' \Omega_{eg0} \\ \delta &= \delta' \Omega_{eg0} \\ \tau &= t' / \Omega_{eg0} \end{cases} \quad (7.5)$$

The new parameter set  $(\omega', \delta', t')$  are unit-less, and ideally  $\omega' = 1$ ,  $\delta' = 0$ , and  $t' = \pi/2$  for a  $\pi/2$ -pulse. Equation 7.4 now becomes:

$$T'(\omega', \delta', t') = \frac{\omega'^2}{\omega'^2 + \delta'^2} \sin^2 \left( \sqrt{\omega'^2 + \delta'^2} \frac{t'}{2} \right). \quad (7.6)$$

The  $\pi$ -pulse is second-order sensitive to all three parameters:

$$T'(1 + \Delta\omega, \delta', \pi + \Delta t) \approx 1 - 2.47 (\Delta\omega)^2 - \delta'^2 - 0.25 (\Delta t)^2 - 1.57 \Delta\omega \cdot \Delta t. \quad (7.7)$$

On-resonance  $\pi/2$ -pulse has first-order sensitivity to pulse power and length (second-order terms are all ignored in the following  $T'$  expressions in this section):

$$T'(1 + \Delta\omega, \delta', \pi/2 + \Delta t) \approx 0.5 + 0.79 \Delta\omega + 0.5 \Delta t. \quad (7.8)$$

Another commonly used test is frequency-detuned  $\pi/2$ -test, in which pulse length is set to on-resonance  $\pi$ -pulse length but detuning is set at a value such that only half of the atoms are transferred to the other state. Condition  $T'(1, \delta_0, \pi) = 1/2$  gives  $\delta_0 = 0.799$ , and

$$T'(1 + \Delta\omega, \delta_0 + \Delta\delta, \pi + \Delta t) \approx 0.5 - 0.19 \Delta\omega - 0.95 \Delta\delta - 0.30 \Delta t. \quad (7.9)$$

This test has a strong sensitivity to frequency noise, and is sometimes used to characterize ac Stark noise in Raman system. In order to further reduce the sensitivity to  $\Delta\omega$ , one could tune both the detuning and pulse length until we null the first-order sensitivity to  $\Delta\omega$ :

$$\begin{cases} \partial T'(\omega', \delta', t')/\partial\omega' = 0 \\ T'(\omega', \delta', t') = 0.5 \\ \omega' = 1 \end{cases} \quad (7.10)$$

The first solution is  $\delta_d = 0.862$  and  $t_d = 0.933 \pi$ , and in this case:

$$T'(1 + \Delta\omega, \delta_d + \Delta\delta, t_d + \Delta t) \approx 0.5 - 0.862 \Delta\delta - 0.25 \Delta t. \quad (7.11)$$

Since pulse length timing is very accurate in our system, these tests mentioned above can be used to distinguish and characterize pulse power fluctuation (intensity noise) and frequency noise (ac Stark noise in Raman beams), respectively.

For the complete  $\pi/2 - \pi - \pi/2$  sequence, interferometer simulator is used to quantify the noise effect. An example is shown in figure 7.1. 1.5% intensity noise (rms) is added to one of the Raman beams ( $I_2$ ), while the other Raman beam is left to be stable. This intensity noise gives 0.75% Rabi frequency ( $\Omega_{\text{eff}}$ ) noise and 1.5% ac Stark ( $\delta_{\text{AC}}$ ) noise ( $\Omega_{\text{eff}} \propto \sqrt{I_1 I_2}$ , so  $\sigma_{\Omega_{\text{eff}}} = \sigma_{I_2}/2$ ; and  $\delta_{\text{AC}} = k_1 I_1 - k_2 I_2$ , so  $\sigma_{\delta_{\text{AC}}} = \sigma_{I_2}$ ). Interferometer contrast noise arises from these two effects, and simulation

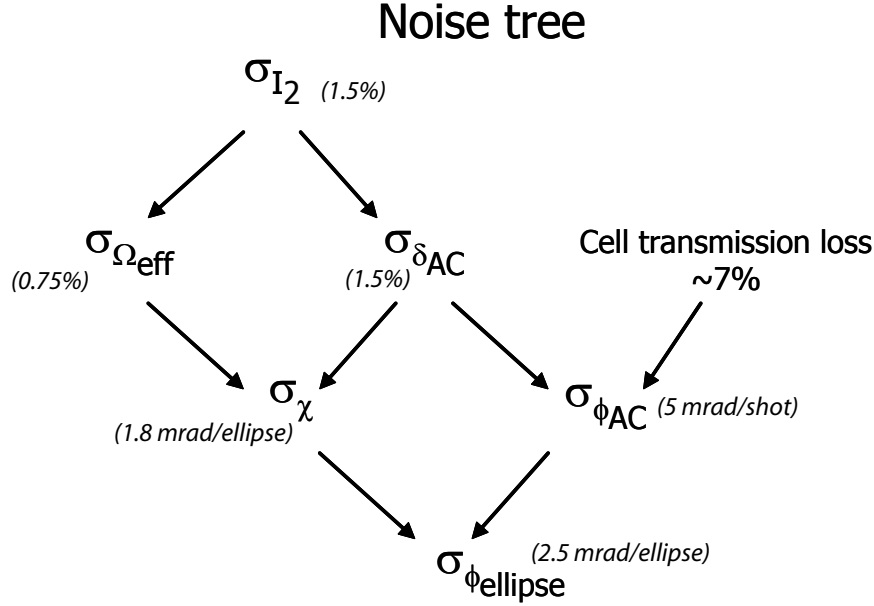


Figure 7.1: Intensity noise propagation to interferometer phase noise. 1.5% intensity noise (rms) in one of the Raman beams produces 2.5 mrad/ellipse phase noise in  $\pi/2 - \pi - \pi/2$  sequence. The other Raman beam is assumed to be stable.

shows contrast noise alone gives 1.8 mrad/ellipse phase noise ( $\sigma_\chi$ ). Note that although interferometer is second-order sensitive to intensity noise, this second-order effect is big enough to disturb contrast and standard ellipse fitting algorithm would pick that out as apparent phase noise.

On top of this contrast noise effect, the 7% Raman window attenuation mentioned in section 6.3.2 adds additional noise. Ac Stark phase noise effect is not completely canceled because two sensors receive 7% difference in Raman beam power. According to section B.1, ac Stark phase shift is about  $\pi$  rad/ $\pi$ -pulse, and 1.5% intensity noise gives  $\sim 50$  mrad/ $\pi$ -pulse ac Stark phase noise, which in turn gives  $\sim 4$  mrad/ $\pi$ -pulse differential ac Stark phase noise (differential in the sense of difference between two sensors, not between two Raman beams). Three pulse sequence adds this effect up to 5 mrad/shot differential ac Stark phase noise ( $\sigma_{\phi_{AC}}$ ), or 1.8 mrad/shot using conversion mentioned in section 5.1.1.  $\sigma_\chi$  and  $\sigma_{\phi_{AC}}$  combined give final phase noise of 2.5 mrad/ellipse ( $\sigma_{\text{ellipse}}$ ) which is confirmed by complete simulation as well.

This complete simulation of intensity noise shows that the Raman beam intensity noise has to be  $< 0.3\%$  to reach our interferometer design goal (0.5 mrad/ellipse).  $\pi/2$ -test gives us the tool to confirm Raman beam performance. Eventually, advanced Raman beam scheme could almost eliminate this effect of Raman beam intensity noise in our system (see section 9.1).

### 7.1.2 Raman Beam Size

With fixed amount of power in the Raman light, pulse transfer efficiency decreases as the beam size gets smaller because the Gaussian intensity profile cannot address the atoms at the edge of the cloud as effectively; however, the finite atom Doppler width makes the pulse transfer efficiency smaller as the beam size increases because the intensity and Rabi frequency decreases. Interferometer simulator was used to study the Raman beam size effect and to find the optimal beam size. Some of the results are shown in figure 7.2. In our apparatus,  $r_b \approx 6.5$  mm Raman beam size was chosen among a few trials of different beam sizes. Simulator confirms this result as well.

Similar study are done to optimize Raman beam single-photon detuning (offset lock setting  $\Delta_o$ ).

## 7.2 Spontaneous Emission

In our apparatus, two-photon transition is via a virtual level  $\sim 500$  MHz away from atomic energy levels to reduce spontaneous emission effect. However, spontaneous emission cannot be completely eliminated. Detailed calculation of spontaneous emission can be found in section B.2, and figure 7.3 shows some results as a function of Raman single-photon detuning.

Spontaneous emission has also been experimentally measured to compare with theory. In order to do that, Raman microwave frequency is tuned a few MHz away from resonance to eliminate two-photon transition. Simply turning on this off-resonance Raman pulse and observing atom loss gives the depumping rate due to spontaneous emission, and can be used to infer total spontaneous emission rate.

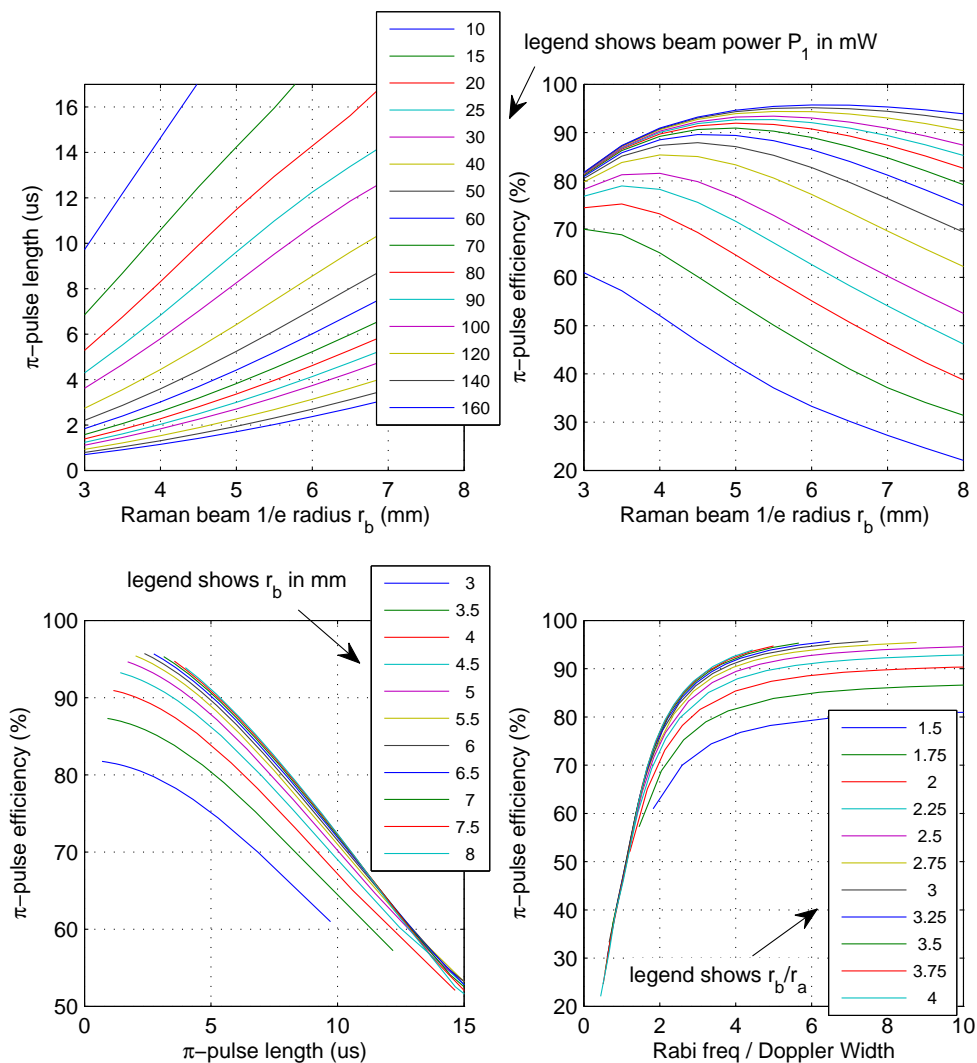


Figure 7.2: Various studies of Raman pulse efficiency and beam size. Top right figure shows that there is an optimal beam size for a fixed beam power. Bottom right figure shows that the ratio of Rabi frequency to atom Doppler width has to be at least 4 to have decent Raman pulse efficiency. Atom Doppler width is defined as  $k_{\text{eff}} \sqrt{k_b T_a / m_{\text{CS}}}$ .

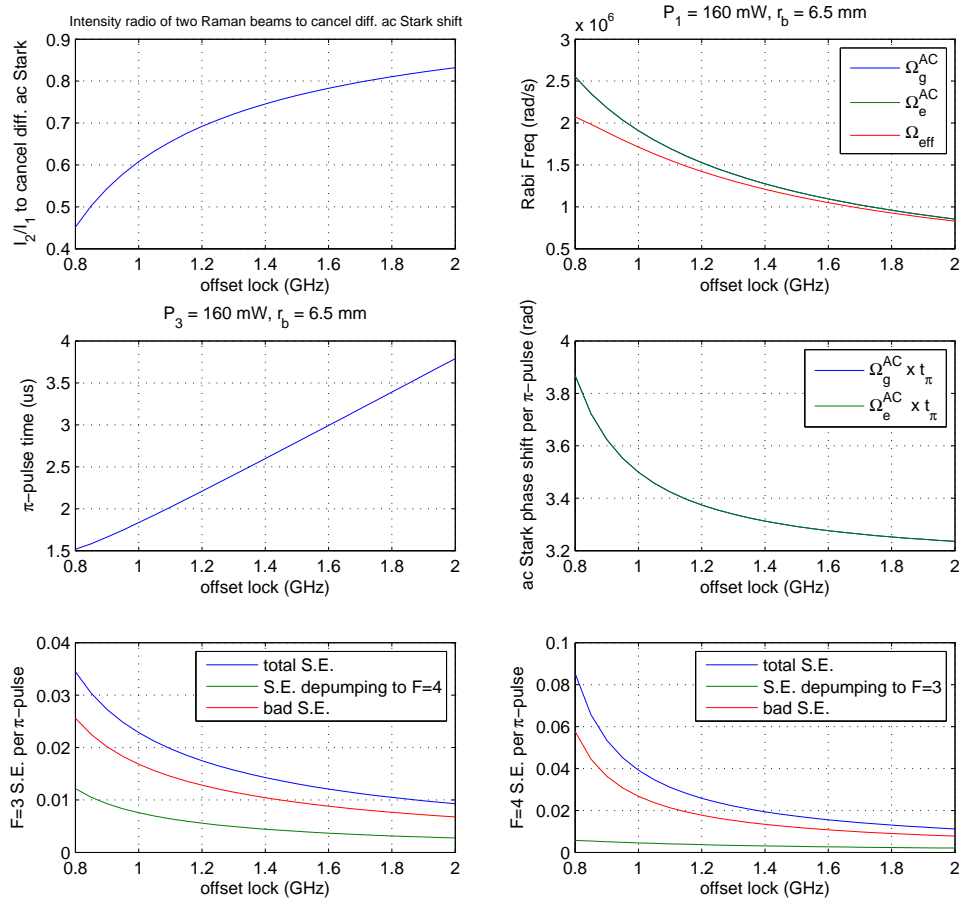


Figure 7.3: Spontaneous emission calculation: various results are plotted as a function of offset lock setting (refer to figure B.1).  $P_1 = 160 \text{ mW}$  and  $r_b = 6.5 \text{ mm}$  in this calculation, and  $P_2$  is calculated assuming differential ac Stark shift is always canceled.

A more elegant way is to insert this off-resonance Raman pulse into a clean microwave  $\pi/2 - \pi/2$  clock sequence (Uwave Clock with Optical Pulse Inserted, or UCOPI sequence), and the decrease in microwave clock contrast as a function of Raman pulse length gives clean measurement of spontaneous emission rate. UCOPI sequence has also been used to measure ac Stark phase noise because tuning Raman pulse off-resonance eliminates two-photon transition but leaves ac Stark effect largely unaffected.

### 7.3 Atom Cloud Temperature

Atom cloud temperature, or the average thermal velocity, is one of the most important numbers to determine optimal system parameters, such as Raman beam size (see section 7.1.2). This section outlines a number of ways to measure atom cloud temperature and attempts to explain the discrepancy in different measurements.

A conventional method to measure atom cloud temperature is the method of time-of-flight (TOF), observing cloud size increase in time. For collisionless expansion over a time  $t$  the 1/e-radius of the atom cloud is (see, e.g. [73] page 59)

$$r(t)^2 = r(0)^2 + 2\frac{k_b T_a}{m} t^2. \quad (7.12)$$

Therefore CCD camera image of atom cloud as a function of time gives us precise measurement of atom cloud temperature  $T_a$ . Note that the usual detection beams are used in taking CCD camera pictures, and we determined  $T_a = 2.3 \mu\text{K}$  in our apparatus with standard sequence parameters.

A better method to measure atom temperature is by scanning frequency of an extremely long Raman pulse, typically  $\sim 200 \mu\text{s}$ . Because the Raman pulse is extremely long, it only addresses those atoms moving near a particular velocity along Raman beam axis such that Doppler shift makes the atom on-resonance for Raman transition. Raman pulse transfer efficiency has a Gaussian profile as a function of Raman frequency detuning, and 1/e-size of this frequency profile ( $f_{1/e}$ ) gives atom

temperature as:

$$T_a = \frac{m_{Cs}}{k_b} \left( \frac{\sqrt{2}\pi}{k_{\text{eff}}} f_{1/e} \right)^2 = 1.46 \times 10^{-3} \frac{\mu\text{K}}{(\text{kHz})^2} (f_{1/e})^2. \quad (7.13)$$

Using standard sequence parameters (detecting atoms 230 ms after launching), we typically measure  $T_a = 2.3 \mu\text{K}$ , confirming CCD camera measurements. However, we measure  $T_a = 5 \mu\text{K}$  if we detect atoms 100 ms after launching (by launching at a slower speed).

Yet another method to measure atom temperature is the  $\delta T$ -scan (see section 3.2.2.3), and earlier investigation has been detailed in [74] section 6.5. Equation 3.69 is used to calculate atom temperature from contrast profile of  $\delta T$ -scan, and the results agree with extremely long Raman pulse measurements mentioned in the previous paragraph.

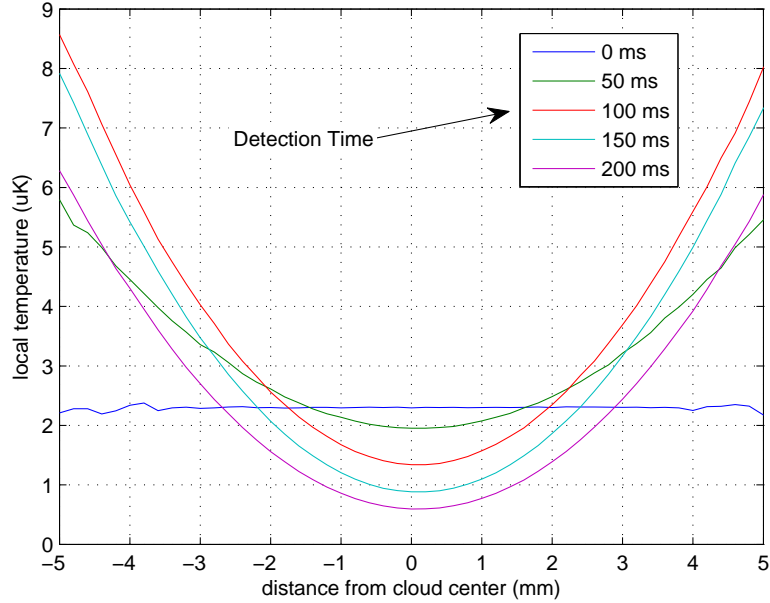


Figure 7.4: Temperature distribution across atom cloud, shown at different stage of the interferometer sequence. Atom cloud starts with 2.2 mm 1/e-radius and 2.3  $\mu\text{K}$  uniform temperature. Local temperature is defined as  $\langle m_{Cs} v_r^2 / k_b \rangle$  where average goes through atoms in the local area.

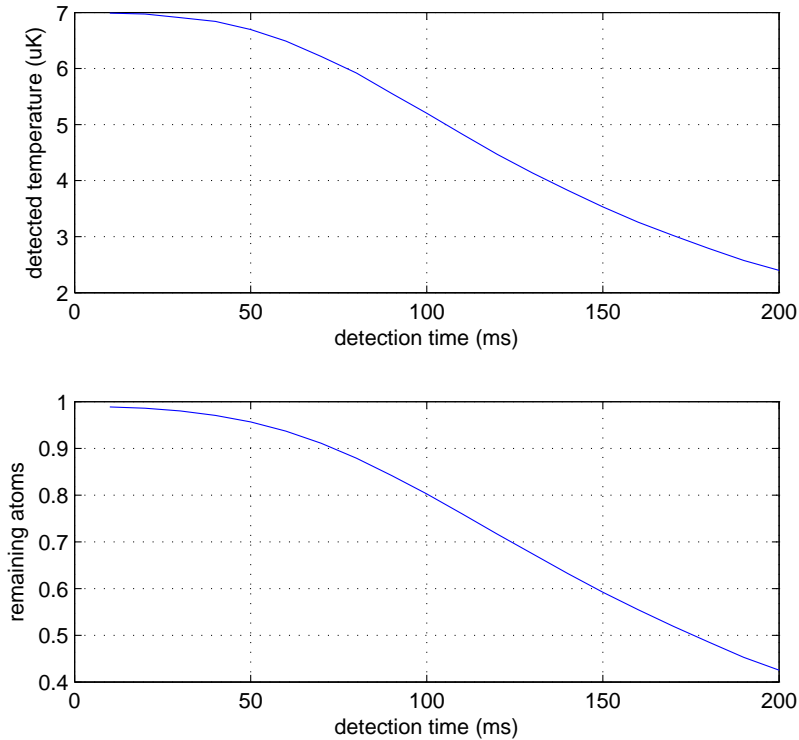


Figure 7.5: Detected atom temperature at different detection times. Atom cloud starts with 2.2 mm 1/e-radius and  $7 \mu\text{K}$  uniform temperature. Detection aperture is assumed to be 4.7 mm radius circle. After 200 ms, only 40% of the atoms are detected, with effective temperature at about  $2.5 \mu\text{K}$ . The atom loss as a function of detection time was quantitatively confirmed by experiment.

It becomes clear that the measured “apparent” atom temperature is a function of detection time, due to the fact that the apparatus detects different parts of the atom cloud with different efficiencies. This is because 1) detection beams have finite size such that only the center part of the atom cloud is illuminated, 2) the detection system picks up fluorescence only from the center part of the cloud due to detection aperture. Theory shows that the center part of the cloud becomes colder and colder as time elapses (see figure 7.4), and the detection aperture has dramatic effect on the atom temperature measurements. Figure 7.5 shows that with a 4.7 mm radius detection aperture (and homogeneous detection beam intensity), an atom cloud starting with 7

$\mu\text{K}$  temperature appears as  $5 \mu\text{K}$  after 100 ms, and  $2.5 \mu\text{K}$  after 200 ms. This theory confirms our observation and indicates that the atoms in our apparatus is much hotter than theoretical limit after cooling sequence (atomic clocks typically achieve  $0.5 \mu\text{K}$ ), and sub-Doppler cooling sequence may require further investigation and optimization. Nevertheless,  $2.3 \mu\text{K}$  atom temperature is still used in interferometer simulator because this sufficiently approximates the distribution of initial velocity of those atoms that are indeed detected at the end of the sequence.

## 7.4 Detection Bleedthrough Model

As mentioned in section 2.5, we separate  $|F = 4\rangle$  atoms from  $|F = 3\rangle$  atoms before detection and image them onto two quadrants on the detector to simultaneously integrate fluorescence from both atom states. Due to practical reasons, the separation between atom clouds is less than the cloud size, thus the clouds of two states are not completely separated during detection. A small amount of fluorescence from one state is detected in the other quadrant detector (bleedthrough). A simulated view of detection bleedthrough is shown in Figure 7.6. The separation pulse heats up  $|F = 4\rangle$  atoms to  $\sim 30 \mu\text{K}$ , so the  $|F = 4\rangle$  atom cloud (imaged onto upper quadrant C) is slightly larger than the  $|F = 3\rangle$  atom cloud due to thermal expansion after separation pulse.

The bleedthrough can be modeled as the following:

$$\begin{pmatrix} Q_A \\ Q_C \end{pmatrix} = K \begin{pmatrix} 1 & s_4 \\ s_3 & s \end{pmatrix} \begin{pmatrix} F_3 \\ F_4 \end{pmatrix} \quad (7.14)$$

Here  $Q_A$  and  $Q_C$  are the voltage integrated on the two quadrant detectors,  $K$  is a coefficient that converts atom number to detector voltage, and  $F_3$  and  $F_4$  are the actual atom numbers.  $s_4$  and  $s_3$  quantify the bleedthrough level and  $s$  is the detection efficiency of  $|F = 4\rangle$  atoms compared with  $|F = 3\rangle$  atoms, commonly referred as scaling in section 2.5.

Parameter  $s_3$ ,  $s_4$  and  $s$  can be experimentally determined by three different detection schemes following same interferometer sequence (e.g. scanning a microwave

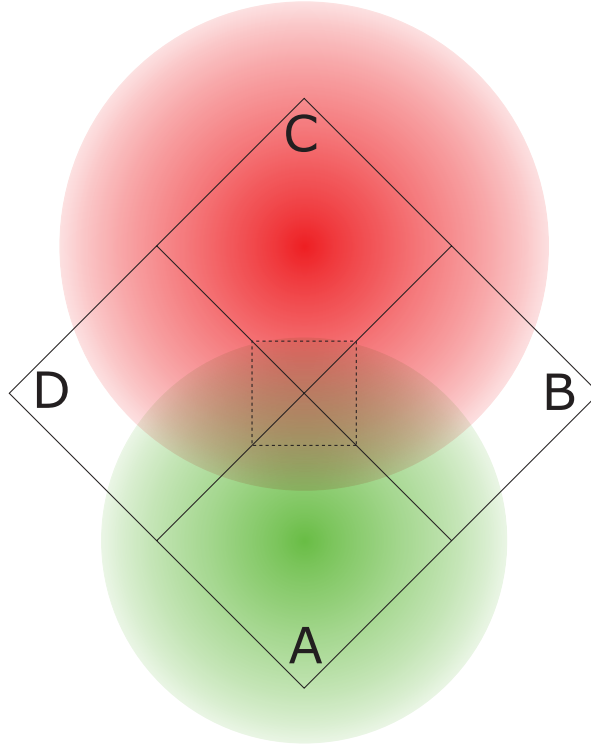


Figure 7.6: Detection bleedthrough diagram.  $|F = 3\rangle$  and  $|F = 4\rangle$  atom clouds are separated and imaged onto quadrants A and C, respectively. Fluorescence from one cloud bleeds through into the other cloud and is detected by the other quadrant. A black tape is placed in the dashed square to reduce (but not completely eliminate) the bleedthrough effect.

fringe). The three detection schemes are: 1) detecting  $|F = 3\rangle$  atoms only by blasting away  $|F = 4\rangle$  atoms before detection; 2) detecting  $|F = 4\rangle$  atoms only by not repumping  $|F = 3\rangle$  atoms before detection; and 3) standard normalized detection sequence. Suppose in three schemes, linear fitting of  $Q_A = kQ_C + b$  gives slope  $k_1$ ,  $k_2$  and  $k_3$ , respectively, then:

$$\begin{cases} k_1 = s_3 \\ k_2 = s/s_4 \\ 1 - k_3s_3 = s_4 - k_3s \end{cases} \quad (7.15)$$

Last equation assumes  $(F_3 + F_4)$  is a constant in normalized detection sequence. From the above three equations, one can solve  $s_3$ ,  $s_4$  and  $s$ . Typical numbers in

our apparatus are  $s_3 = 1\%$ ,  $s_4 = 5\%$ , and  $s = 0.85$ . Once these three numbers are experimentally determined, one can inverse the bleedthrough matrix to calculate actual  $F_3$  and  $F_4$  from measured voltage  $Q_A$  and  $Q_C$ :

$$\begin{pmatrix} F_3 \\ F_4 \end{pmatrix} = \frac{1}{K} \begin{pmatrix} 1 & s_4 \\ s_3 & s \end{pmatrix}^{-1} \begin{pmatrix} Q_A \\ Q_C \end{pmatrix} \quad (7.16)$$

Coefficient  $K$  is eliminated in calculating the normalized  $|F = 3\rangle$  atom number:

$$N_3 = \frac{F_3}{F_3 + F_4}. \quad (7.17)$$

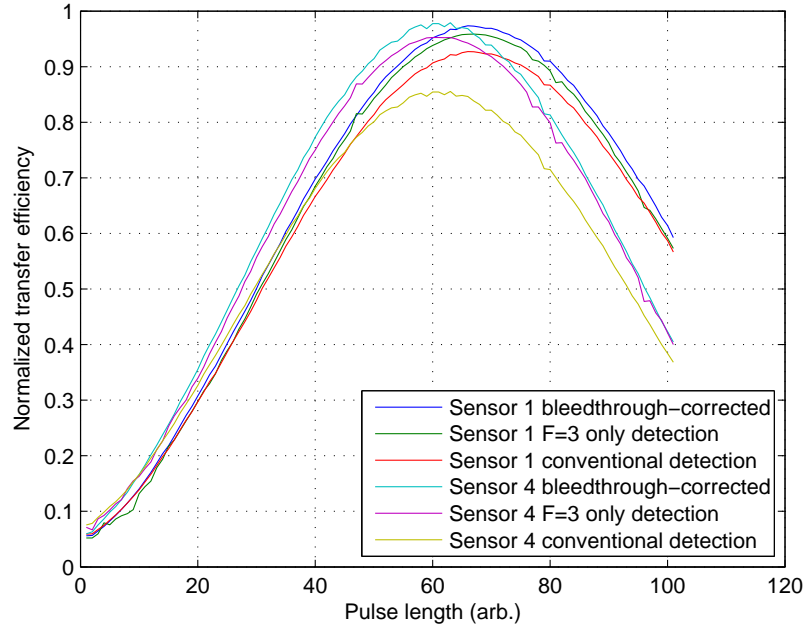


Figure 7.7: Bleedthrough correction for a microwave pulse efficiency measurement. Two sensors appear to have different pulse efficiency using conventional normalized detection algorithm, however bleedthrough correction reveals the same true efficiencies in two sensors.

Compared with conventional normalization method mentioned in section 2.5, this

bleedthrough correction model does not improve interferometer performance. However, bleedthrough correction is useful in determining the true pulse efficiency and comparing sensors with different bleedthrough levels. Figure 7.7 shows a typical bleedthrough correction algorithm that reveals the true microwave pulse efficiency in our system.

## 7.5 $0 \rightarrow 2$ Transition

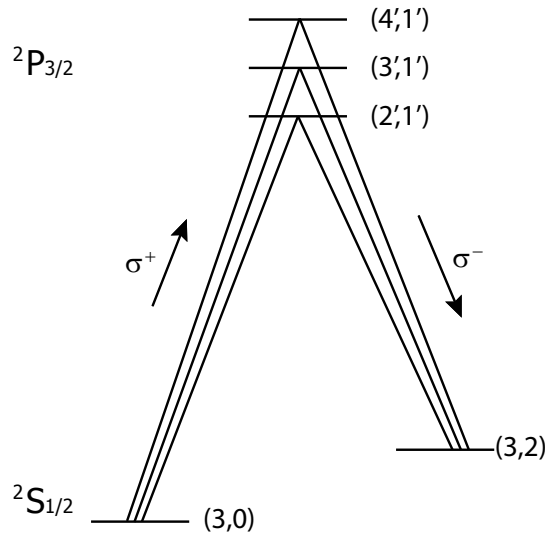


Figure 7.8:  $0 \rightarrow 2$  transition paths: example is shown for  $|F = 3, m_F = 0\rangle - |F = 3, m_F = 2\rangle$  coupling.

Cross-linearly polarized Raman beams drive two-photon stimulated Raman transition exactly the same as pure  $\sigma^+ - \sigma^+$  polarization, because the  $\sigma^+$  and  $\sigma^-$  components in cross-linear light both drive transition and their transition amplitudes add up. However, in linearly polarized case, atoms can undergo a  $0 \rightarrow 2$  transition via, e.g.

$$|F = 3, m_F = 0\rangle \xrightarrow{\sigma^+} |F' = 3, m_{F'} = 1\rangle \xrightarrow{\sigma^-} |F = 3, m_F = 2\rangle.$$

(see figure 7.8) There are three paths for  $|F = 3, m_F = 0\rangle - |F = 3, m_F = 2\rangle$  coupling,

and it turns out the transition amplitudes sum up to 0:

$$T = \sum_{F'=2'}^{4'} T_{3,0 \rightarrow F',1} \cdot T_{3,2 \rightarrow F',1} \quad (7.18)$$

$$= \sqrt{\frac{1}{14}} \sqrt{\frac{5}{21}} + \sqrt{\frac{3}{16}} \left( -\sqrt{\frac{5}{32}} \right) + \sqrt{\frac{25}{336}} \sqrt{\frac{5}{224}} = 0. \quad (7.19)$$

However, this zero-coupling is true only in the far-detuned limit. If the Raman beam is 1 GHz blue detuned, path  $|3,0\rangle \rightarrow |4',1'\rangle \rightarrow |3,2\rangle$  is slightly stronger than the other two paths, resulting non-zero coupling between  $|3,0\rangle - |3,2\rangle$  states. Figure 7.9 shows coupling strength as a function of single-photon detuning  $\Delta_O$ , normalized to corresponding coupling strength of  $|3,0\rangle - |4,0\rangle$  (the desired two-photon Raman transition). Similar calculation is done for couplings  $|3,0\rangle - |4,2\rangle$ ,  $|4,0\rangle - |4,2\rangle$ , and  $|4,0\rangle - |3,2\rangle$ .

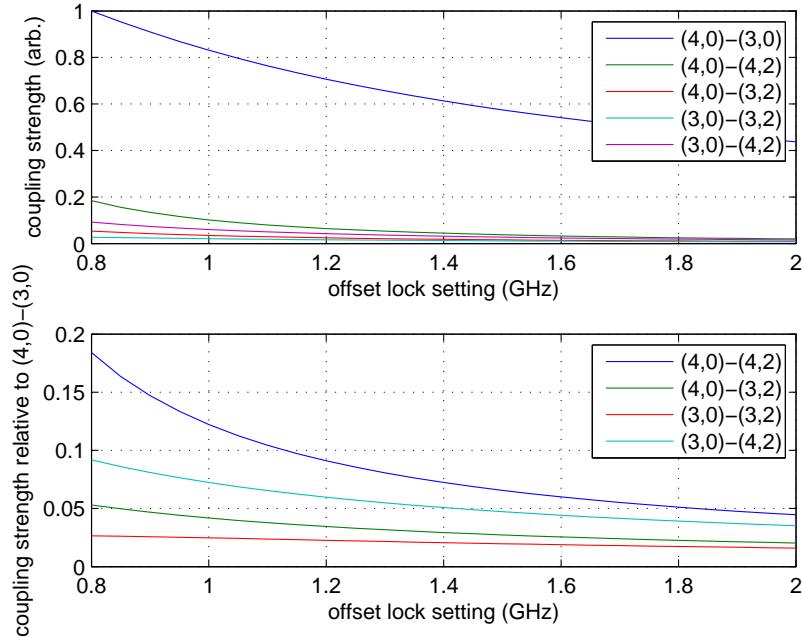


Figure 7.9:  $0 \rightarrow 2$  transition strength: bottom figure shows relative transition strengths of all four  $0 \rightarrow 2$  transitions compared to the desired 0 to 0 transition at their corresponding detuning frequency.

Coupling  $|4, 0\rangle - |4, 2\rangle$  is the strongest among these four  $0 \rightarrow 2$  transitions, and was easily observed experimentally. Figure 7.10 shows the observed  $|m_F = 2\rangle$  atoms after applying a linearly polarized Raman pulse to  $|F = 4, m_F = 0\rangle$  atoms. One can increase bias field to shift the magnetically sensitive level  $|m_F = 2\rangle$  away, making this  $0 \rightarrow 2$  transition off resonance and effectively suppressed. In our apparatus, this effect reduces interferometer contrast by  $\sim 1\%$  and does not impose a limit on interferometer performance.

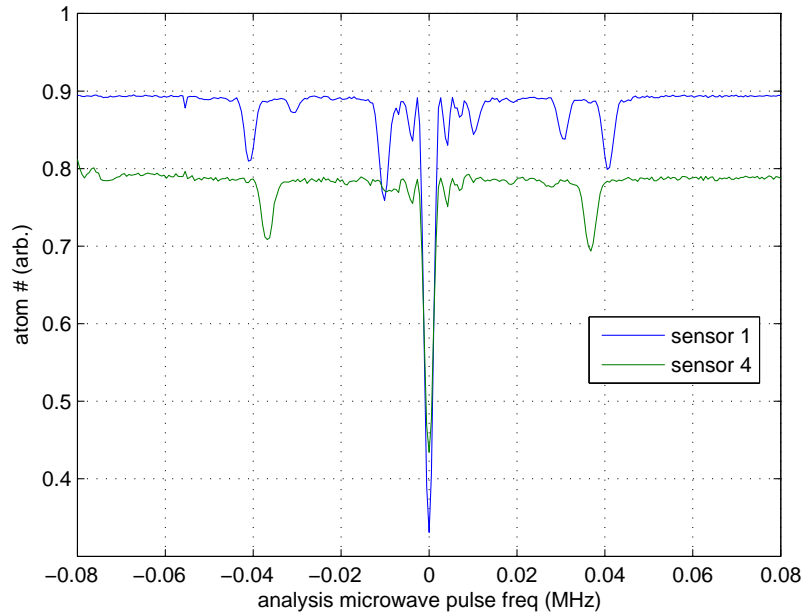


Figure 7.10: Observed  $0 \rightarrow 2$  transition. An analysis microwave pulse is fired after a linearly polarized Raman pulse applied to  $|F = 4, m_F = 0\rangle$  atoms. The frequency of this analysis microwave pulse is scanned to detect atom numbers in different  $m_F$  levels. Valleys near  $\pm 40$  kHz indicate  $|m_F = 2\rangle$  atoms, and there is no  $|m_F = 1\rangle$  atoms observed, confirming the theory. Valleys near  $\pm 30$  kHz and  $\pm 10$  kHz corresponds to microwave cross-transitions due to imperfectness of microwave field, and are not relevant here.

# Chapter 8

## Gravity Gradient Measurements

This chapter summarizes some gravity gradient measurements and related tests we conducted with the apparatus. This includes gradiometer performance characterization in the lab before moving the apparatus into the truck, the gravity gradient survey we did near our lab, and some related interesting tests to demonstrate the flexibility of our apparatus and ability to quantify system noise parameters with specially designed sequence and setup.

### 8.1 Gradiometer Performance

We performed a mass test in the lab to verify our gradiometer performance, using two stacks of Lead bricks, each about 540 kg. The source masses are chopped between two positions (detailed in [74] section 6.1.1) using precision positioning table, and the signal at each position is averaged for 40 sec which is empirically chosen to minimize the impact of slow drifts in the gradiometer phase (see section 5.1.1). The mass motion is synchronized with the interferometer timing system and data collection procedure, and mass positioning instability is negligible. The measured gravity field signal modulates between two values, giving a square wave output (see figure 8.1). Slow drift in the interferometer phase due to environment factors is largely removed by dedrifting methods (see section 5.5). The resulting difference signal of the chopped gradiometer phase is determined to be  $67.85 \pm 0.02$  mrad.

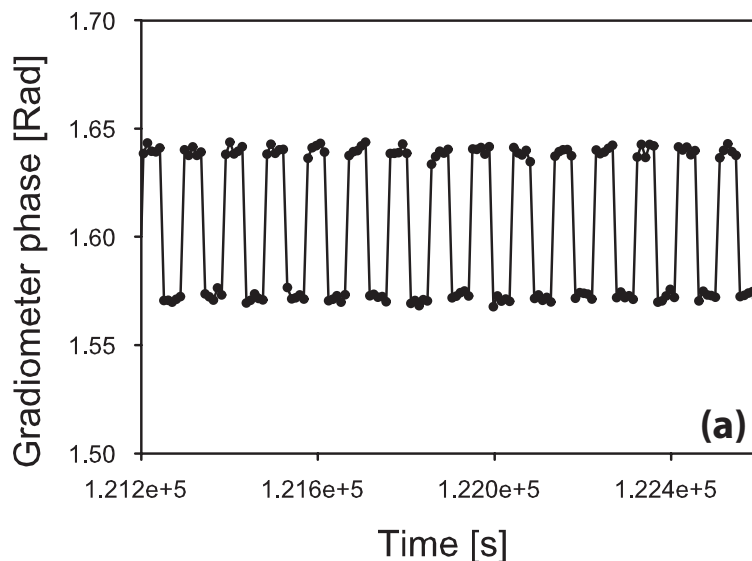


Figure 8.1: The gravity potential is chopped between two values to remove the sensitivity to long term drifts in phase. A typical section of data shows that the SNR of the modulated signal is 34 : 1 and the repetition rate is 0.01 Hz.

The resulting time records are concatenated for five days and an Allan deviation of this record (see figure 8.2) reveals that the mass signal integrates as  $1/\tau^{1/2}$  for  $10^5$  seconds ( $\approx 1$  day). The local de-drift algorithm results in a signature bump in the signal between  $10^2$  and  $10^4$  seconds (see section 5.5). At longer times, the accuracy of the Allan deviation is restored giving a mass signal uncertainty of  $\pm 0.15$  E after one day. In this test, two gradiometer phase readouts generate one mass-signal readout, thus mass signal sensitivity is twice worse than the actual gradiometer phase readout sensitivity. The measured mass signal sensitivity is  $10 \text{ mrad/Hz}^{1/2}$ , or  $48 \text{ E/Hz}^{1/2}$  with 1.8 meter baseline, assuming no down-time due to mass moving. The inferred gradiometer sensitivity is  $24 \text{ E/Hz}^{1/2}$ , with 0.08 E resolution after one day integration.

## 8.2 Gravity Anomaly Survey

A gravity gradient survey was conducted outside of a 4 story-deep Stanford University Hansen Experimental Physics Laboratory (HEPL) building, which measures  $28 \times 65$  meters around and 11 meters deep. The truck was driven along a linear profile

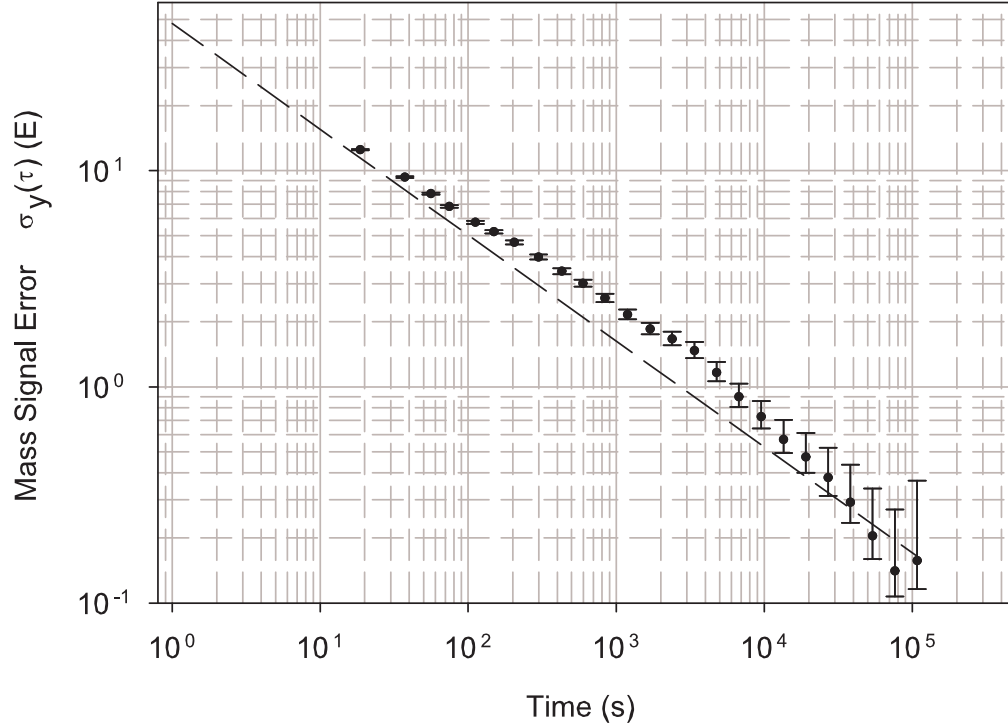


Figure 8.2: Allan deviation of the mass signal, assuming 1.8 m baseline.

extending inside the building's loading bay (see figure 8.3), and measurements were taken at points spaced roughly a meter apart.

The truck was advanced along the profile using the electric motor drive by remote computer control. This survey was conducted without a precision steering control, resulting in a small amount of non-repeatability in the yaw angle, which is estimated to be roughly 10% of the measured peak (details in section 8.4). In principle, truck orientation can be guided by two GPSs, but we compensated yaw angle with an actively controlled platform motor inside the truck so the Raman axis is always parallel with the desired survey line within 0.01 degree.

After coming to a stop and engaging the electric brakes, the sensor platform was levelled and about 5 minutes of gradient data was acquired. The current typical performance of the system allows for an integrated sensitivity of 20 E in 1 minute



Figure 8.3: Truck during gravity gradient survey. Truck is driven by an electric motor to take measurements along a linear profile. Apparatus is about 2.1 meters above the ground.

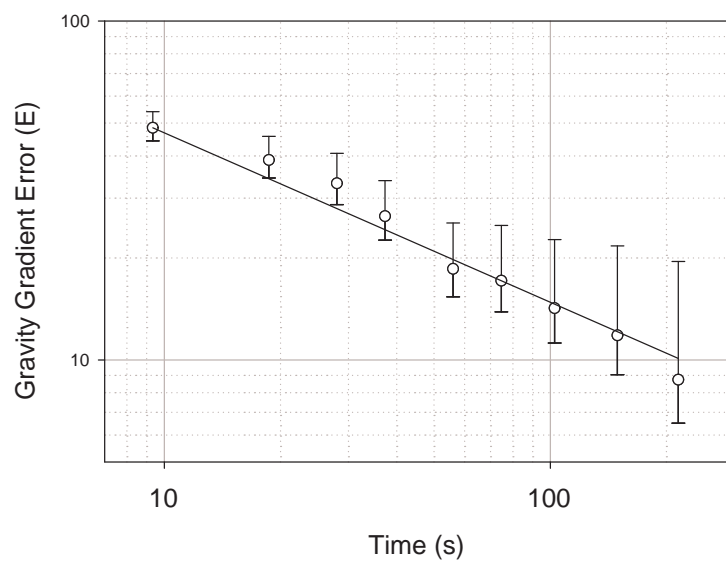


Figure 8.4: Typical Allan deviation of gravity gradient signal during survey.

and 10 E in 4 minutes, as indicated by the plot of the typical Allan deviation in figure 8.4. The best performance seen so far was integrated sensitivity of 5 E in about 4 minutes.

The truck routinely comes back to the reference point so that the slow drift in absolute gradiometer phase (due to environment such as temperature) can be linearly interpolated over and taken out. The remarkable repeatability of the gravity gradient measurements reassures the effectiveness of this slow drift correction.

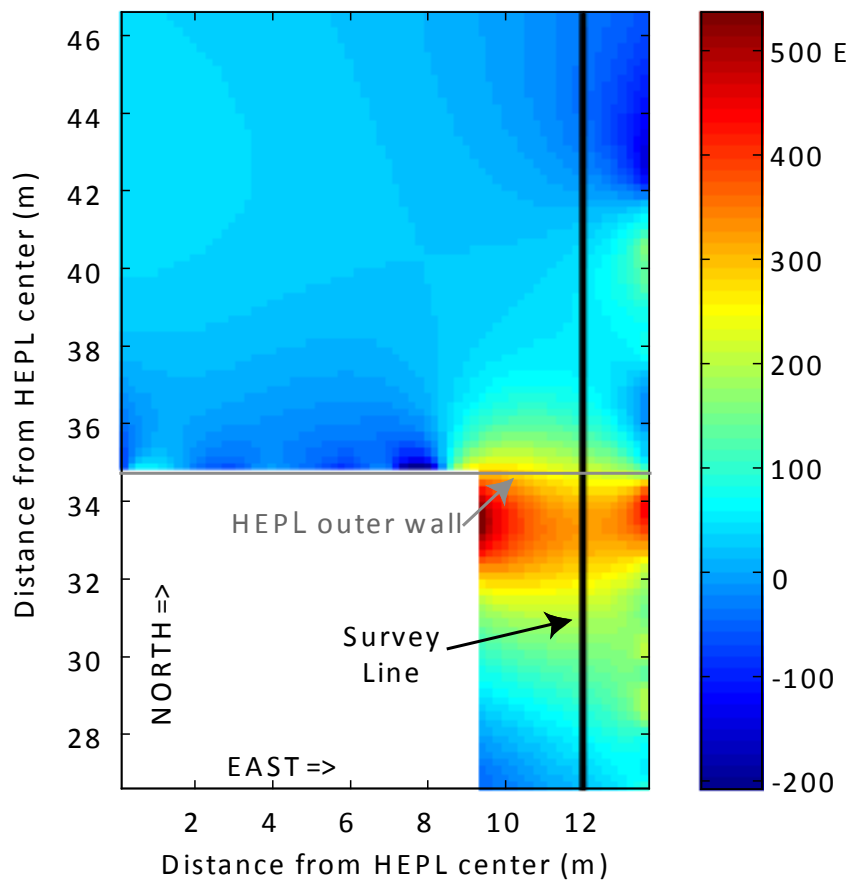


Figure 8.5: False color map of calculated  $T_{yy}$  gravity gradient. The main peak (shown red) is due to missing concrete wall at the HEPL main garage door. Survey was taken along the solid black line from roughly 4 meters inside the HEPL wall to 8 meters outside. The GPS coordinates of the survey reference point (survey line at the HEPL outer wall) are 37.42745 N, 122.17434 W.

The gradient signature of the surveyed anomaly was modeled including the 2 meter thick walls of the building and nearby raised soil level, using Monte Carlo technique. In short, random source points  $(x_s, y_s, z_s)$  are picked around the survey location  $(x_0, y_0, z_0)$  and density  $\rho(x_s, y_s, z_s)$  at each point is used for calculating the gravity gradient generated by mass near that point (with simulation unit volume  $dV$ ):

$$T_{yy} = \sum_s G\rho(x_s, y_s, z_s) dV \frac{(x_0 - x_s)^2 - 2(y_0 - y_s)^2 + (z_0 - z_s)^2}{[(x_0 - x_s)^2 + (y_0 - y_s)^2 + (z_0 - z_s)^2]^{5/2}}. \quad (8.1)$$

Figure 8.5 is the map of the simulated gradient, with the black line indicating the survey route. Figure 8.6 is the processed gradiometer data showing the gravity gradient measurements as well as the modeled profile.

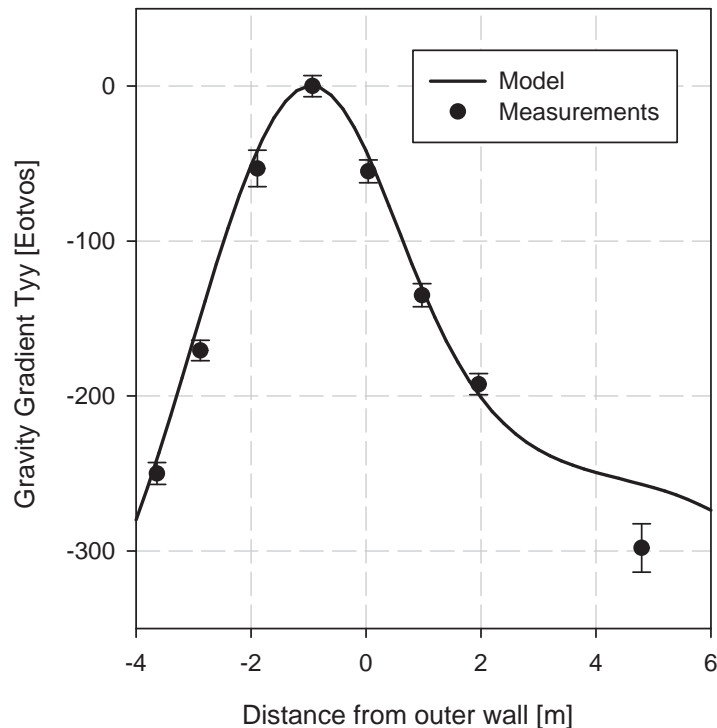


Figure 8.6: Gravity gradient survey measurements compared with model calculation. The model has large uncertainty in various dimensions and densities, and it agrees with the measurements to large extent.

### 8.3 Baseline Determination

As pointed out in [44], and discussed in section 3.3, single-photon detuning of Raman laser frequency is a source of noises, and can be a limiting factor in atom interferometer measurements if not controlled. We present here a clear effect of this and indeed take advantage of this effect to measure the distance between two atom clouds (baseline). This is an important measurement in gravity gradient measurements.

Acceleration of the atoms are measured by the optical ruler of Raman laser, whose wavelength serves as the tick markers of the ruler. Suppose the atom clouds are launched with a separation of  $L$  and a small relative velocity  $v_b$  towards each other due to launching angle mismatch. The extra differential laser phase between sensors due to this launching angle mismatch is

$$\Delta\phi = k_{\text{eff}}L - 2k_{\text{eff}}(L - v_bT) + k_{\text{eff}}(L - 2v_bT) = 0, \quad (8.2)$$

where  $T$  is the interrogation time. Launching angle mismatch is therefore not a problem in the measurement. However, if one changes the Raman laser frequency by  $\delta\nu$  for the first pulse only, then this extra differential laser phase becomes:

$$\Delta\phi = (k_{\text{eff}} + 2\pi\delta\nu/c)L - 2k_{\text{eff}}(L - v_bT) + k_{\text{eff}}(L - 2v_bT) = 2\pi\delta\nu L/c. \quad (8.3)$$

It is clear that this technique can be used to measure baseline  $L$ . We experimentally used  $\nu = 5.617$  MHz, and measured  $\Delta\phi = 236.6 \pm 0.3$  mrad after one hour integration, and that translates to  $1.0049 \pm 0.0015$  m baseline during first pulse. Note that this baseline is optical length which includes the effect of index of refraction of the Raman window. The actual physical distance between atom clouds is slightly smaller than this (see [74] section 6.3). Similarly, by switching Raman laser frequency for the other two pulses, distances between atom clouds during these pulses can be measured independently. The result is plotted in figure 8.7, and it is clear that launching angle mismatch exists and is estimated at about 1.7 degrees in this test setup. Although this measurement cannot measure horizontal launching velocity of individual sensor, only the relative horizontal launching velocity between sensors is important in the

interferometer model, and launching angle mismatch is sufficient for noise decorrelation.

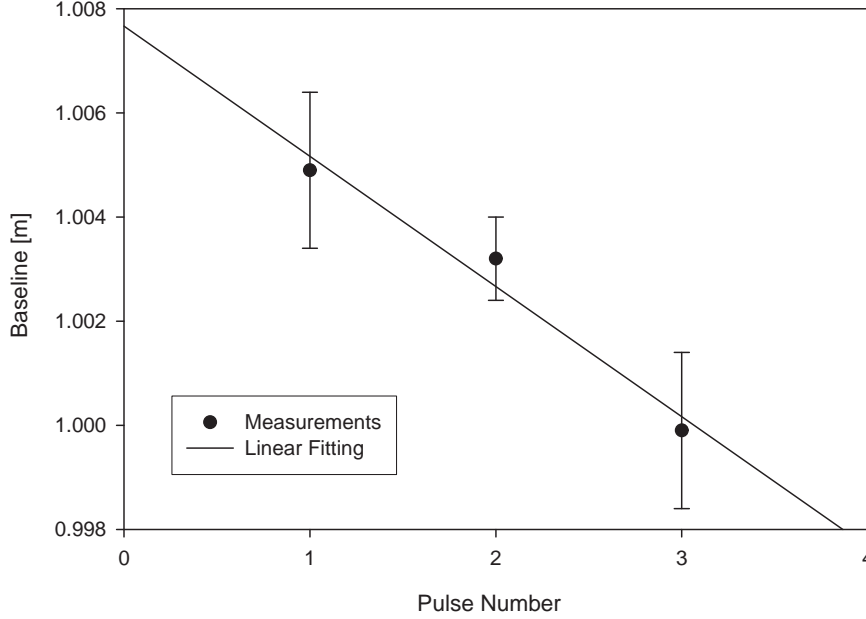


Figure 8.7: Baseline independently measured with three pulses in  $\pi/2 - \pi - \pi/2$  sequence. Linear trend indicates a small launching angle difference between two sensors, estimated as about 1.7 degrees.

## 8.4 Absolute Gravity Gradient Measurement

As pointed out in section 1.1, the horizontal inline gravity gradient measurement measures a combination of different components of the local gravity gradient tensor (assuming polar angle  $\phi = \pi/2$  in equation 1.6):

$$T_{\theta}^{\text{inline}} = T_{xx} \cos^2 \theta + T_{yy} \sin^2 \theta + T_{xy} \sin(2\theta) \quad (8.4)$$

$$= (T_{xx} + T_{yy})/2 + (T_{xx} - T_{yy}) \cos(2\theta)/2 + T_{xy} \sin(2\theta). \quad (8.5)$$

The gravity gradient sensor readout varies with the inline measurement angle  $\theta$ . If one changes  $\theta$  by a small amount  $\Delta\theta$ , the change in  $T_\theta^{\text{inline}}$  depends on  $\theta$ :

$$\Delta T_\theta^{\text{inline}}(\Delta\theta) = [-(T_{xx} - T_{yy}) \sin(2\theta) + 2T_{xy} \cos(2\theta)]\Delta\theta. \quad (8.6)$$

In particular, when  $\theta = 0$ :

$$\Delta T_{\theta=0}^{\text{inline}}(\Delta\theta) = 2T_{xy}\Delta\theta. \quad (8.7)$$

By chopping gradiometer apparatus yaw angle by  $\Delta\theta$  near  $\theta = 0$ , we can measure the interferometer phase shift and infer  $T_{xy}$ . This is an absolute measurement - we are not comparing with a reference position. By doing similar measurement near  $\theta = 45^\circ$ , we can measure  $(T_{xx} - T_{yy})$  absolutely. Note the Earth gravity gradient has  $(T_{xx} - T_{yy}) = T_{xy} = 0$ , so these measurements are sensitive to only the gravity gradient modified by local structure.

We experimentally chopped yaw angle by  $\Delta\theta = 6$  degrees (limited by platform control system hardware), and acquired chopping data for about 2 hours for each measurement axis ( $\theta$ ) at the  $T_{yy}$  peak on the survey line (see figure 8.5 and 8.6, 1 m inside HEPL outer wall). Using similar simulation as in figure 8.5, we expect  $T_{xx} \approx -400$  E,  $T_{yy} \approx 300$  E, and  $T_{xy} \approx -200$  E at this location. Figure 8.8 shows the measurement results as well as model fit using equation 8.6. The fitting results indicate  $(T_{xx} - T_{yy}) = -700 \pm 200$  E, and  $T_{xy} = 0 \pm 300$  E, which agree with the prediction of model simulation.

## 8.5 Motion Sensitivity

Although linear acceleration of the platform is canceled between two sensors in our gravity gradient measurement, rotation effect is not canceled and creates one of the noise sources. In this section we explore some of these effects, particularly how it affects atom interferometer contrast. More detailed analysis is followed in [78].

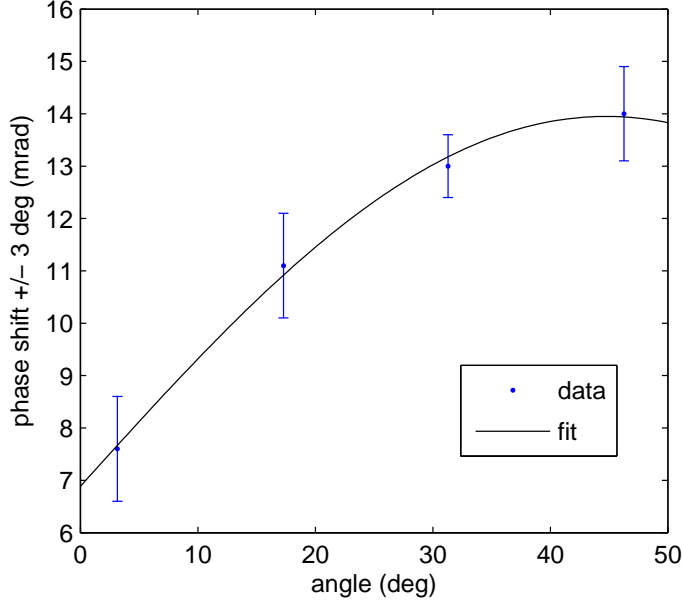


Figure 8.8: Yaw chop test. Yaw angle is chopped by 6 degrees and phase shift is measured as a function of truck orientation.

### 8.5.1 Yaw Rotation Response

A simple example to show rotation effect is to rotate apparatus yaw angle at a constant rate  $\omega$  during interferometer sequence and observe its effect on contrast and differential phase. Yaw rotation was chosen because rotating yaw does not change atom launching angle with respect to the detection system thus has minimum side-effect on the apparatus. Following analysis in section 3.2.2.4 and 6.5, the leading terms in contrast and differential phase shift are:

$$\chi(\omega) = \exp\left(-2T^4\omega^2k_{\text{eff}}^2v_{\text{rms}}^2\right), \quad (8.8)$$

$$\Delta\phi(\omega) = 2k_{\text{eff}}\omega T^2(v_h + \omega L), \quad (8.9)$$

where  $v_h$  is the transverse initial velocity mismatch between two sensors (see equation 6.94), and  $L$  is the baseline. We measured yaw rotation effect on interferometer contrast and phase at various rotation rate (see figure 8.9). The measurement of contrast

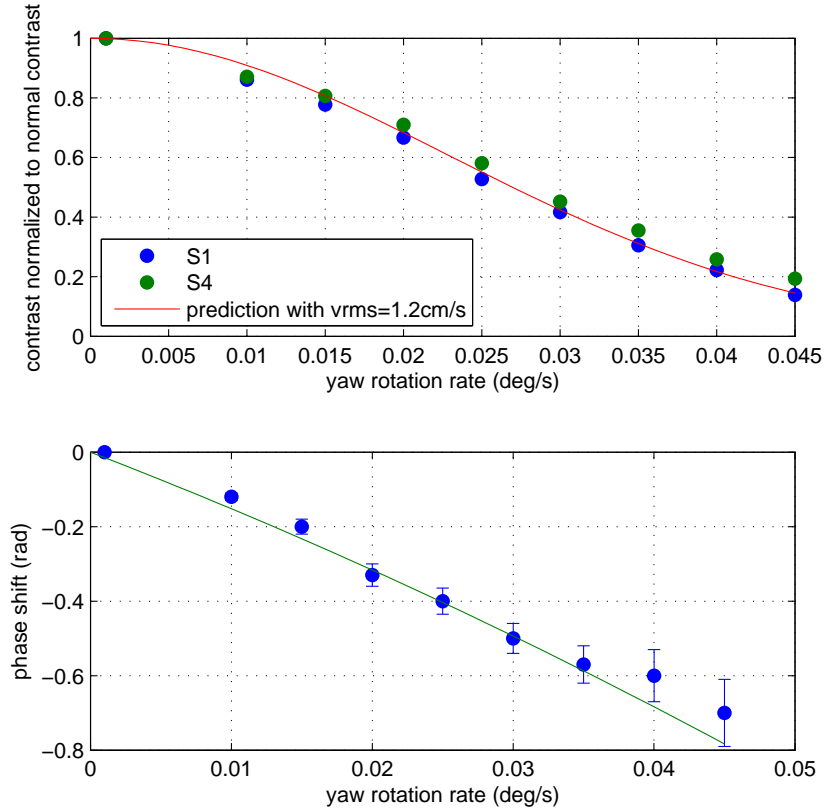


Figure 8.9: Yaw rotation test. Contrast prediction assumes  $v_{\text{rms}} = 1.2 \text{ cm/s}$  ( $T_a = 2.3 \mu\text{K}$ ), and the phase fitting curve indicates a transverse initial velocity mismatch  $v_h = 3 \text{ mm/s}$ .

as a function of rotation rate agrees with model perfectly, and the measurement of phase can be used to quantify  $v_h$ .

If we rotate yaw in the reverse direction, we could plot this contrast curve in a wider range, and maximum contrast is achieved when our yaw rotation rate exactly cancels the Earth rotation in yaw. This was not attempted experimentally but the proof-of-principle test already proves that the earth rotation (at  $0.004 \text{ deg/s}$ ), with our apparatus parameters, reduces atom interferometer contrast by  $\sim 1\%$ . That is an unneglectable effect in predicting interferometer contrast limit. It is also interesting to note that contrast reduction is not always an enemy to fight with but can potentially

be our friend to independently estimate rotation rate, and to stabilize the long term drifts of the conventional gyro [84].

### 8.5.2 Disturbance Sensitivity

As discussed in the error model (section 6.1), contrast noise and phase noise almost always appear together and it is difficult to distinguish these two effects experimentally because ellipse fitting is sensitive to both noise sources. We developed a synchronized test protocol to clearly separate the contrast effects and phase effects due to platform motion. Such study is important because it could extract system noise parameters and later be used for motion decorrelation. Experimentally, we run platform at a special frequency  $f = 1/(2T)$ , and synchronize atom interferometer sequence with the platform motion. The phase between the interferometer sequence and the platform motion is adjustable. Consider a simple model with platform motion in pitch <sup>1</sup>:

$$\theta_x(t) = A \cos\left(2\pi\frac{1}{2T}(t - t_0) + \phi_p + \phi_0\right), \quad (8.10)$$

where the adjustable  $\phi_p$  is called platform phase.  $\phi_0$  is to account the platform data acquisition phase lag. The Raman beam angle at three pulses are then:

$$\begin{cases} \theta_{x1} = \theta_x(t_0) & = A \cos(\phi_p + \phi_0) \\ \theta_{x2} = \theta_x(t_0 + T) & = -A \cos(\phi_p + \phi_0) + \gamma_v \\ \theta_{x3} = \theta_x(t_0 + 2T) & = A \cos(\phi_p + \phi_0), \end{cases} \quad (8.11)$$

where additional angle  $\gamma_v$  is added to the second pulse to represent the Raman beam vertical misalignment angle between top and bottom Raman beams. This angle  $\gamma_v$  is typically on the order of 1  $\mu$ rad due to corner cube and Raman window imperfection. Plugging equation 8.11 into equation 6.24, assuming yaw is stable, we get the interferometer contrast:

$$\chi(\phi_p) = \exp\left[-k_{\text{eff}}^2(r_0^2 + 2v_{\text{rms}}^2(t_0 + T)^2)(2A \cos(\phi_p + \phi_0) - \gamma_v)^2\right]. \quad (8.12)$$

---

<sup>1</sup>Chetan Mahadeswaraswamy first proposed this actuation.

In the synchronized test, platform phase  $\phi_p$  is stable, therefore interferometer contrast  $\chi(\phi_p)$  is stable, giving ellipse fitting a perfect chance to extract the differential phase. Meanwhile, by comparing the ellipse dimensions to the clean ellipse (with no platform noise), we can derive the contrast loss due to platform motion. The remarkable distinction between phase effects and contrast effects are clearly shown in the raw data (see figure 8.10).

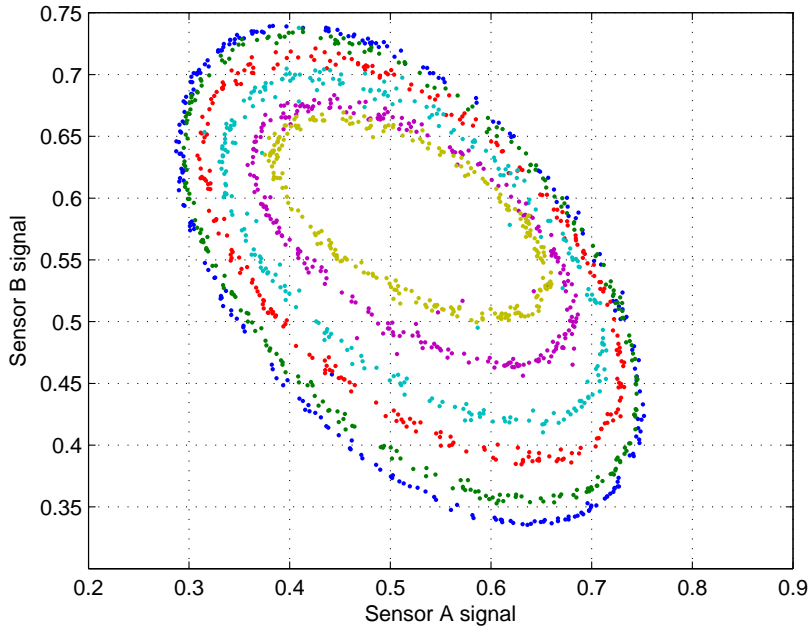


Figure 8.10: Synchronized disturbance test shown as different colored ellipses for different platform phases  $\phi_p$ .

We fix parameters  $r_0 = 2.2$  mm and  $v_{\text{rms}} = 1.2$  cm/s as atom cloud initial conditions, and fit free parameters  $A$ ,  $\phi_0$ , and  $\gamma_v$  in equation 8.12 using experimental data. Results are shown in table 8.1 and figure 8.11.

Platform data shows  $A \approx 1$  mdeg in pitch. The fitting results do not agree with that. It is possible that LN250, which is used to measure platform disturbance, overestimates platform disturbance due to internal digital filters. It is also possible that the parameter  $r_0$  or  $v_{\text{rms}}$  is incorrect, although both of them were confirmed by many independent measurements. Detection system might contribute to this discrepancy as

Parameter	Sensor A	Sensor B	Unit
Disturbance amplitude $A$	0.665(10)	0.789(7)	mdeg
Raman misalignment $\gamma_v$	-0.56(28)	1.47(17)	$\mu\text{rad}$
Phase lag $\phi_0$	-0.925(20)	-0.933(9)	rad

Table 8.1: Synchronized disturbance test fitting results.  $1\sigma$ -bounds are shown in parentheses.

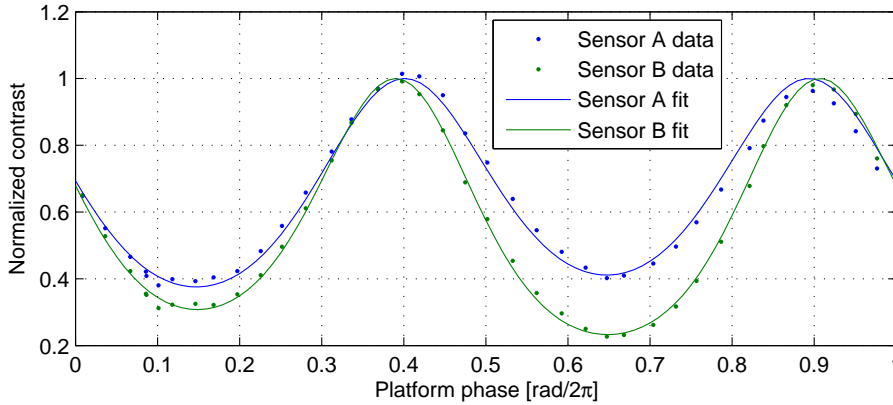


Figure 8.11: Synchronized disturbance test result: contrast as a function of platform phase is fitted with the contrast model.

well. Note that LN250 data also shows that platform has about 0.4 mdeg-amplitude in-phase oscillation in yaw, which is not intended. The effect of this yaw motion in contrast is almost an order of magnitude smaller, and is thus ignored in analysis and fitting.

The parameter  $\gamma_v$  introduces asymmetry between two valleys in contrast curve in figure 8.11. Fitting confirms that  $\gamma_v$  is not 0 in both sensors, yet within specification of corner cube. The difference between two  $\gamma_v$ s is most likely due to Raman window steering between two sensors.  $\phi_0$  is the same for two sensors, as expected.

While contrast effects are relatively easy to understand and model, phase effects involve many more terms and free parameters. More complete analysis and experiment, as well as studies of other disturbance frequencies, can be found in [78].

# Chapter 9

## Conclusion

A compact mobile atom interferometer based on two-photon stimulated Raman transitions in a dual atomic fountain has been developed for precision gravity gradient survey and other gravity tests. Various noise sources have been identified and overcome, and a differential acceleration sensitivity of  $4.2 \times 10^{-9} g/\sqrt{\text{Hz}}$  has been demonstrated over a 70 cm baseline in the laboratory. The apparatus was then moved into a box-truck and a gravity gradient survey was conducted near a 4 story-deep building, at an accuracy of  $7 \times 10^{-9}/\text{s}^2$  in gravity gradient with about three minutes integration at each survey point. The survey results agreed with a theoretical model considering detailed floor plan and building structure. In addition, technique to measure absolute gravity gradient was demonstrated. Finally, a complete dynamic model of the  $\pi/2 - \pi - \pi/2$  sequence was established, and potential algorithms to de-correlate apparatus platform noise during survey based on this model were identified.

### 9.1 Future Improvements

The current performance of gravity gradient survey is limited by various factors in the apparatus, although it is not certain which particular noise source is the primary one. Major noise sources has been identified and can be reduced in the near future or next generation of the apparatus. Here we list a few of them: Detection system can be further optimized, particularly increasing the separation between two clouds

during detection would suppress bleedthrough (see section 7.4) and null the sensitivity to separation beam [67]. Raman source can use even higher finesse cavity to further reduce linewidth and boost stability [85]. Multi- $\hbar k$  sequence (3.4) is under investigation in the hope of doubling or even tripling the gravity gradient sensitivity without hardware changes. High power tapered amplifier has proved to be stable in overdriven pulse-mode operation [86], and can potentially give us the opportunity to explore bigger size Raman beams and larger single-photon detuning without losing performance. If Raman beam does have power to spare, one could even balance differential ac Stark shifts for individual beam, so that Raman beam intensity noise would not introduce ac Stark shift noise into the interferometer.

If we were to retrofit the apparatus, there are a few things we can improve. The Raman window is not ideal in current generation of apparatus (see section 6.3), and the wedge and the attenuation problem can be fixed with better specification in fabrication. Trapping more atoms is also possible with a tapered amplifier delivering high power trap light to the sensor. Magnetic field servo can be improved by putting in an additional magnetometer in the sensor head to interpolationally measure the true magnetic field at the atom cloud. Isolation of the thermal source from the glasscell can be improved in order to reduce Raman window wedge effects.

In terms of interferometer simulation, work has been done to analyze the inertial model (see section 6.5), atomic process (Raman simulator mentioned in section 7.1), and part of the detection process (see section 7.4). A combined model of all these work, with a model of realistic detection beam, could simulate the complete process in this atom interferometer work, and can potentially be used to extensively study various noise sources and their interactions. Furthermore, there is still room for improvements in the data processing algorithm, particularly using Bayesian estimation [81].

# Appendix A

## Characteristic Data

Quantity	Symbol	Value (SI)
Speed of light	$c$	$2.997\,924\,58 \times 10^8$ m/s (exact) [87]
Planck's constant	$\hbar$	$1.054\,571\,596(82) \times 10^{-34}$ J·s
Boltzmann's constant	$k_b$	$1.380\,650\,3(24) \times 10^{-23}$ J/K
Melting point	$T_M$	28.44 °C [88]
Atomic mass	$m_{\text{Cs}}$	$2.206\,946\,50(17) \times 10^{-25}$ kg [89]
Frequency	$\omega_0$	$2\pi \cdot 351\,725\,718.50(11)$ MHz [90]
Wavelength (Vacuum)	$\lambda$	852.347 275 82(27) nm
Lifetime	$\tau$	30.473(39) ns [91, 92, 93]
Natural linewidth	$\gamma$	$2\pi \cdot 5.2227(66)$ MHz
Hyperfine splitting ( $6^2\text{S}_{1/2}$ )	$\omega_{\text{HF}}$	9.192 631 770 GHz (exact)
Clock transition Zeeman shift	$\Delta\omega_{\text{clock}}/B^2$	$2\pi \cdot 427.45$ Hz/G <sup>2</sup>
Doppler temperature	$T_D$	125 $\mu$ K [64]
Doppler velocity	$v_D$	8.82 cm/s
Recoil temperature	$T_r$	198 nK
Recoil velocity	$v_r$	3.52 mm/s
Saturation intensity	$I_s$	1.1023(10) mW/cm <sup>2</sup>

Table A.1: Useful constants and relevant Cs D<sub>2</sub> properties for the  $6^2\text{S}_{1/2} \rightarrow 6^2\text{P}_{3/2}$  on the  $|F = 4\rangle \rightarrow |F' = 5\rangle$  cooling transition.

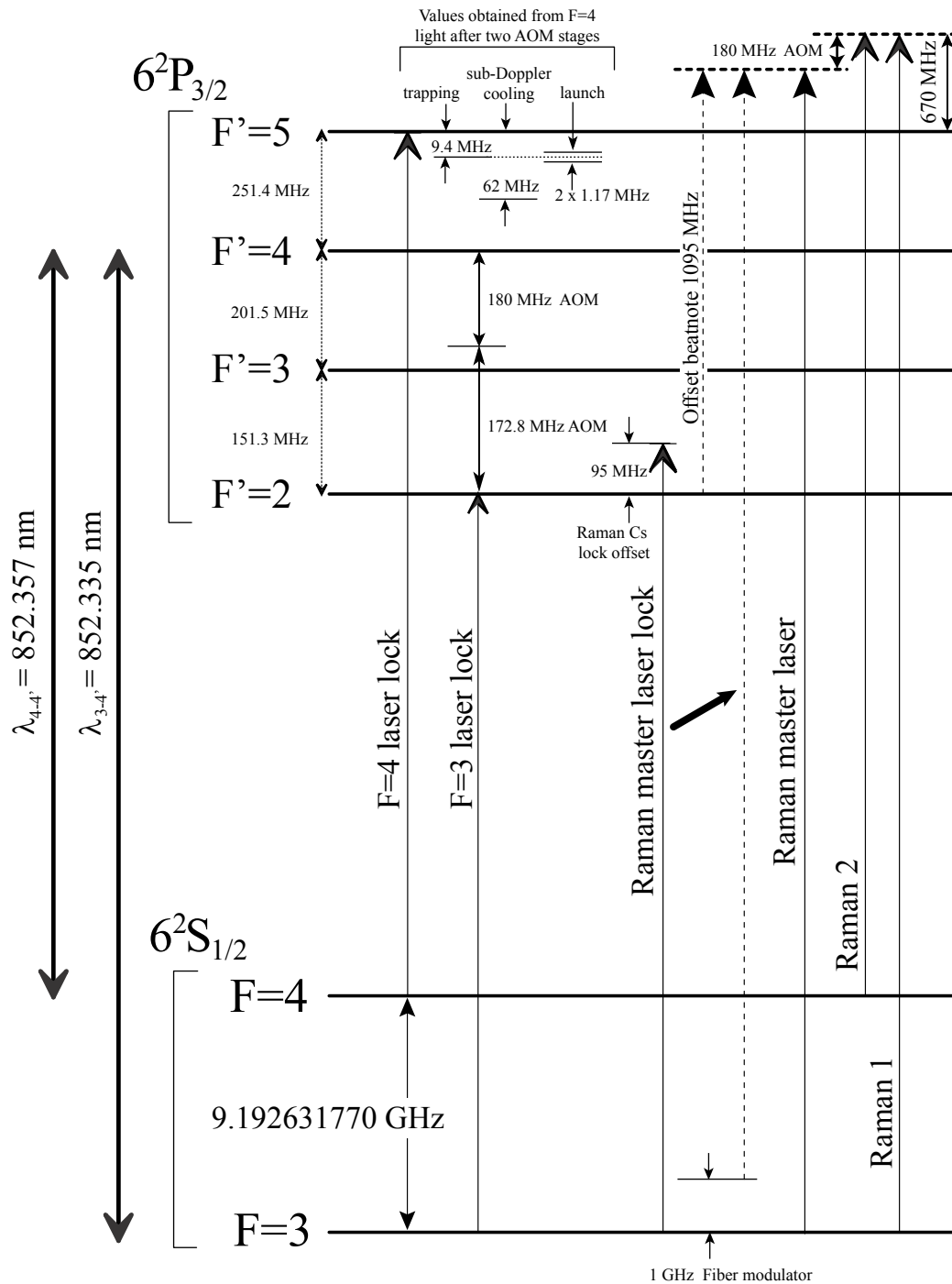


Figure A.1: Cesium energy levels used in this work.

# Appendix B

## Transition Calculation

### B.1 AC Stark Calculation

Laser beam shifts atomic state energy levels, known as the ac Stark effect. Here we consider the case in our interferometer sequence. In particular, two laser beams are  $\sigma^+$  polarization. We start with Rabi frequency coupling states  $|e\rangle$  and  $|g\rangle$ :

$$\Omega = -\frac{\langle e|\mathbf{d}\cdot\mathbf{E}|g\rangle}{\hbar} = \frac{-eE_0}{\hbar}\langle e|r|g\rangle. \quad (\text{B.1})$$

For the strongest transition  $|F = 4, m_F = 4\rangle \rightarrow |F' = 5, m'_F = 5\rangle$ , saturation intensity is [64]:

$$I_s = \frac{\hbar\omega^3\Gamma}{12\pi c^2} = 1.1023(10) \text{ mW/cm}^2. \quad (\text{B.2})$$

Saturation parameter is defined as:

$$s_0 = 2|\Omega|^2/\gamma^2 = I/I_s, \quad (\text{B.3})$$

so

$$|\Omega|^2 = \frac{1}{2} \frac{I}{I_s} \gamma^2, \quad (\text{B.4})$$

where  $\gamma = 2\pi \cdot 5.2227(66)$  MHz. For other transitions:

$$|\Omega_{F,m_F \rightarrow F',m'_F}|^2 = \frac{T_{F,m_F \rightarrow F',m'_F}}{5040} \frac{1}{2} \frac{I}{I_s} \gamma^2, \quad (\text{B.5})$$

where  $T_{F,m_F \rightarrow F',m'_F}$  is the relative transition strength number given in e.g. [64] page 289, and  $I_s$  always refers to the saturation intensity of  $|F = 4, m_F = 4\rangle \rightarrow |F' = 5, m'_F = 5\rangle$  transition.

For stimulated Raman transition, the Rabi frequency between the ground states  $|i\rangle$  and excited state  $|j\rangle$  coupling through light field  $|k\rangle$  is:

$$\Omega_{kji} = \frac{\langle j | \mathbf{d}_{ij} \cdot \mathbf{E} | i \rangle}{\hbar}, \quad (\text{B.6})$$

where in our particular interferometer (see figure B.1):

$$k = 1, 2 \quad (\text{two laser beams}) \quad (\text{B.7})$$

$$i = 3, 4 \quad (\text{two ground states: } F = 3, 4) \quad (\text{B.8})$$

$$j = 2', 3', 4', 5' \quad (\text{four excited states: } F' = 2', 3', 4', 5') \quad (\text{B.9})$$

The effective Rabi frequency between two ground states is:

$$\Omega_{\text{eff}} = \sum_j \frac{\Omega_{1j3}^* \cdot \Omega_{2j4}}{2\Delta_{1j3}}, \quad (\text{B.10})$$

and ac Stark shift of ground state level  $|i\rangle$  is:

$$\Omega_i^{\text{AC}} = \sum_{k,j} \frac{|\Omega_{kji}|^2}{4\Delta_{kji}}. \quad (\text{B.11})$$

To calculate ac Stark shift for  $|F = 4\rangle$  level, we can ignore the effect from laser beam 1 since it is one order of magnitude more away from resonance:

$$\Omega_4^{\text{AC}} = \sum_{k,j} \frac{|\Omega_{kj4}|^2}{4\Delta_{kj4}} = \sum_j \frac{|\Omega_{2j4}|^2}{4\Delta_{2j4}} \quad (\text{B.12})$$

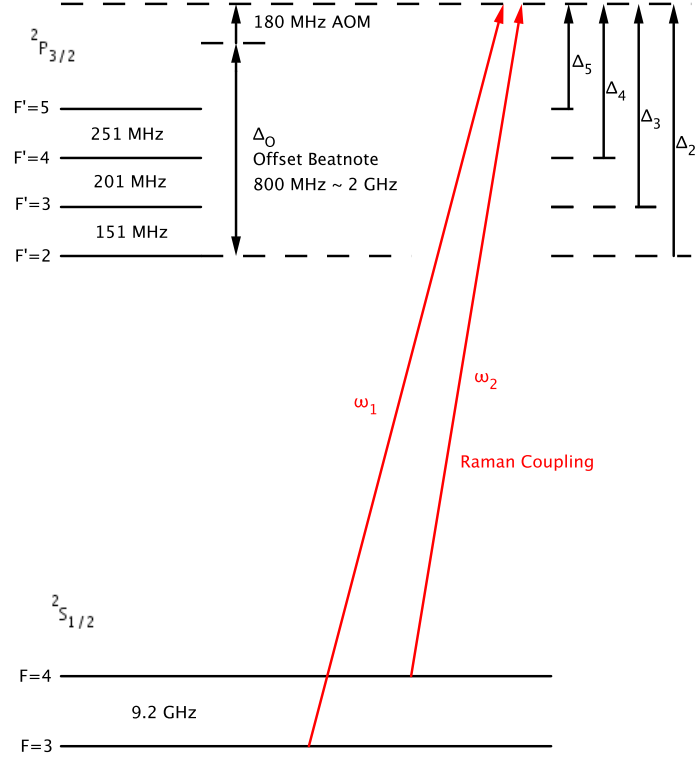


Figure B.1: Energy diagram for Raman transition calculation.

$$= \frac{1}{8} \frac{I_2}{I_s} \gamma^2 \sum_{F'=3'}^{5'} \frac{T_{4,0 \rightarrow F',1}}{5040} \frac{1}{\Delta_{2F'}} \quad (\text{B.13})$$

$$= \frac{1}{8} \frac{I_2}{I_s} \gamma^2 \left( \frac{210}{5040} \frac{1}{\Delta_3} + \frac{1470}{5040} \frac{1}{\Delta_4} + \frac{1680}{5040} \frac{1}{\Delta_5} \right) \quad (\text{B.14})$$

Similarly,

$$\Omega_3^{\text{AC}} = \frac{1}{8} \frac{I_1}{I_s} \gamma^2 \left( \frac{720}{5040} \frac{1}{\Delta_2} + \frac{1890}{5040} \frac{1}{\Delta_3} + \frac{750}{5040} \frac{1}{\Delta_4} \right) \quad (\text{B.15})$$

To cancel the differential ac Stark shift  $\Omega_3^{\text{AC}} = \Omega_4^{\text{AC}}$ , a particular ratio of  $I_2/I_1$  is required, and the ratio depends on the Raman beam single-photon detuning  $\Delta_O$ . Figure 7.3 shows the required ratio  $I_2/I_1$  as a function of detuning.

The effective Rabi frequency is

$$\Omega_{\text{eff}} = \sum_j \frac{\Omega_{1j3}^* \cdot \Omega_{2j4}}{2\Delta_{1j3}} = \sum_{F'=3',4'} \frac{\Omega_{1F'3}^* \cdot \Omega_{2F'4}}{2\Delta_{F'}} \quad (\text{B.16})$$

$$= \frac{\sqrt{|\Omega_{13'3}|^2 |\Omega_{23'4}|^2}}{2\Delta_3} + \frac{\sqrt{|\Omega_{14'3}|^2 |\Omega_{24'4}|^2}}{2\Delta_4} \quad (\text{B.17})$$

$$= \left( \frac{630}{5040} \frac{1}{\Delta_3} + \frac{1050}{5040} \frac{1}{\Delta_4} \right) \frac{1}{4} \frac{\sqrt{I_1 I_2}}{I_s} \gamma^2. \quad (\text{B.18})$$

(One has to check density matrix signs, but two terms do add in B.16.)

The two-photon transition  $\pi$ -pulse time is defined as

$$t_\pi = \pi / \Omega_{\text{eff}}, \quad (\text{B.19})$$

and from this we can calculate ac Stark phase shift atom gets from each beam:

$$\phi_3^{\text{AC}} = \Omega_3^{\text{AC}} \cdot t_\pi \quad (\text{B.20})$$

$$\phi_4^{\text{AC}} = \Omega_4^{\text{AC}} \cdot t_\pi \quad (\text{B.21})$$

If canceling differential ac Stark is required, one can prove that  $\phi_3^{\text{AC}}$  and  $\phi_4^{\text{AC}}$  is a function of  $\Delta_O$ , but do not depend on  $I_1$  or  $I_2$ . Figure 7.3 shows  $\phi_3^{\text{AC}}$  and  $\phi_4^{\text{AC}}$  are both about  $\pi$  rad.

## B.2 Spontaneous Emission

Spontaneous emission rate is

$$\gamma_p = \gamma \frac{s/2}{1 + s + (2\Delta/\gamma)^2}. \quad (\text{B.22})$$

In our setup,  $s \sim 200$ , and  $(2\Delta/\gamma)^2 \sim 10^5 \gg s \gg 1$ , so:

$$\gamma_p \approx \gamma \frac{s/2}{(2\Delta/\gamma)^2} = \frac{\gamma^3 s}{8\Delta^2} = \frac{\gamma}{4\Delta^2} |\Omega|^2. \quad (\text{B.23})$$

Total spontaneous emission rate from  $|F = 3\rangle$  state is:

$$\gamma_{p3} = \sum_{F'=2}^4 \frac{\gamma}{4\Delta^2} |\Omega_{3,0 \rightarrow F',1}|^2 \quad (\text{B.24})$$

$$= \left( \frac{720}{5040} \left( \frac{1}{\Delta_2} \right)^2 + \frac{1890}{5040} \left( \frac{1}{\Delta_3} \right)^2 + \frac{750}{5040} \left( \frac{1}{\Delta_4} \right)^2 \right) \frac{\gamma^3 I_1}{8 I_s}. \quad (\text{B.25})$$

Similarly,

$$\gamma_{p4} = \left( \frac{210}{5040} \left( \frac{1}{\Delta_3} \right)^2 + \frac{1470}{5040} \left( \frac{1}{\Delta_4} \right)^2 + \frac{1680}{5040} \left( \frac{1}{\Delta_5} \right)^2 \right) \frac{\gamma^3 I_2}{8 I_s}. \quad (\text{B.26})$$

The experimentally observable quantity is the depumping rate, or spontaneous decay rate to the other  $F$  ground state. The possible depumping paths from  $|F = 3\rangle$  to  $|F = 4\rangle$  are:

$$|F = 3, m_F = 0\rangle \xrightarrow{\sigma^+} |F' = 3, m_{F'} = 1\rangle \left\{ \begin{array}{l} \xrightarrow{\sigma^+} |F = 4, m_F = 0\rangle : 210/5040 \\ \xrightarrow{\pi} |F = 4, m_F = 1\rangle : 525/5040 \\ \xrightarrow{\sigma^-} |F = 4, m_F = 2\rangle : 525/5040 \end{array} \right.$$

(total fraction of depumping in this path is 1260/5040), and

$$|F = 3, m_F = 0\rangle \xrightarrow{\sigma^+} |F' = 4, m_{F'} = 1\rangle \left\{ \begin{array}{l} \xrightarrow{\sigma^+} |F = 4, m_F = 0\rangle : 1470/5040 \\ \xrightarrow{\pi} |F = 4, m_F = 1\rangle : 147/5040 \\ \xrightarrow{\sigma^-} |F = 4, m_F = 2\rangle : 1323/5040 \end{array} \right.$$

(total 2940/5040). Total depumping rate is:

$$\gamma_{p3(d)} = \left( \frac{1890}{5040} \frac{1260}{5040} \left( \frac{1}{\Delta_3} \right)^2 + \frac{750}{5040} \frac{2940}{5040} \left( \frac{1}{\Delta_4} \right)^2 \right) \frac{\gamma^3 I_1}{8 I_s}. \quad (\text{B.27})$$

Similarly, depumping rate from  $|F = 4\rangle$  to  $|F = 3\rangle$  is

$$\gamma_{p4(d)} = \left( \frac{210}{5040} \frac{3780}{5040} \left( \frac{1}{\Delta_3} \right)^2 + \frac{1470}{5040} \frac{2100}{5040} \left( \frac{1}{\Delta_4} \right)^2 \right) \frac{\gamma^3 I_2}{8 I_s}. \quad (\text{B.28})$$

The fraction of depumping per  $\pi$ -pulse is:

$$d_3 = \gamma_{p3(d)} \cdot t_\pi \tag{B.29}$$

$$d_4 = \gamma_{p4(d)} \cdot t_\pi \tag{B.30}$$

One can experimentally measure  $d_3$  and  $d_4$  by detuning microwave frequency (see section 7.2) without changing other parameters in a Raman pulse.

# Bibliography

- [1] Karoly I. Kis and William B. Agocs. Ars longa vita brevis for the 150th anniversary of Lorand Eotvos' birthday. *The Leading Edge*, 18(6):675–677, 1999.
- [2] R. V. Eötvös. Mathematische und naturwissenschaftliche berichte und ungar. 8:65, 1891.
- [3] A. Peters. *High Precision Gravity Measurements using Atom Interferometry*. PhD thesis, Stanford University, 1998.
- [4] Dwain K. Butler. Microgravimetric and gravity gradient techniques for detection of subsurface cavities. *Geophysics*, 49(7):1084–1096, 1984.
- [5] Valentin Mikhailov, Gwendoline Pajot, Michel Diament, and Antony Price. Tensor deconvolution: A method to locate equivalent sources from full tensor gravity data. *Geophysics*, 72(5):61–69, 2007.
- [6] Ephraim Fischbach, Daniel Sudarsky, Aaron Szafer, Carrick Talmadge, and S. H. Aronson. Reanalysis of the eoumltvös experiment. *Physical Review Letters*, 56(1):3–6, Jan 1986.
- [7] J. B. Lee, D. B. Boggs, M. A. Downey, R. A. M. Maddever, R. J. Turner, and M. H. Dransfield. First test survey results from the falcon helicopter-borne airborne gravity gradiometer system. In *Australian Earth Sciences Convention*, Melbourne, Australia, 2006.

- [8] A. J. Romaides, J. C. Battis, R. W. Sands, A. Zorn, D. O. Benson, and D. J. DiFrancesco. A comparison of gravimetric techniques for measuring subsurface void signals. *Journal of Physics D-Applied Physics*, 34(3):433–443, 2001. 7.
- [9] A. Lawrence. *Modern Inertial Technology: Navigation, Guidance, and Control*. Springer-Verlag, New York, 1998.
- [10] Pratap Misra and Per Enge. *Global Positioning System: Signals, Measurement, and Performance*. Ganga-Jamuna Press, 2006.
- [11] C. Jekeli. Precision free-inertial navigation with gravity compensation by an onboard gradiometer. *Journal of Guidance Control and Dynamics*, 29(3):704–713, 2006. 17.
- [12] Donald C. Barton. Eötvös torsion balance. *Physics*, 3:29–38, 1932.
- [13] George T Gillies. The newtonian gravitational constant: recent measurements and related studies. *Reports on Progress in Physics*, 60(2):151–225, 1997.
- [14] C. C. Speake and T. J. Quinn. The gravitational constant: Theory and experiment 200 years after cavendish. *Measurement Science and Technology*, 10(6), 1999.
- [15] H. W. S. McQueen. Independence of the gravitational constant from gross earth data. *Physics of The Earth and Planetary Interiors*, 26(3):6–9, 1981.
- [16] N. I. Kolosnitsyn. Calibration of gravitational gradiometers using gradient gauges. *Measurement Techniques*, 35(12):1443–1447, 12 1992.
- [17] Hidezumi Terazawa. Simple relation among the electromagnetic fine-structure, fermi weak-coupling, and newtonian gravitational constants. *Physical Review D*, 22(4):1037–1038, Aug 1980.
- [18] T. Damour and A. M. Polyakov. The string dilation and a least coupling principle. *Nuclear Physics B*, 423(2-3):532–558, 1994.

- [19] A. D. Sakharov. Vacuum quantum fluctuations in curved space and the theory of gravitation. *General Relativity and Gravitation*, 32(2):365–367, 02 2000.
- [20] J. M. McGuirk, M. J. Snadden, and M. A. Kasevich. Large area light-pulse atom interferometry. *Physical Review Letters*, 85(21):4498–4501, 2000. 19.
- [21] R. V. Eötvös, D. Pekár, and E. Fekete. *Annalen der Physik (Leipzig)*, 68:11–66, 1922.
- [22] J. H. Gundlach, G. L. Smith, E. G. Adelberger, B. R. Heckel, and H. E. Swanson. Short-range test of the equivalence principle. *Physical Review Letters*, 78(13):2523–2526, Mar 1997.
- [23] Bahram Mashhoon. Gravitational couplings of intrinsic spin. *Classical and Quantum Gravity*, 17(12):2399–2409, 2000.
- [24] Christopher Jekeli. A review of gravity gradiometer survey system data analyses. *Geophysics*, 58(4):508–514, 1993.
- [25] Edwin H. van Leeuwen. BHP develops airborne gravity gradiometer for mineral exploration. *The Leading Edge*, 19(12):1296–1297, 2000.
- [26] M. Ryan. Memphis uses gravity to reach new navigational heights. *Undersea Warfare*, 1:22–3, 1998.
- [27] M. V. Moody and H. J. Paik. Gauss’s law test of gravity at short range. *Physical Review Letters*, 70(9):1195–1198, Mar 1993.
- [28] H. J. Paik, V. Prieto, and M. V. Moody. Probing extra dimensions using a superconducting accelerometer. *Journal of the Korean Physical Society*, 45:S104–S109, 2004. 21 Suppl. S.
- [29] J. M. Brown, T. M. Niebauer, F. J. Klopping, and A. T. Herring. A new fiber optic gradiometer for 4-d absolute differential gravity. *Geophysical Research Letters*, 27(1):33–36, 2000. 14.

- [30] L. de Broglie. *Recherches sur la theorie des quanta (Research on quantum theory)*. PhD thesis, Paris, 1924.
- [31] N. F. Ramsey. A molecular beam resonance method with separated oscillating fields. *Physical Review*, 78(6):695–699, 1950. 9.
- [32] R. Colella, A. W. Overhauser, and S. A. Werner. Observation of gravitationally induced quantum interference. *Physical Review Letters*, 34(23):1472–1474, Jun 1975.
- [33] S. A. Werner, J. L. Staudenmann, and R. Colella. Effect of earth’s rotation on the quantum mechanical phase of the neutron. *Physical Review Letters*, 42(17):1103–1106, Apr 1979.
- [34] T.W. Hansch and A.L. Schawlow. Cooling of gases by laser radiation. *Optics Communications*, 13(1):68–69, 1975.
- [35] D. J. Wineland and Wayne M. Itano. Laser cooling of atoms. *Physical Review A*, 20(4):1521–1540, Oct 1979.
- [36] S. Chu, L. Hollberg, J. E. Bjorkholm, A. Cable, and A. Ashkin. 3-dimensional viscous confinement and cooling of atoms by resonance radiation pressure. *Physical Review Letters*, 55(1):48–51, 1985. 24.
- [37] E. L. Raab, M. Prentiss, A. Cable, S. Chu, and D. E. Pritchard. Trapping of neutral sodium atoms with radiation pressure. *Physical Review Letters*, 59(23):2631–2634, 1987. 7.
- [38] Mark Kasevich and Steven Chu. Atomic interferometry using stimulated raman transitions. *Physical Review Letters*, 67(2):181–184, Jul 1991.
- [39] F. Riehle, Th. Kisters, A. Witte, J. Helmcke, and Ch. J. Bordé. Optical ramsey spectroscopy in a rotating frame: Sagnac effect in a matter-wave interferometer. *Physical Review Letters*, 67(2):177–180, Jul 1991.

- [40] M. A. Kasevich. *Atom Interferometry in an Atomic Fountain*. PhD thesis, Stanford University, 1992.
- [41] M. Kasevich and S. Chu. Measurement of the gravitational acceleration of an atom with a light-pulse atom interferometer. *Applied Physics B: Lasers and Optics*, 54:321–332, 1992.
- [42] A Peters, K Y Chung, and S Chu. High-precision gravity measurements using atom interferometry. *Metrologia*, 38(1):25–61, 2001.
- [43] M. J. Snadden, J. M. McGuirk, P. Bouyer, K. G. Haritos, and M. A. Kasevich. Measurement of the earth’s gravity gradient with an atom interferometer-based gravity gradiometer. *Physical Review Letters*, 81(5):971–974, Aug 1998.
- [44] J. M. McGuirk, G. T. Foster, J. B. Fixler, M. J. Snadden, and M. A. Kasevich. Sensitive absolute-gravity gradiometry using atom interferometry. *Physical Review A*, 65(3):033608, Feb 2002.
- [45] T. L. Gustavson, P. Bouyer, and M. A. Kasevich. Precision rotation measurements with an atom interferometer gyroscope. *Physical Review Letters*, 78(11):2046–2049, Mar 1997.
- [46] T L Gustavson, A Landragin, and M A Kasevich. Rotation sensing with a dual atom-interferometer sagnac gyroscope. *Classical and Quantum Gravity*, 17(12):2385–2398, 2000.
- [47] D. S. Durfee, Y. K. Shaham, and M. A. Kasevich. Long-term stability of an area-reversible atom-interferometer sagnac gyroscope. *Physical Review Letters*, 97(24):240801, 2006.
- [48] K. Takase. *Precision Rotation Rate Measurements with a Mobile Atom Interferometer*. PhD thesis, Stanford University, 2008.
- [49] David S. Weiss, Brenton C. Young, and Steven Chu. Precision measurement of the photon recoil of an atom using atomic interferometry. *Physical Review Letters*, 70(18):2706–2709, May 1993.

- [50] B. Young, M. Kasevich, and S. Chu. *Atom Interferometry*, chapter Precision Atom Interferometry with Light pulses, pages 363–406. Academic Press Inc, 1997.
- [51] H. Muller, S. W. Chiow, Q. Long, C. Vo, and S. Chu. A new photon recoil experiment: towards a determination of the fine structure constant. *Applied Physics B-Lasers and Optics*, 84(4):633–642, 2006.
- [52] J. B. Fixler. *Atom Interferometer-Based Gravity Gradiometer Measurements*. PhD thesis, Yale University, 2003.
- [53] J. B. Fixler, G. T. Foster, J. M. McGuirk, and M. A. Kasevich. Atom interferometer measurement of the newtonian constant of gravity. *Science*, 315(5808):74–77, 2007.
- [54] A. Bertoldi, G. Lamporesi, L. Cacciapuoti, M. de Angelis, M. Fattori, T. Petelski, A. Peters, M. Prevedelli, J. Stuhler, and G. M. Tino. Atom interferometry gravity-gradiometer for the determination of the newtonian gravitational constant  $g$ . *European Physical Journal D*, 40(2):271–279, 2006.
- [55] Charles H-T Wang, Robert Bingham, and J Tito Mendonca. Quantum gravitational decoherence of matter waves. *Classical and Quantum Gravity*, 23(18):L59–L65, 2006.
- [56] Craig J. Hogan. Indeterminacy of holographic quantum geometry. *Physical Review D*, 78(8):087501, 2008.
- [57] Savas Dimopoulos and Andrew A. Geraci. Probing submicron forces by interferometry of bose-einstein condensed atoms. *Physical Review D*, 68(12):124021, Dec 2003.
- [58] Savas Dimopoulos, Peter W. Graham, Jason M. Hogan, and Mark A. Kasevich. Testing general relativity with atom interferometry. *Physical Review Letters*, 98(11):111102, 2007.

- [59] Jürgen Audretsch and Karl-Peter Marzlin. Ramsey fringes in atomic interferometry: Measurability of the influence of space-time curvature. *Physical Review A*, 50(3):2080–2095, Sep 1994.
- [60] R. Y. Chiao and A. D. Speliotopoulos. Towards migo, the matter-wave interferometric gravitational-wave observatory, and the intersection of quantum mechanics with general relativity. *Journal of Modern Optics*, 51(6-7):861–899, 2004.
- [61] Stefano Foffa, Alice Gasparini, Michele Papucci, and Riccardo Sturani. Sensitivity of a small matter-wave interferometer to gravitational waves. *Physical Review D*, 73(2):022001, 2006.
- [62] P. Delva, M-C. Angonin, and Ph. Tournenc. Matter waves and the detection of gravitational waves. *Journal of Physics: Conference Series*, 66:012050 (7pp), 2007.
- [63] Sung Hoon Yang, Kwang Jae Baek, Taeg Yong Kwon, Young Bum Kim, and Ho Seong Lee. Second-order zeeman frequency shift in the optically pumped cesium beam frequency standard with a dual servo system. *Japanese Journal of Applied Physics*, 38(Part 1, No. 10):6174–6177, 1999.
- [64] H. J. Metcalf and P. van der Straten. *Laser Cooling and Trapping*. Springer-Verlag, New York, 1999.
- [65] G. Avila, V. Giordano, V. Candelier, E. de Clercq, G. Theobald, and P. Cerez. State selection in a cesium beam by laser-diode optical pumping. *Physical Review A*, 36(8):3719–3728, Oct 1987.
- [66] J. M. McGuirk, G. T. Foster, J. B. Fixler, and M. A. Kasevich. Low-noise detection of ultracold atoms. *Optics Letters*, 26(6):364–366, 2001.
- [67] G. W. Biedermann, X. Wu, L. Deslauriers, K. Takase, and M. A. Kasevich. Low-noise simultaneous fluorescence detection of two atomic states. *Opt. Lett.*, 34(3):347–349, 2009.

- [68] S Bize, P Laurent, M Abgrall, H Marion, I Maksimovic, L Cacciapuoti, J Grunert, C Vian, F Pereira dos Santos, P Rosenbusch, P Lemonde, G Santarelli, P Wolf, A Clairon, A Luiten, M Tobar, and C Salomon. Cold atom clocks and applications. *Journal of Physics B: Atomic, Molecular and Optical Physics*, 38(9):S449–S468, 2005.
- [69] B. C. Young, F. C. Cruz, W. M. Itano, and J. C. Bergquist. Visible lasers with subhertz linewidths. *Physics Review Letters*, 82(19):3799–3802, May 1999.
- [70] K. Bongs, R. Launay, and M. A. Kasevich. High-order inertial phase shifts for time-domain atom interferometers. *Applied Physics B-Lasers and Optics*, 84(4):599–602, 2006. Bongs, K. Launay, R. Kasevich, M. A. 26.
- [71] Kurt Gibble. Difference between a photon’s momentum and an atom’s recoil. *Physical Review Letters*, 97(7):073002, 2006.
- [72] Christian J. Borde Peter Wolf. Recoil effects in microwave ramsey spectroscopy. <http://arxiv.org/abs/quant-ph/0403194>, 2004.
- [73] K. Dieckmann. *Bose-Einstein Condensation with High Atom Number in a Deep Magnetic Trap*. PhD thesis, de Universiteit van Amsterdam, 2001.
- [74] G. W. Biedermann. *Gravity Tests, Differential Accelerometry and Interleaved Clocks with Cold Atom Interferometers*. PhD thesis, Stanford University, 2007.
- [75] O. Schmidt, K. M. Knaak, R. Wynands, and D. Meschede. Cesium saturation spectroscopy revisited - how to reverse peaks and observe narrow resonances. *Applied Physics B-Lasers and Optics*, 59(2):167–178, 1994.
- [76] Leo W. Hollberg Richard W. Fox, Chris W. Oates. *Cavity-Enhanced Spectroscopies: Experimental Methods in the Physical Sciences*, chapter Stabilizing diode lasers to high-finesse cavities, pages 1–46. Academic Press, 2002.
- [77] M. J. Lawrence, B. Willke, M. E. Husman, E. K. Gustafson, and R. L. Byer. Dynamic response of a fabry–perot interferometer. *Journal of the Optical Society of America B-Optical Physics*, 16(4):523–532, 1999.

- [78] Chetan Mahadeswaraswamy. *Atom Interferometric Gravity Gradiometer: Transfer Function Estimation and Mobile Gradiometry*. PhD thesis, Stanford University, 2009.
- [79] Andrew Fitzgibbon, Maurizio Pilu, and Robert B. Fisher. Direct least square fitting of ellipses. *IEEE Transactions on Pattern Analysis and Machine Intelligence*, 21(5):476–480, 1999.
- [80] G. T. Foster, J. B. Fixler, J. M. McGuirk, and M. A. Kasevich. Method of phase extraction between coupled atom interferometers using ellipse-specific fitting. *Optics Letters*, 27(11):951–953, 2002.
- [81] John K. Stockton, Xinan Wu, and Mark A. Kasevich. Bayesian estimation of differential interferometer phase. *Physical Review A*, 76(3):033613, 2007.
- [82] Mark A. Kasevich Jason M. Hogan, David M. S. Johnson. Light-pulse atom interferometry. <http://arxiv.org/abs/0806.3261>, 2008.
- [83] W. M. Itano, J. C. Bergquist, J. J. Bollinger, J. M. Gilligan, D. J. Heinzen, F. L. Moore, M. G. Raizen, and D. J. Wineland. Quantum projection noise: Population fluctuations in two-level systems. *Physical Review A*, 47(5):3554–3570, May 1993.
- [84] Mark Kasevich. Private communications, 2008.
- [85] A. Schoof, J. Grünert, S. Ritter, and A. Hemmerich. Reducing the linewidth of a diode laser below 30 hz by stabilization to a reference cavity with a finesse above 105. *Opt. Lett.*, 26(20):1562–1564, 2001.
- [86] Ken Takase, John K. Stockton, and Mark A. Kasevich. High-power pulsed-current-mode operation of an overdriven tapered amplifier. *Optics Letters*, 32(17):2617–2619, 2007.
- [87] P. J. Mohr and B. N. Taylor. Codata recommended values of the fundamental physical constants: 2002. *Reviews of Modern Physics*, 77(1):1–107, 2005.

- [88] Boca Raton, editor. *CRC Handbook of Chemistry and Physics*. CRC Press, 2000.
- [89] Michael P. Bradley, James V. Porto, Simon Rainville, James K. Thompson, and David E. Pritchard. Penning trap measurements of the masses of  $c133s$ ,  $r87$ ,  $85b$ , and  $n23a$  with uncertainties  $\leq 0.2$  ppb. *Physical Review Letters*, 83(22):4510–4513, Nov 1999.
- [90] V. Gerginov, C. E. Tanner, S. Diddams, A. Bartels, and L. Hollberg. Optical frequency measurements of  $6s\ ^2s_{1/2} - 6p\ ^2p_{3/2}$  transition in a  $^{133}\text{Cs}$  atomic beam using a femtosecond laser frequency comb. *Physical Review A*, 70(4):042505, Oct 2004.
- [91] R. J. Rafac, C. E. Tanner, A. E. Livingston, K. W. Kukla, H. G. Berry, and C. A. Kurtz. Precision lifetime measurements of the  $6^2p_{1/2,3/2}$  states in atomic cesium. *Physical Review A*, 50(3):1976–1979, Sep 1994.
- [92] L. Young, W. T. Hill, S. J. Sibener, Stephen D. Price, C. E. Tanner, C. E. Wieman, and Stephen R. Leone. Precision lifetime measurements of  $\text{Cs } 6p\ ^2p_{1/2}$  and  $6p\ ^2p_{3/2}$  levels by single-photon counting. *Physical Review A*, 50(3):2174–2181, Sep 1994.
- [93] Robert J. Rafac and Carol E. Tanner. Measurement of the ratio of the cesium  $d$ -line transition strengths. *Physical Review A*, 58(2):1087–1097, Aug 1998.